NASA SCATTEROMETER BEAM BALANCE USING HOMOGENOUS LAND TARGETS

by

Josko Zec
B.S. University of Zagreb, 1992
M.S. New Jersey Institute of Technology, 1994

A dissertation submitted in partial fulfillment of the requirements
for the degree of Doctor of Philosophy
in the Department of Electrical and Computer Engineering
in the College of Engineering
at the University of Central Florida
Orlando, Florida

Summer Term
1998

Major Professor: Linwood W. Jones

ABSTRACT

Satellite scatterometers are spaceborne radars designed to measure normalized radar cross section (σ^o) of the target illuminated by sensor antennas. σ^o measurements are used to retrieve various geophysical parameters, primarily wind speed and direction over sea surface. To remove direction ambiguity, which is inherent in the relation between wind vector and σ^o, multi-azimuth observations are necessary. Antennas providing multiple looks must be well calibrated to eliminate beam biases. A simple method is proposed for post-launch scatterometer beam-bias removal. It relies on homogenous land targets with azimuth-isotropic radar response. The method is applied to calculate beam balance corrections for the NASA Scatterometer (NSCAT) using Amazon rainforest as a calibration target. NSCAT flew on board Japan's Advanced Earth Observing Satellite (ADEOS) between Aug. 96 and June 97. Calculated corrections agree well with results from other methods (ice and open ocean measurements). Difference is noticed in corrections calculated separately from ascending and descending passes over Amazon. It is shown that imperfect ADEOS attitude can cause this inconsistency. The beam balance is used to estimate the attitude bias. Mean yaw angle bias of 0.25^o between ascending and descending passes is suggested as the main cause of different ascending/descending corrections. Applying this attitude adjustment decreases standard deviation of σ^o measurements and makes ascending and descending corrections consistent.

ACKNOWLEDGEMENTS

I would like to thank my advisor Dr. Linwood Jones for his excellent leadership during the research that resulted in this dissertation.

I am grateful to Dr. David Long at Brigham Young University. His high-resolution land masks were critical for the applied method.

Dr. Scott Dunbar at NASA Jet Propulsion Laboratory provided data and enormous help and guidance in NASA Scatterometer data processing.

Other gentleman, whose suggestions helped clarify the right direction of the research, include: Wu-Yang Tsai, James Huddleston, Mike Spencer, and Richard West, all from Jet Propulsion Laboratory.

This research was sponsored by the contract with National Aeronautics and Space Administration and Jet Propulsion Laboratory.

TABLE OF CONTENTS

LIST OF TABLES

LIST OF FIGURES

1 INTRODUCTION

Satellite scatterometers are spaceborne radars designed to measure the normalized radar cross-section (σ^o) of the target area illuminated by the sensor antennas. A directly measured value is the power reflected from the target. The normalized radar cross section σ^o is calculated from the reflected power and is a signature of the target. Several geophysical parameters can be retrieved from σ^o of natural targets, such as ice-edge, vegetation type, soil moisture, snow depth, and wind vectors over sea surfaces. Wind retrieval is the primary application of most scatterometers. The scatterometer wind retrieval technique is based on the relation between σ^o and wind vectors. Surface wind determines sea-surface roughness, which, together with dielectric properties, determines σ^o. Since scatterometer measures σ^o, it can retrieve wind vectors using this relation. Global wind vectors are main input into numerical models for weather prediction. Accuracy of a prediction model critically depends on the availability of frequently sampled wind vectors, with uniform and global coverage. Only a spaceborne instrument can provide such coverage, and satellite scatterometers are therefore expected to become the main source of wind observations in the future. Several instruments can estimate wind speed alone (radiometers, altimeters), but only scatterometers retrieve direction as well. Direction retrieval is possible if the same point is observed from multiple azimuths. Scatterometers are therefore multi-antenna instruments. These antennas must be well calibrated to eliminate biases among individual beams. For the required wind vector accuracy, beams must be balanced to within few tenths of a dB. Pre-launch calibration alone is not sufficient for such accuracy, so post-launch activities are planned for scatterometer missions. Earth stations and distributed land targets have been used in the past for beam balancing before σ^o data sets are released to the scientific community.

NASA Scatterometer (NSCAT) has been the latest satellite scatterometer. It flew onboard Japan's Advanced Earth Observing Satellite (ADEOS) between August 17, 1996 and June 30, 1997, when malfunction of power generating solar panels caused an early end of the mission. This dissertation proposes a simple and fast converging method that has been applied toward NSCAT beam balancing. The method relies on homogenous large area targets with azimuth-isotropic radar response, such as Amazon rainforest. It uses polynomial modeling of σ^o response and forces individual beams to the referent value, the average of all beams. The method is therefore relative and converges faster than other proposed methods (ice and open ocean measurements). The unique approach is adopted, where large target is divided into non-overlapping smaller location elements. These elements become micro-cells for beam balancing. Results agree well with other methods and with the balancing numbers accepted in the NSCAT final σ^o reprocessing before data release.

During inter-beam calibration, a stable difference is noted between the beam corrections calculated separately from ascending (night) and descending (day) passes over the target. Since geophysical parameters can not account for the diurnal effect of beam biases, an attempt is made to attribute this discrepancy to imperfect reporting of ADEOS attitude (roll, pitch, and yaw angles). A minimum objective function mathematical model is derived to estimate the mean attitude that will produce the most consistent ascending/descending beam balance. The iterative procedure suggests 0.25^o ascending vs. descending difference in yaw angle as the most effective attitude adjustment at Equatorial latitudes. Applying the proposed attitude adjustment decreases standard deviation of σ^o measurements and difference in ascending versus descending-based corrections.

This dissertation is organized into 6 chapters. After short introduction, scattering of electromagnetic waves is summarized in Chapter 2. The chapter defines σ^o, discusses radar operation in remote sensing and surface and volume scattering mechanisms. Chapter 3 covers principles of scatterometry, motivation behind it, and operational aspects. Scatterometer wind retrieval process is explained and a brief history of satellite scatterometry is given. NSCAT is described in more detail and a section is devoted to data processing segment of the mission. Future missions are also listed. Chapter 4 is the core of the dissertation. The method employed for NSCAT beam balancing is described. Scatterometer calibration in general is explained, followed by a mathematical description of the method. Data selection using high-resolution maps is explained. Mask division is introduced as a way to ease homogeneity requirement on the target. Results are presented with corrections calculated in different periods of the NSCAT mission. A comparison with the accepted beam balance confirms the validity of the method. Chapter 5 discusses attitude estimation using beam balance results. Discrepancy between ascending and descending - based beam balance is illustrated, followed by a mathematical description of the technique for attitude estimation. The objective function is formulated and calculated as a function of different attitude sets (roll, pitch, and yaw angles). The argument of the minimum objective function is the suggested mean ADEOS attitude over the latitude range of the Amazon basin. The improved consistency is shown when proposed attitude adjustment is made. The dissertation concludes with a brief summary and conclusions in Chapter 6.

Numerical results and calibration data processing are covered in appendixes. Appendix A contains a table with the beam balance correction results. The record structure of the NSCAT Level 1.5 data is tabulated in Appendix B. Based on the record structure from Appendix B, Appendix C lists FORTRAN program used to coarsely select records from Level 1.5 that were measured in the vicinity of the target. Appendix D lists MATLAB routines to finely select data points taken from within a high-resolution mask and to calculate beam-balance corrections. It also contains MATLAB programs for beam balancing at multiple attitudes, in order to identify the attitude with the most consistent ascending/descending correction results.

2 ELECTROMAGNETIC SCATTER

2.1 Introduction

Exact modeling of the interaction between electromagnetic (EM) waves and matter is a complex task owing to the scale and the number of parameters governing this interaction. This is especially true for the case of scattering from large natural surfaces. For example, ocean wave spectrum is shaped by parameters such as long-wave slope, atmospheric stability, sea-surface temperature, air pressure, salinity, wind speed and direction, the polarization of radiation, incidence angle and others. Accounting all of the above would lead to a complicated deterministic model and therefore statistical and empirical approach is adopted to estimate and predict average results of interaction of EM energy and such targets. An EM wave radiated by an instrument propagates freely according to Maxwell equations [5]. For instruments mounted on Earth-orbiting platforms, radiation first interacts with Earth's atmosphere. Composition of the atmosphere is varying and is driven by many parameters (temperature, solar radiation, emissions from the earth, etc). Therefore, statistical models (standard atmosphere [15, 18, 42]) are used to describe atmospheric effects on propagation. In this dissertation, the assumption is made that the atmosphere is modeled well and that the effects of propagation through the atmosphere are accounted for. The important interaction, for this study, is between EM radiation and Earth's surface. The amount of energy reflected from the surface is a signature of the illuminated area. This enables remote sensing of various surface properties. Of particular interest is the ability to estimate near-surface winds over sea. Wind estimation techniques will be described in chapter 3. The remainder of this chapter will discuss physical basis of EM scatter. Radar cross-section will be introduced through radar equation. Extended-area targets are treated in section 2.3. Models for surface scattering are reviewed in section 2.4 and for volume scattering in section 2.5.

2.2 Radar Cross Section

Radars [38,39] are active microwave instruments used to detect, track, image or remotely sense properties of the observed target. They operate on microwave frequencies (3-300 GHz) enabling all-weather and light-independent operation. Standard designations of radar frequency bands are tabulated in Table 1. Radars transmit either continuous waves (CW radars) or pulses of microwave energy (pulsed radars). Objects found in the path of transmitted radiation will partially absorb and partially scatter incident energy.

Frequency band	Range [GHz]
L	1-2
S	2-4
C	4-8
X	8-12
Ku	12-18
K	18-27
Ka	27-40
Millimeter	40-300

Table 1: Satellite radar frequency designations

Scattered radiation is caused by the currents induced on the object, by the incident EM field. Scatter is in all direction and is driven by laws of physical optics and geometrical theory of diffraction [5,25]. Power returned in the direction of the source (backscattered power, P_r) is of particular interest. Transmitted and backscattered power are related by radar equation:

$$P_r = \frac{P_t G_t}{4\pi R^2} \sigma \frac{1}{4\pi R^2} A_r \ , \tag{2.1}$$

where P_t is transmitted power [W], G_t is gain of the transmitting antenna, R is distance between the radar and the target [m], A_r is effective aperture of the receiving antenna [m^2], and σ is the radar cross-section [m^2]. Equation (2.1) illustrates a propagation circle from transmitting power P_t, which is directionally modulated by the antenna pattern (gain G_t) and attenuated due to the free-space loss ($1/4\pi R^2$). Upon incidence on an object, power is reflected, determined by the object's reflective properties. They are expressed by the proportionality constant σ. Reflected power is attenuated by additional free space loss $1/4\pi R^2$ while propagating back to radar. Finally, a part of reflected power is captured by the receiving antenna with effective aperture A_r. Using relation between effective antenna aperture A_r and receiving antenna gain G_r:

$$A_r = \frac{\lambda^2}{4\pi} G_r \ , \tag{2.2}$$

equation (2.1) can be written in a compact form:

$$P_r = \frac{P_t G_t G_r \lambda^2}{(4\pi)^3 R^4} \sigma \ . \tag{2.3}$$

Equation (2.3) is the fundamental radar equation for point targets. It is simplified by neglecting losses that can not be avoided in real operation. It illustrates the role of the radar cross section σ as a target's signature. Since σ is affected by a broad range of geophysical parameters, remote sensing of these parameters is possible by calculating σ from measured $P_{r,}$ inverting (2.3):

$$\sigma = \frac{(4\pi)^3 R^4 P_r}{P_t G_r G_t \lambda^2} \ . \tag{2.4}$$

For a small number of simple objects, σ can be analytically calculated. This has been done for ideal geometrical shapes and such objects are used for radar calibration [4, 27]. Realistic radar targets can be only loosely approximated by ideal shapes. The results of calculations are only used to give initial idea of σ. Measurements are required to associate reliable σ to a given radar target and confirm preliminary calculations. A classical example of the ideal object for which σ can be analytically derived is a metallic sphere with radius a [4]. Three scattering regimes are illustrated on Figure 1. Radar cross-section is normalized to projected area πa^2 and plotted as a function of circumference normalized to wavelength $ka = 2\pi a / \lambda$. Distinctive regions noted on Figure 1 are:

- Rayleigh region ($\lambda >> L$, L is body size): Because the wavelength is much greater than the target, there is no phase variation over the spatial extent of the target. The scattering mechanism is based on dipole moments induced on the reflecting body. Details of the target shape are not important since entire body participates in the scattering as a point.
- Resonant region ($\lambda \approx L$): Oscillatory behavior is due to interference of specular (true optics) reflections and the creeping wave around the sphere. This region is bounded by $1 \leq L/\lambda \leq 10$. Overall geometry is important and exact solution of Maxwell equations is required. Method of moments [5] is employed to solve Stratton-Chu integral forms [4], which describe scattering in the resonant region.

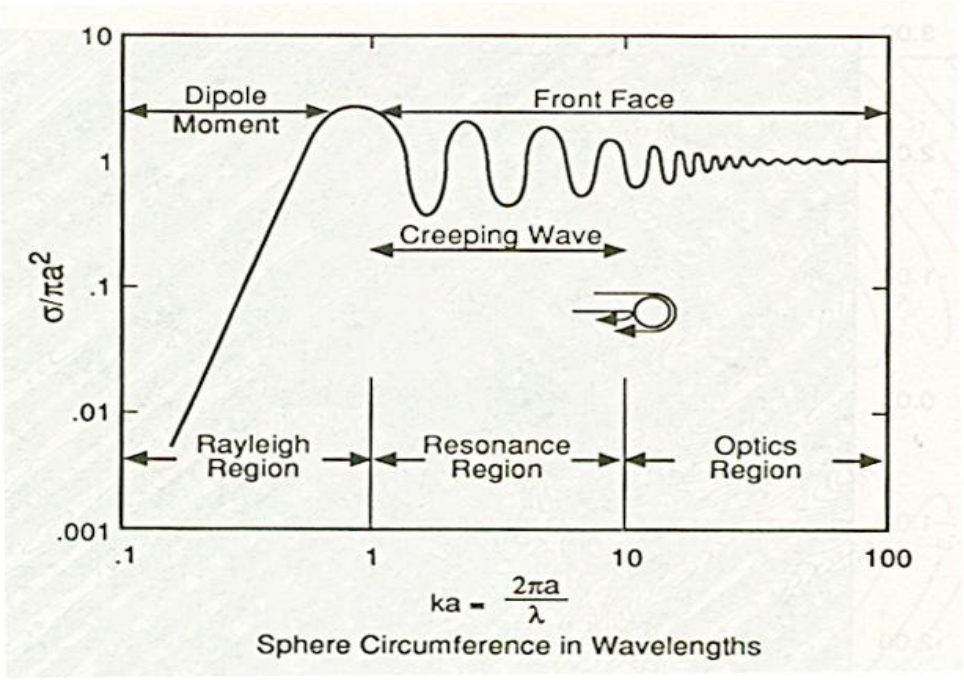

Figure 1: Radar cross section of a metallic sphere

- Optics region ($\lambda << L$): In this region, surface and creeping waves disappear and front-face reflection is the main mechanism. Radar cross-section is $\sigma = \pi a^2$, which is the projected area of the sphere.

For other, more complex targets, detailed geometry becomes important, as total scattering is collected from independent scattering centers. σ becomes a complicated phasor sum, and empirical and statistical models are used.

2.3. Radar cross section of distributed targets

Equation (2.3) is appropriate for point targets whose dimensions are negligible to antenna field of view. In most remote sensing applications, radar observes large areas on Earth or on extraterrestrial objects. For such observations, σ can not be taken as a constant. Rather, radar return is composed by coherent contributions from a large number of point scatterers within the illuminated area [28]. The scattering cross-section of the individual sub-target is:

$$\sigma = \frac{\sigma_i \Delta A_i}{\Delta A_i} \quad . \tag{2.5}$$

If each sub-target contains enough point scatterers, the average value of σ_i can be calculated as:

$$\sigma^o = \left\langle \frac{\sigma_i}{\Delta A_i} \right\rangle \quad , \tag{2.6}$$

where σ^o is dimensionless [m^2/m^2] normalized radar cross-section. Now $\sigma_i=\sigma^o \Delta A_i$ and radar equation (2.3) can be written for extended area targets over area A:

$$P_r = \frac{\lambda^2}{(4\pi)^3} \int_A \frac{P_t G_t G_r}{R} \sigma^o dA \ . \tag{2.7}$$

Logarithmic decibel units (dB) are used in practice for σ^o:

$$\sigma^o[dB] = 10\log_{10}(\sigma^o) \ . \tag{2.8}$$

Factors determining σ^o of a target can be broadly classified into geometric, dielectric, and instrument related properties. Geometric properties include roughness, size, and slope of the object while dielectric properties include complex permitivity (dielectric constant), complex permeability, and homogeneity of material. Instrument related factors are wavelength, polarization, incidence and azimuth angle, and resolution. Dielectric properties of the material are described by the complex permitivity:

$$\varepsilon = \varepsilon^{'} - \varepsilon^{''} = \varepsilon_0 (\varepsilon_r - j\frac{\gamma}{\omega\varepsilon_0}) \ , \tag{2.9}$$

where $\varepsilon_0=8.854 \cdot 10^{-12}$ Farad/meter is permitivity of the free space, ε_r is relative permitivity of the material, $\omega=2\pi f$ [rad] is radial frequency, and γ is the conductivity of the medium in siemens or mhos. Several important values for ε_r are given in Table 2. Generally, smaller values of $\varepsilon''/\varepsilon'$ (lower conductivity) will cause deeper EM penetration through the surface. From Table 2 it can be observed that presence of water causes large permitivity increase compared to dry material. This is a mechanism by which soil moisture can be sensed [36].

Material	dry soil	sand	Snow	water	Mahogany
ε'	2.44	2.55	1.2	77	1.9
ε''	0.006	0.001	0.0003	0.157	0.025

Table 2: Permitivity of selected materials at 3 GHz

Remote sensing radars on moving platforms experience Doppler frequency shift. It varies for different points within a large natural target due to different radar radial velocity among points comprising the target. This enables discrimination and spatial resolution on the ground. Frequency of the returned signal is:

$$f_r = f_t + f_d = f_t - \frac{2v_r}{\lambda} \ , \tag{2.10}$$

where f_t is transmitted frequency, f_r is received frequency, f_d is Doppler shift and v_r is radial velocity. Minus sign in (2.10) expresses the fact that received frequency is lower than transmitted when radar is receding (distance between radar and target (R) is increasing and $v_r = \frac{dR}{dt}$). Binning the received signal into frequency bins is therefore equivalent to spatial discrimination, since returns from different points will have different

v_r. It can be shown [42] that for radar horizontal motion above the plane surface, loci of the points with constant Doppler shift are hyperbolas. The equation of these hyperbolas (isodops) is:

$$h^2 = x^2\left[\left(\frac{f_{d0}}{f_d}\right)^2 - 1\right] - y^2 \quad , \tag{2.11}$$

where h is the radar altitude, y is the ground projection of the flight direction, x is perpendicular to y, and f_{do} is the Doppler shift for the points along the direction of motion ($f_{do} \geq f_d$). All points within a distributed target whose planar coordinates (x,y) satisfy (2.11), return signal at the same frequency. Relation is more complicated for included effects of Earth rotation. Earth rotation has to be included in vectorial relative velocity calculation. It results in rotation of the hyperbolic contours by approximately 3.5^{o} at the Equator. The effect is illustrated by an example on Figure 2. Satellite is assumed in circular orbit at h=800 km. From the first Keppler law, this determines spacecraft ground velocity v_g as:

$$v_g = \sqrt{\frac{\mu}{(h+\rho)}}\frac{\rho}{\rho+h} \quad , \tag{2.12}$$

where ρ=6378.14 km is the mean Earth radius and μ=3.986 X $10^5\,\text{km}^5 / \text{s}^3$ is Keppler constant. Contours of different Doppler shifts are shown at Equator zero latitude for four

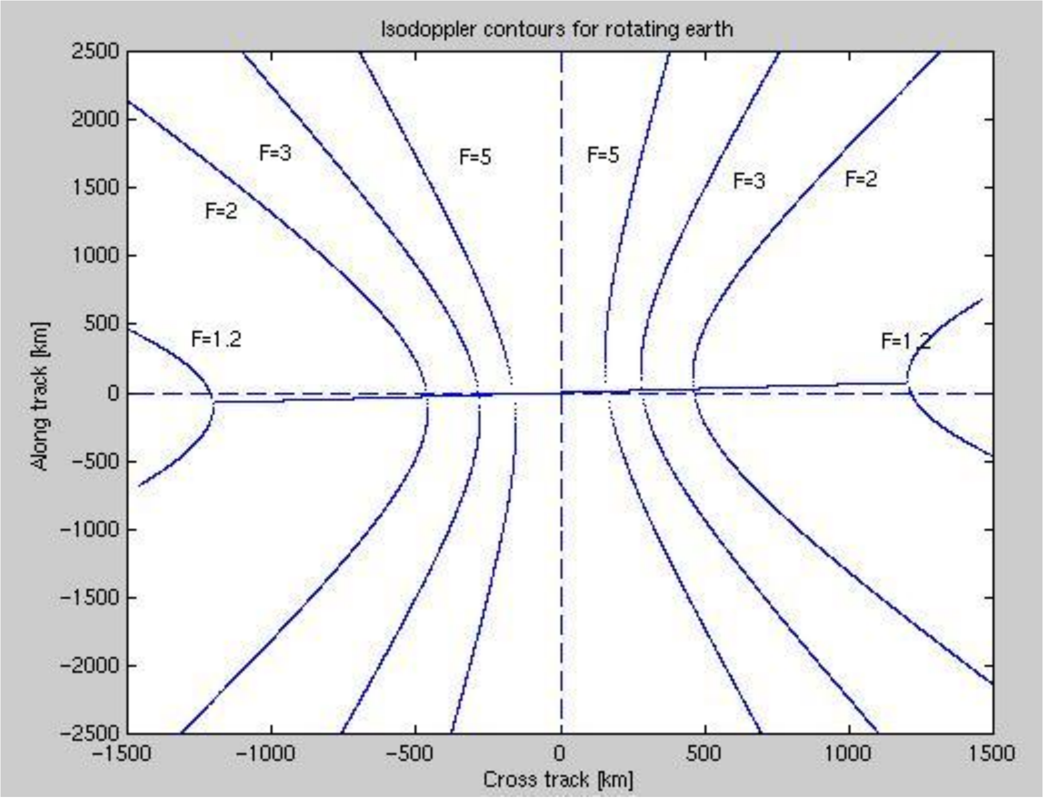

Figure 2: Isodoppler contours for rotating earth

values of parameter $F=f_{do}/f_d$ (1.2, 2, 3, and 5).

2.4 Surface scattering models

When EM wave impinges upon the boundary surface between two semi-infinite media, a portion of the incident energy is scattered and the rest propagates across the boundary through the lower medium. If the lower medium is homogenous, scattering will be limited to the boundary area. Depending on the surface roughness, three scattering mechanisms can be identified (Figure 3). Reflection from the smooth surface is primarily specular reflection determined by Fresnel laws [5]. Except for near-nadir incidence, a

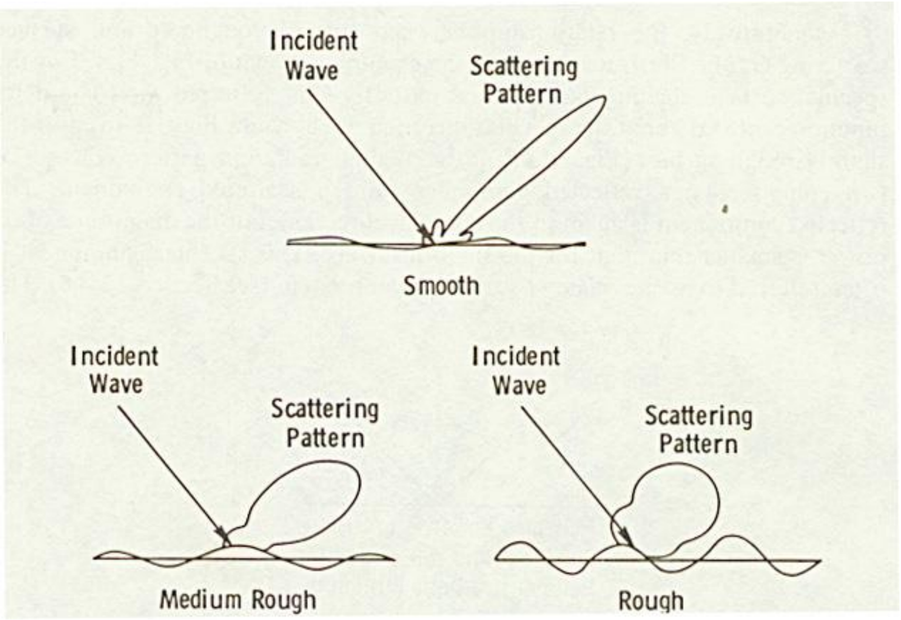

Figure 3: Surface scattering patterns

smooth surface would return little power to the monostatic radar. Medium-rough surface reflects both coherent (in specular direction) and non-coherent (all directions) radiation. Rough or Lambertian surface causes primarily non-coherent scatter. Roughness of a surface is relative property, determined by the frequency used. Surface characterized as rough for optical frequencies may be classified as smooth for microwaves.

Random surface roughness of natural targets is described by two statistical parameters, standard deviation of surface height and surface correlation length [6]. Standard deviation of the surface height over a L_x X L_y segment is defined using mean height $\bar{h}$:

$$\bar{h} = \frac{1}{L_x L_y} \int_{-Lx/2}^{Lx/2} \int_{-Ly/2}^{Ly/2} h(x,y)\,dx\,dy \quad , \tag{2.13}$$

and the second moment $\bar{h}_2$:

$$\bar{h}_2 = \frac{1}{L_x L_y} \int_{-Lx/2}^{Lx/2} \int_{-Ly/2}^{Ly/2} h^2(x,y)dxdy \quad . \tag{2.14}$$

The standard deviation of the surface height is:

$$\rho_h = (\bar{h})^2 - \bar{h}_2 \quad . \tag{2.15}$$

The normalized autocorrelation function is defined in one dimension as:

$$\rho_l(l) = \frac{\int_{-Lx/2}^{Lx/2} h(x)h(x+l)dx}{\int_{-Lx/2}^{Lx/2} h^2(x)dx} \quad . \tag{2.16}$$

The surface correlation length L is defined as displacement for which the normalized autocorrelation function is 1/e (e = 2.718, the base of the natural logarithm):

$$\rho_l(L) = \frac{1}{e} \quad . \tag{2.17}$$

Perfectly smooth surfaces have infinite correlation length. The Fraunhofer criterion for a surface to be considered smooth is expressed by the standard deviation of the surface height:

$$\rho_h < \frac{\lambda}{32\cos\theta} \quad , \tag{2.18}$$

where θ is the incidence angle and λ is the wavelength.

2.5 Volume Scattering

If the lower medium is dielectrically inhomogenous, additional scattering takes place within the lower medium. Such volume scattering is mostly non-coherent (in all directions) and is caused by random discontinuities at different layers within the volume [9]. The angular scattering pattern is a complex function of the distribution of discontinuities and their dielectric properties. An important parameter is the penetration depth D_p. If $P(y=0)$ is the power at the boundary, the power at depth y is:

$$P(y) = P(0)e^{-\int_0^y \chi(\xi)d\xi} \quad , \tag{2.19}$$

where χ is the extinction coefficient. The penetration depth is defined as depth D_p at which power decreases by factor $1/e$ from the $P(0)$:

$$P(y = D_p) = P(0)\frac{1}{e} \quad . \tag{2.20}$$

Approximate expression holds for most natural surfaces [42]:

$$D_p = \frac{\lambda\sqrt{\varepsilon'}}{2\pi\varepsilon''} \quad , \tag{2.21}$$

where ε' is real part and ε'' is imaginary part of the complex permitivity. The age of sea-ice, snow height, and soil moisture can be inferred from the estimated penetration depth.

Total scatter from natural targets combines contributions from both surface and volume scatter. Exact mathematical modeling is very involved [9,42] and exceeds the scope of this dissertation. Semi-empirical models are developed to characterize scattering signature as a function of various geophysical parameters. Soil moisture can be inferred from σ^o measurements if roughness effects are decoupled [17,40]. As another example, vegetation type can be recognized from primarily volume-backscattering coefficient if soil moisture is fixed. Snow parameters (water content, depth) can also be inferred from active microwave instruments [35]. Many more parameters can be monitored through σ^o measurements. σ^o signatures of several terrain types are shown on Figure 4.

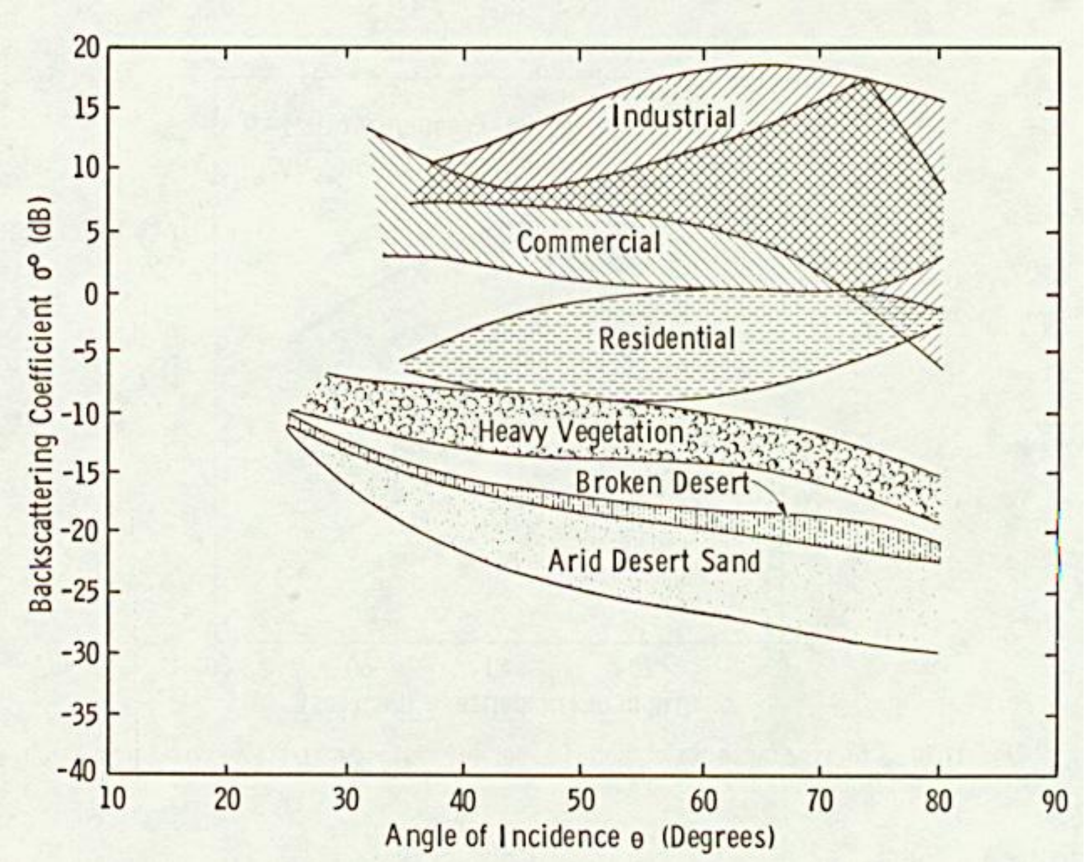

Figure 4: Backscattering signatures of several terrain types at 9.75 GHz

3 SCATTEROMETRY

3.1 Introduction

Near-surface wind vectors (both speed and direction) are a significant driving force determining local and global climate. Winds determine both small-scale events, such as tropical storms or hurricanes, and global-scale phenomena, such as El Nino, which is connected with the changed direction of the Pacific Trade winds. Wind vectors are significant inputs into existing numerical models for weather prediction. Because of such importance, accurate measurements of wind vectors are crucial in meteorology, which reaches far into many areas such as agriculture, traffic, tourism, etc. Earth climate is a global dynamical system. Therefore, global- coverage wind maps are required for accurate weather modeling. While wind observations over land are generally available, observing wind over oceans is a problem. Since oceans cover about 3/5 of the earth, the problem of wind estimation over oceans has to be addressed. This has been attempted in the past using voluntary ship report program. The approach suffered from a small frequency of observations and a non-uniform coverage. Figure 5 shows distribution of ship wind reports during three summer months in 1978. There is obvious bias in measurement distribution toward major shipping lanes, which are concentrated in the Northern Hemisphere. This leaves most of the Southern Hemisphere uncovered, making it insufficient input for global weather modeling.

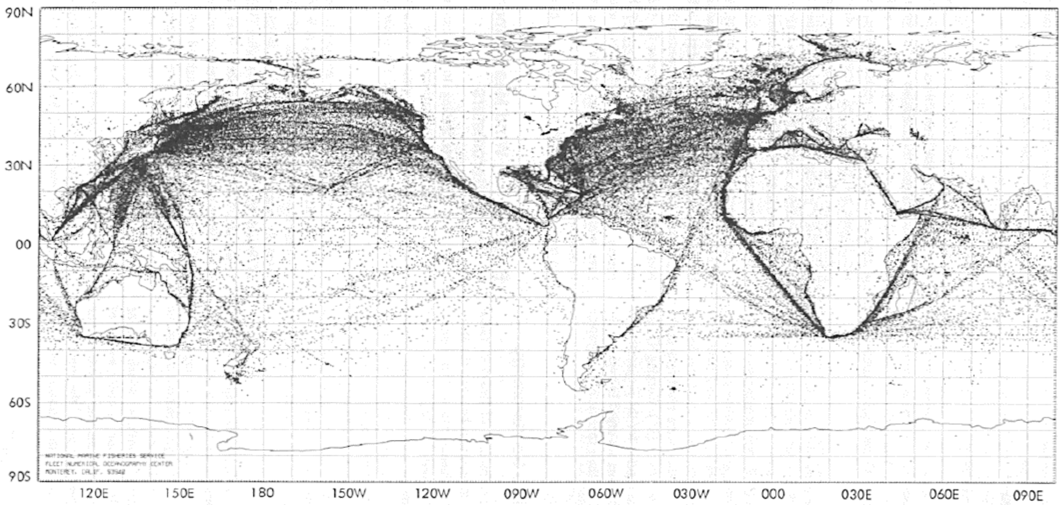

Figure 5: Distribution of ship wind condition reports during Jun-Sept. 1978

The idea to solve the problem of small frequency and biased coverage of wind observations using a spaceborne instrument is credited to Moore and Pierson [31]. They proposed usage of microwave radars on-board artificial satellites orbiting the Earth in low orbits (500-1000 km). Such instruments would have frequent, uniform, and global coverage. Operating at microwave frequencies (3-30 GHz) enables all-weather measurements because clouds are transparent for EM waves at these frequencies. Improved coverage of a spaceborne instrument is illustrated on Figure 6. It shows NASA Scatterometer instrument coverage in a 24-hour period. The advantage over ship observations is obvious: a spaceborne instrument provides more coverage in a day than all ships combined in a three-month period. The coverage of satellite is also uniform, which is equally important in global modeling as the extent of the covered area.

This chapter will present an introduction to satellite scatterometry. After explaining our motivation in the introduction, principles of scatterometry are discussed in

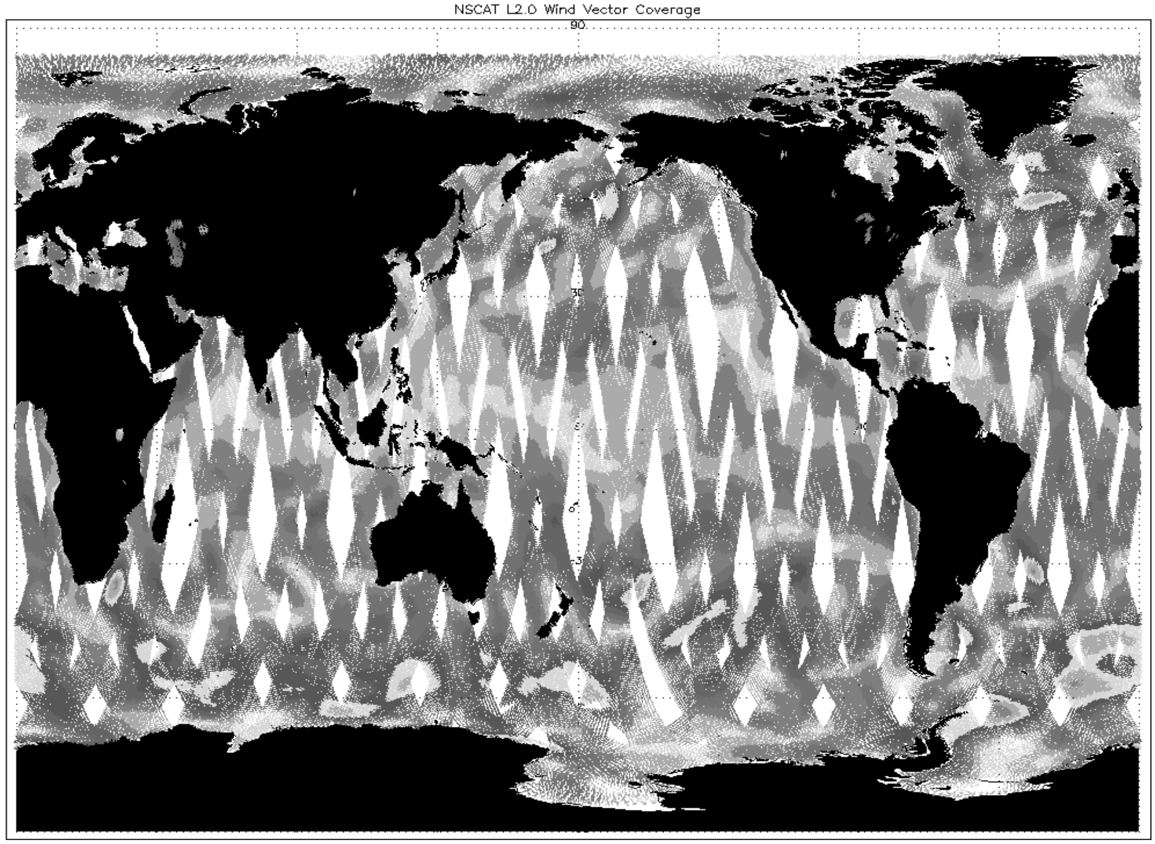

Figure 6: Coverage of the NASA Scatterometer during a typical 24-hour period

next section. Wind retrieval technique is introduced and illustrated with examples. History of scatterometry will include previously flown instruments. NASA Scatterometer is described in more detail followed by the data processing segment of the mission. The last section lists future scatterometer missions.

3.2 Principles of scatterometry

Satellite scatterometers are microwave radars used for measuring the normalized radar cross-section σ^0. The primary purpose of σ^0 measurements is near-surface wind estimation over oceans. Scatterometers are classified as non-imaging remote sensing radars (as spectrometers and altimeters [17]), as opposed to imaging category (moving antenna systems, real aperture, and synthetic aperture radars [12, 21]). Scatterometry is concerned exclusively with the signal amplitudes (no phase information). Amplitude σ^o measurements give useful information about a target, which can be expanded by varying other parameters, such as observing responses at different polarization, at multiple azimuth angles, or varying incidence angle. Although any radar calibrated for σ^o measurements is a scatterometer, the term is most often used for radars that measure σ^o as an intermediate step toward wind retrieval. Wind speed alone can be inferred by several other satellite instruments, such as radiometers [10, 32] or altimeters [17, 18]. It is the wind direction sensitivity that promotes scatterometers and gives them advantage. Studies are under way to detect if directional effects are present in radiometer measurements of the ocean brightness temperature. Besides wind retrieval from the scatterometer measurements over ocean, scatterometers are useful for various over-land applications [26, 42]. Soil moisture detection, vegetation type determination, and ice-edge detection, are among potential abilities of a scatterometer.

Wind scatterometers directly measure power reflected from the area illuminated by the scatterometer antennas. Scatterometers are calibrated radars and, as such, transmit pulses at microwave frequency and measure the amplitude of the return used in (2.4) to calculate σ^o. Scattering from the ocean surface is driven by resonant interaction of EM waves with capillary and short gravity waves. This phenomenon is referred to as Bragg scattering. As discussed in section 2.4, σ^o is determined, among others, by the surface roughness of the target. Sea-surface roughness is determined by the wind-induced waves.

This enables wind retrieval over sea surface from estimated σ^o. The retrieval is based on the relation between wind speed and direction pair, and σ^o. Wind vectors and σ^o are related through a geophysical model function [8, 13]:

$$\sigma^o = f(\vec{u}, \alpha, \theta, p, ...) \quad , \tag{3.1}$$

where $\vec{u}$ denotes wind vector, α denotes radar azimuth angle, θ is the radar incidence angle, and p denotes EM polarization. There are likely more variables affecting σ^o (sea-surface temperature, wave height, foam coverage, etc), but their effects are considered not significant and currently used model functions neglect them. These neglected parameters are denoted by ellipsis (…) in (3.1). Wind direction $\varphi(\vec{u})$ and azimuth are combined into relative wind direction:

$$\psi = \alpha - \varphi(\vec{u}) \ . \tag{3.2}$$

This reduces (3.1) into a four scalar variable function:

$$\sigma^o = f(|\vec{u}|, \psi, \theta, p) \ . \tag{3.3}$$

Attempts to provide an explicit functional expression to describe (3.3) did not produce satisfactory results. Table look-up approach is adopted, where 4-dimensional tables are empirically built [37, 43]. Recent studies employ neural networks as another way to derive geophysical model function [2]. Wind speed and direction are retrieved from the look-up table at known θ, p, and measured σ^o. There are multiple pairs of $|\vec{u}|$ and ψ that correspond to fixed θ, p, and σ^o. Therefore, multiple measurements are necessary to eliminate ambiguity in ψ.

An example of a geophysical model function is given on Figure 7. The Figure shows locus of possible σ^o values for three different wind speeds (5, 8, and 15 m/s), measured at θ=40^o incidence angle, by a vertically polarized beam. σ^o is plotted vs. relative wind direction ψ. This direction ambiguity is resolved by measuring σ^o from the same location at multiple azimuth angles. This would enable locating the unique solution

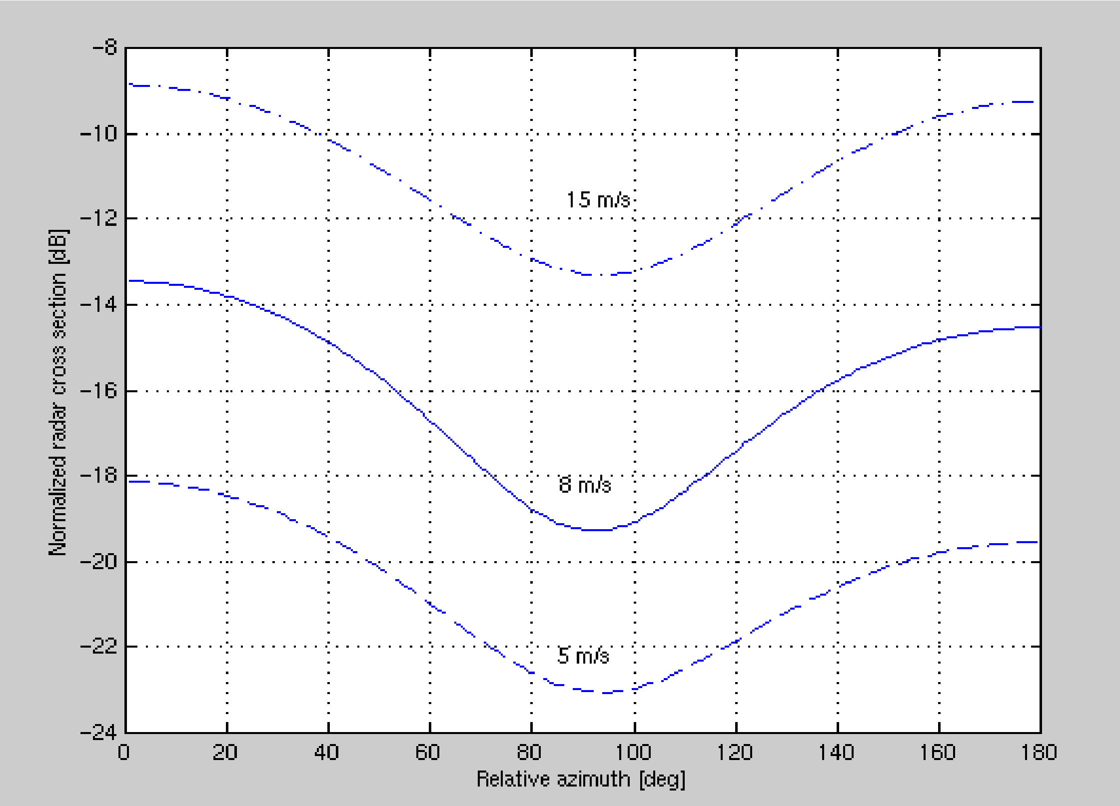

Figure 7: NSCAT 1 model function

at the crossing of individual $\sigma^o(\psi)$ loci (more details in section 4.2). Therefore, to be effective as both wind speed and wind direction sensors, scatterometers must measure σ^o at multiple azimuth angles. This requires multiple or articulating antennas as a part of a scatterometer.

3.3 History of scatterometry

While several air/space-borne instruments (radiometers, altimeters [18]) provide ocean-surface wind speed estimation, only satellite scatterometers give globally distributed, all-weather, and frequent measurements of both wind speed and direction [33, 34, 41]. Therefore, scatterometers are expected to become the main source of near-surface wind vector observations in the future. Several instruments have proven the abilities of a scatterometer in the past. The first space-borne scatterometer SL-193 flew on SKYLAB missions SL-2, SL-3, and SL-4. It produced only a single-azimuth-look measurement of radar cross-section. A single measurement was insufficient to resolve wind vector ambiguity. Thus, a radar signature of the globe, without independent wind determination capability, was the SKLYAB legacy in scatterometry. Advanced Aerospace Flight Experiment Radiometer/Scatterometer (AAFE RADSCAT [11]) in mid 1970s helped refine scatterometer design and geophysical model function [23], along with numerous small-scale airborne experiments.

The Seasat-A Satellite Scatterometer (SASS) proved the concept of retrieving oceanic wind vectors by estimating radar cross section from the measured reflected power. SASS, flown aboard the Seasat satellite from June to October 1978, operated in

Ku-band at 14.6 GHz. Four dual-polarized antennas (two at each side, Figure 8) allowed measurements at two azimuth angles (45^o and 135^o relative to the sub-track), with a nominal resolution of 50 km. The σ^o measurements from fore and aft antennas were combined to estimate wind speed and up to four wind directions. Despite a short lifetime of only 99 days for the Seasat satellite, SASS accomplishments were [1, 20, 22, and 24]:

1) SASS demonstrated that accurate (± 2 m/s and ± 20^o) measurements of wind speed and direction (up to four aliases) are obtained from scatterometer data.
2) The geophysical model function SASS-1 was built by correlating SASS data and "surface truth" measurements taken by the in-situ sensors.

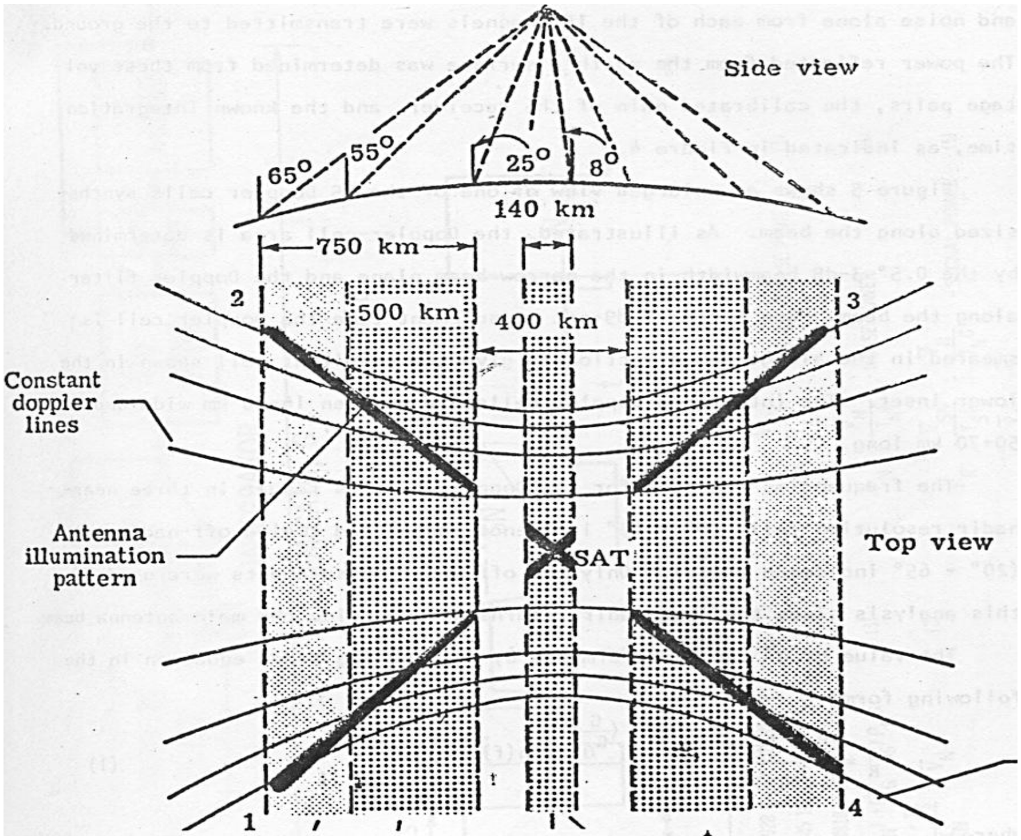

Figure 8: SASS antenna footprint geometry

3) SASS data were used to construct the first global maps of near-surface wind vectors.

Extensive analysis followed the SASS mission. The analysis validated principles of scatterometry, as a powerful wind measuring technique. Accuracy of σ^o measurements confirmed SASS sensor accuracy. Comparing winds retrieved by SASS, with in-situ observations, validated the SASS geophysical algorithm [24].

The European Remote Sensing Satellite Wind Scatterometers (ERS-1 and ERS-2 WSC) was launched in 1991 and 1996 by the European Space Agency ESA, operate in C-band at 5.3 GHz. ERS WSC is flying in a near-polar, Sun-synchronous orbit at mean altitude of 785 km and inclination angle of 98.5^o. The geometry of ERS-1 WSC is shown in Figure 9. Three fan-beam vertically polarized antennas are pointed 45^o, 90^o, and 135^o to the satellite flight path. The incidence angles range from 18^o to 59^o. Resolution of about 50 km is achieved using range-gating technique [3]. ERS-2 WSC is still operational covering 90% of the Earth’s surface every 5 days. Relatively smaller coverage is the consequence of a single-side, 500-km wide swath. It operates discontinuously because the Synthetic Aperture Radar (SAR [12]) and the Scatterometer are operating in a time-shared mode. The same instrument (Active Microwave Instrument AMI) operates in three modes. In the image mode, AMI is a 30-meter resolution SAR with high data rate of 105 Mb/s. The image mode is active only during line-of-sight communication with an ERS-1 ground station. In the wave mode, AMI operates as a combined SAR/scatterometer, but on a decreased data rate of 345 kb/s. Lower data rate is due to lower resolution, which is still sufficient for imaging the ocean wave patterns. AMI becomes scatterometer in the wind mode, which is active over ocean surfaces.

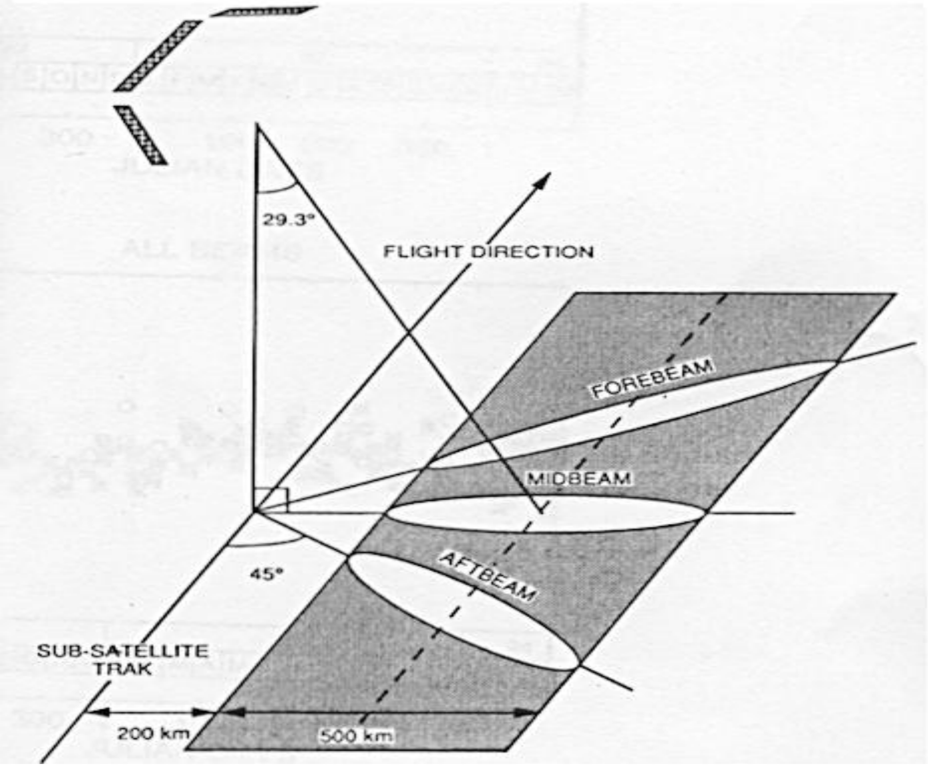

Figure 9: ERS-1 WSC antenna geometry

Significant difference between C-band ERS-1 WSC, and Ku-band SASS and NSCAT, is in the scattering regime. While C-band scattering from the ocean surface is primarily driven by the short gravity waves, Ku-band wavelengths are scattered by both short gravity and capillary sea waves. In addition to surface scattering, C-band wavelengths penetrate into volume and experience volume scattering as well. Despite different mechanisms, C-band model function is similar to a Ku-band model function. It is illustrated in Figure 10 showing C-band CMOD 4 model function [2] used for ERS-1 WSC and SASS 2 model function [37, 43] used for SASS wind retrieval. The figure is given for vertical polarization, 40^o incidence angle and 8 m/s wind speed.

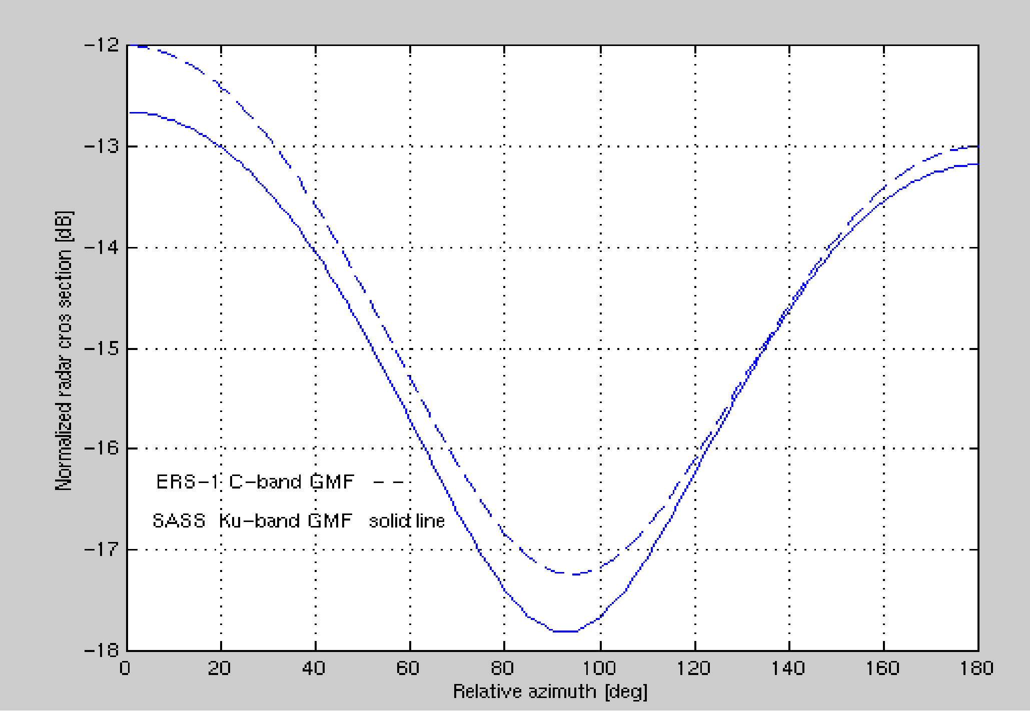

Figure 10: A comparison between ERS-1 and SASS 2 model functions

3.4 NASA Scatterometer

Built on the SASS experience, NASA Scatterometer (NSCAT) has been the latest satellite scatterometer. It was originally designed to fly on NROSS satellite. The NROSS project was cancelled and NSCAT design was modified to fly on-board the Japanese Advanced Earth Observing Satellite (ADEOS). ADEOS was launched August 17, 1996, and was lost on June 30, 1997 due to a failure of power generating solar panels. Besides NSCAT, ADEOS carried a payload of scientific instruments designed to measure global climate change including: Ocean Color and Temperature Scanner (OCTS), Advanced Visible and Near Infrared Radiometer (AVNIR), Total Ozone Mapping Spectrometer (OCTS), the instrument for measuring Polarization and Directionality of the Earth's reflectance (POLDIR), Interferometer for Monitoring Greenhouse gasses (IMG), and

Improved Limb Atmospheric Sounder (ILAS) [34]. In the 10-month lifetime, NSCAT collected huge amount of valuable data and, before the spacecraft failure, showed unprecedented stability and sensitivity to geophysical variables. Unfortunately, the premature end of the mission did not enable desired studies of seasonal and inter-annual variations. NSCAT mission requirements were to measure wind speeds with 2 m/s or 10 % (whichever greater) accuracy in the range 3-30 m/s. Accuracy in the retrieved wind direction was required to be 20^o. Spatial resolution requirements were 25 km for σ^o cells with multiple cells combined into 50-km wind cells with location accuracy of 25 km. The planned duration was 36 months and except for this, NSCAT successfully met these requirements.

ADEOS flew in a near-polar, Sun-synchronous orbit with 98.5^o inclination angle and at altitude of 795 km. NSCAT had six 3-meter long antennas. Antennas were slotted waveguide-array fed horns. Horns were producing fan beams with beamwidths of 25^o (elevation) and 0.4^o (azimuth). Beams were pointed 45^o, 115^o, and 135^o relative to the satellite subtrack. The NSCAT instantaneous antenna footprint geometry is shown on Figure 11. The 300-km nadir gap in the middle corresponds to incidence angles below 20^o. σ^o measured at these low incidence angles is insensitive to wind speed nor direction. Thus, this part of the fan beam is unusable for wind retrieval and only measurements at 10^o are taken to monitor antenna gain. Usable incidence angles ranged between $\approx 20^o$ (near swath, 150 km from the satellite sub-point) and 60^o (far swath, 750 km from the satellite sub-point). Future conical scanning scatterometers will remove nadir limitations.

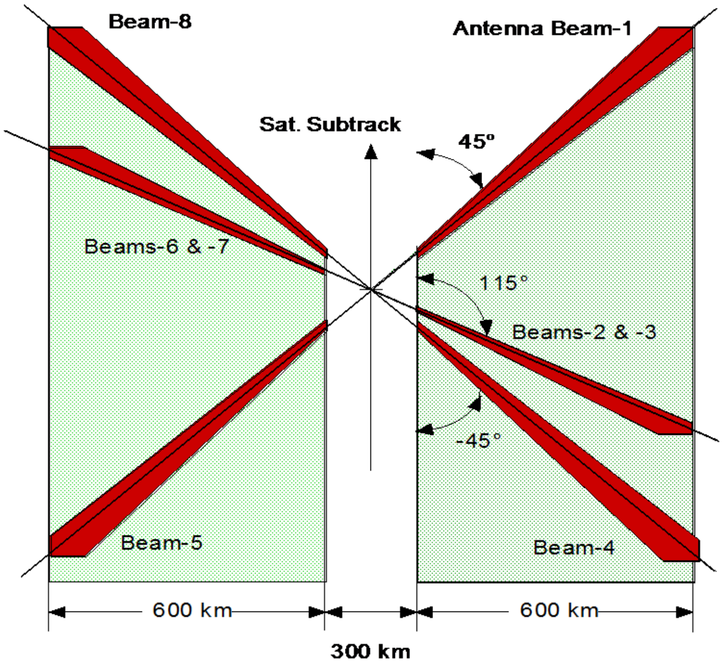

Figure 11: NSCAT antenna footprint geometry

NSCAT used two orthogonal linear polarizations. Middle antennas were dually polarized with beams 2 and 6 being vertically polarized and beams 3 and 7 horizontally. Fore (1 and 8) and aft (4 and 5) beams were vertically polarized. Subtracks of each beam were resolved into 24 along-beam cells using on-board Doppler filtering [34]. Along-track resolution was achieved using measurement timing. σ^0 resolution cells were 25 km along-beam (cross-track) and several km (up to 7) along-track. The σ^0 cells are defined by the combined effect of the 3-dB Doppler filter bandwidth and antenna beamwidth [34]. By combining up to 4 X 4 σ^0 observations taken at three different azimuth angles (Figure 12), NSCAT improved wind direction determination capability over SASS that had only two azimuth looks.

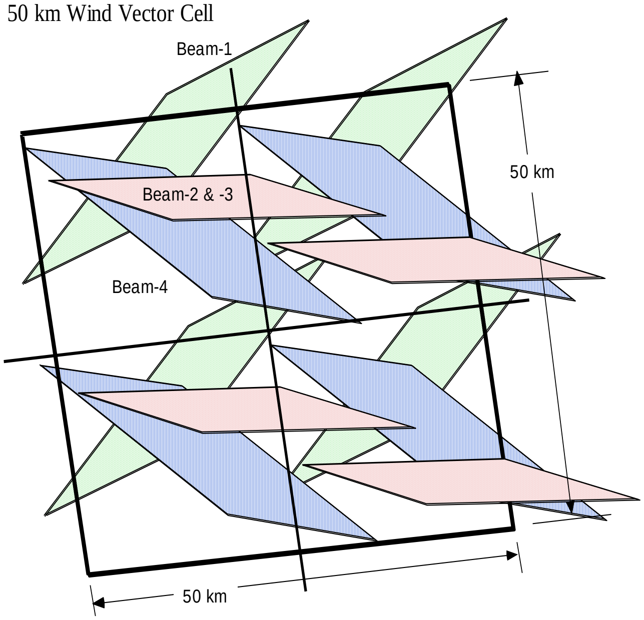

Figure 12: Wind vector cell

NSCAT sequenced through all eight beams within 3.74 s. Since transmit/receive cycle is 16 ms, as many as 29 measurements of returned power contribute to a σ^o estimation ($\frac{1}{8}\frac{3.74}{0.016} \approx 29$). There are four noise-only measurements leaving 25 signal + noise. Returned power is estimated by subtracting noise-only from the signal + noise measurements. Powers are calculated by summing appropriate periodogram bins from the 4-channel on-board digital Doppler processor.

The NSCAT hardware was based on the SASS design, with several important improvements. A simplified block diagram is shown on Figure 13. Transmit signal at 13.995 GHz is generated by a stable local oscillator (STALO) and frequency up-converters. The signal is amplified by a travelling wave tube amplifier (TWTA). There are two independent TWTA's, one of which is fully redundant. Circulator and switching matrix (SM) are used to route signal to antennas. In the reception path, the received signal is routed from the antennas to a 5-stage GaAs FET low noise amplifier (LNA). The amplified signal is split into four channels and down-converted to baseband frequency. The baseband signals are input into digital Doppler processor (DDP). The primary objective of the on-board Doppler processor is to achieve along-beam resolution, based on spatially dependent Doppler shift of the returned signal (section 2.3). Digital Doppler processor accounts for relative motion of the rotating Earth by adapting filter bandwidths and center frequencies as a function of latitude. This is significant improvement over the SASS analog processor that had fixed filters and therefore highly varying σ^o cell dimension, depending on the latitude. The NSCAT Doppler processor is a 16-bit FFT processor capable of computing seven complex 512-point FFT's in 16 ms. This reduces downlink data rate through the telemetry antenna (TA) by a factor of 2500. A calibration noise source was also included in the receiver. It was a tunnel diode (TN) with 20500 K noise temperature. The diode output was periodically switched and fed into LNA to serve as a stable reference to monitor the receiver gain. Data were downlinked to the Earth station and transferred to the ground data processing segment at the Jet Propulsion Laboratory (JPL) in Pasadena. The ground data processing segment was responsible for telemetry-to-engineering unit conversion, geometry calculation and cell co-location, σ^o estimation from power measurements, inversion of model function, and ambiguity removal to select the wind vector. The final product was 0.5^o X 0.5^o daily wind field maps.

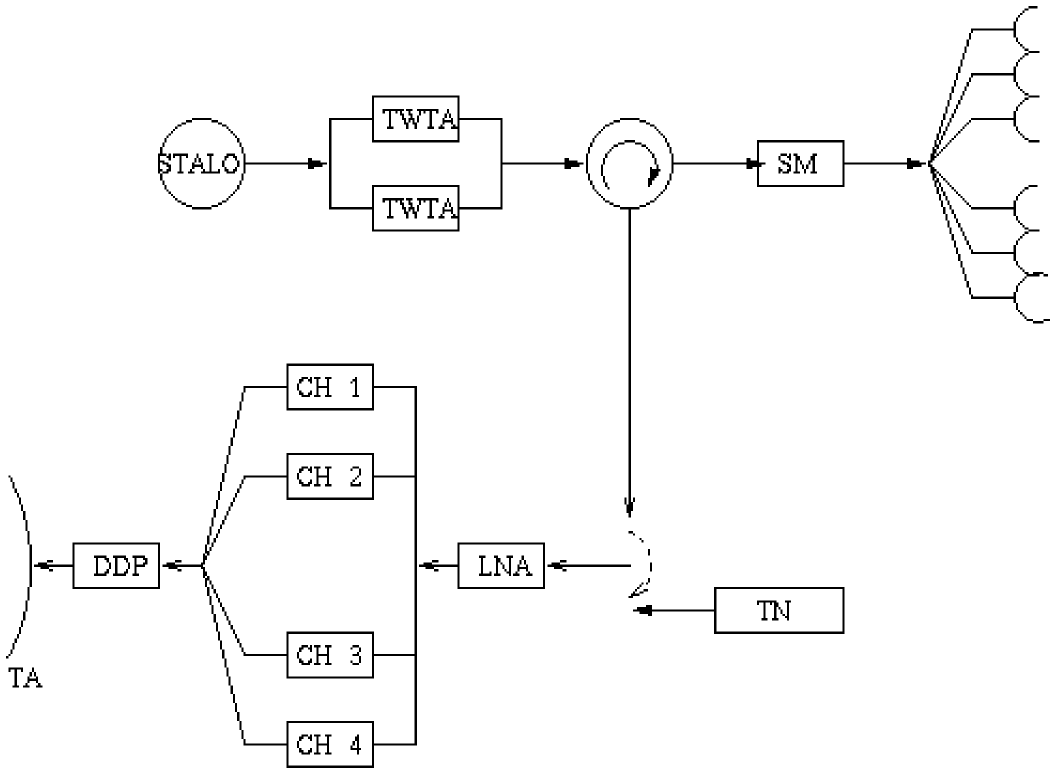

Figure 13: Simplified NSCAT block diagram

3.5 NSCAT data processing

NSCAT scientific data processing is based on the Algorithm Testbed, written mostly by Dr. Scott Dunbar at JPL [16]. Realized in FORTRAN, the testbed takes spacecraft and instrument telemetry as the input and processes it through several stages into the final product: retrieved wind vectors. Processing and data are divided into levels, designated as:

- Level 0: Time-tagged raw spacecraft and instrument telemetry
- Level 1: Instrument data converted from raw binaries into engineering units

- Level 1.5: Earth-located σ^o data with surface flag assigned using Central Intelligence Agency (CIA) world map
- Level 1.7: σ^o and associated data collocated in wind vector cells (Figure 12)
- Level 2.0 Earth-located wind vector ambiguities ranked by likelihood, with ambiguity removal process identifying selected vector

Manipulating data through these levels is illustrated on Figure 14. It starts from Level 1.0 to Level 1.5 processing. Raw telemetry is converted into engineering units. Data are divided into revolution files (≈ 20 MB, binary). The spacecraft state vector is computed from ephemeris file generated off-line. There are six state variables, each using an eight-order polynomial for interpolation. Level 1.0 to Level 1.5 includes sensor data processing. There are three groups of algorithms at this processing level: Geometry algorithms, Land and ice flag algorithms, and σ^o and standard deviation algorithms. General geometry is calculated through series of coordinate transformations. Antenna geometry sub-module calculates maximum gain direction, antenna angle and cell gain. Cell centers, cell area, slant range (distance between the satellite and the cell center), azimuth and incidence angle, are calculated in the Cell Geometry sub-module. Doppler binning sub-module assigns frequency bin number for each σ^o cell, which is crucial for resolution and σ^o grouping accuracy. Uncertainties in geometry calculation are computed to weight individual σ^o measurements. Sub-track binning indexes are assigned to σ^o cells, and are used in grouping algorithm. Land and ice flags are required to exclude affected σ^o measurements from the wind retrieval. Land flag is assigned according to coarse and fine comparisons with the "CIA World Data Base I" world map [16]. Ice flags are set from the daily inputs from the National Oceanographic and Atmospheric Agency (NOAA) and Navy Joint Ice Center. Initially planned rain flagging was not available since radiometer (rain detector) was not onboard the ADEOS. The core of the sensor data processing is σ^o and normalized standard deviation (K_p) calculation. σ^o is calculated using the radar equation. K_p is calculated from geometry uncertainties. σ^o measurements with lower K_p are weighted more in the wind retrieval. Level 1.5 to level 2.0 processing includes geophysical processing algorithms. Individual σ^o measurements are first regrouped from

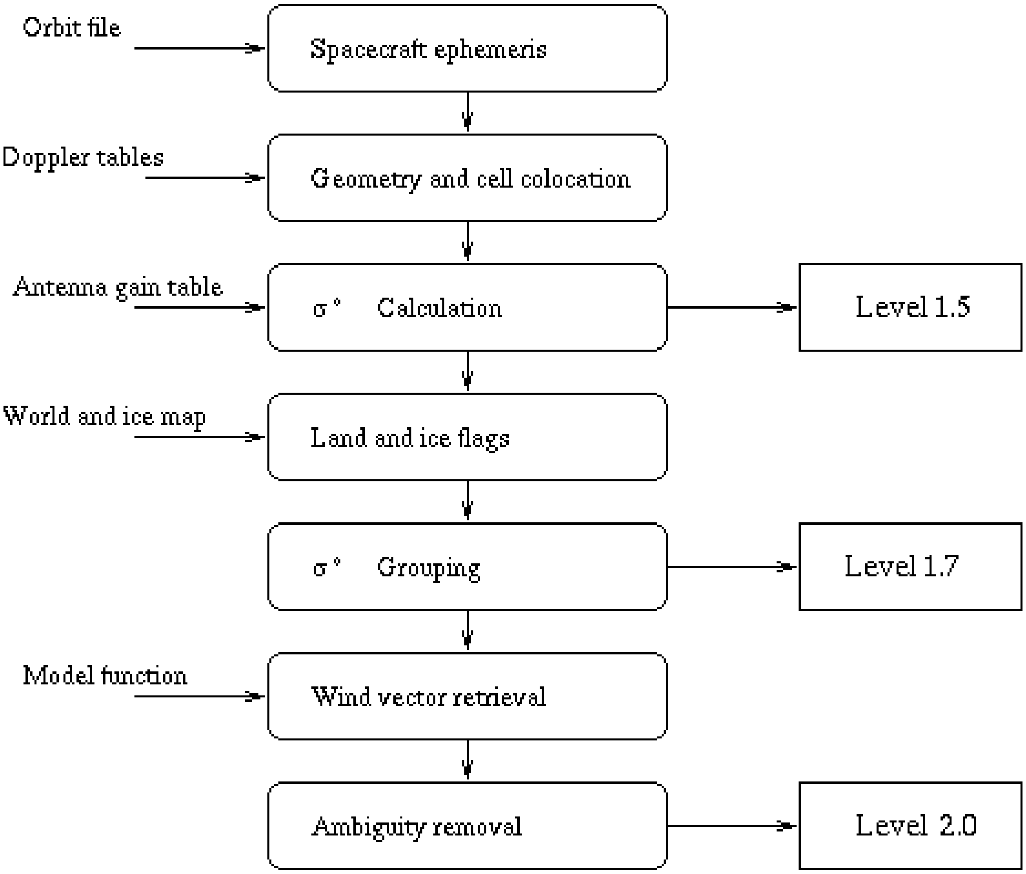

Figure 14: NSCAT data processing flow chart

the time-ordered into spatially-ordered sets. The grouping is based on sub-track indexes assigned at Level 1.0 to Level 1.5 processing. Grouped σ^o data are denoted as Level 1.7 data and intermediate files are generated (≈ 8 MB, binary). Wind retrieval algorithm uses maximum likelihood estimation (MLE). The cost function is:

$$J(u,\psi) = \sum_{i=1}^{N} \frac{(\sigma_m(u,\psi,\theta_i,p_i) - \hat{\sigma}_i)^2}{K_{p,i}\sigma_i} \quad , \tag{3.4}$$

where σ_m is the model function value corresponding to speed u, relative wind direction ψ, incidence angle θ_i and polarization p_i. $\hat{\sigma}_i$ is measured at θ_i incidence by a p_i - polarized beam. The MLE procedure calculates $J(u,\psi)$ for each (u,ψ) pair and assigns the highest probability to arguments of the minimum J value. Multiple (u,ψ) pairs are ranked by their MLE probabilities. From these (up to four) pairs (aliases), the unique wind vector is selected using the median filter data processing technique. The de-aliased wind vector and auxiliary data are organized in Level 2.0 files (≈ 800 KB, binary). Level 2.0 data files are the final geophysical products of the NSCAT processing.

The most relevant data level for beam balancing is the Level 1.5. It contains all required variables for inter-beam calibration. Level 1.5 record structure is given in Appendix B.

3.6 Future scatterometers

Future satellite scatterometer missions include SEAWINDS, scheduled for launch on ADEOS II spacecraft in 2001. SEAWINDS is a conical-scan scatterometer. Conical scanning will eliminate nadir gap (300 km for NSCAT, Figure 11), thereby increasing swath to 1800 km. Daily coverage will be subsequently increased to 92 % of the globe. Up to four azimuth looks will be available at a location cell. SEAWINDS will transmit horizontally polarized short pulses at 13.4 GHz. Beams will be incident at angles of 42^{o} and 54^{o}. Signal-to-noise ratio of 5-25 dB will be higher than -20 - +18 dB for fan beam scatterometers. Conical scan will enable parallel use of radiometer to account for some rain-related effects on scatterometer response. The only disadvantage will be complex moving antenna, required for conical scan.

To bridge the gap between NSCAT and SEAWINDS, JPL is building the Quikscat scatterometer. Quikscat is scheduled for November 1998 launch. It will utilize a rotating dish antenna with two beams of the same design as SEAWINDS. It will transmit at the same frequency of 13.4 GHz. The swathwidth of 1800 km will generate ≈ 400 000 measurements per day. European space agency is also planning follow-ups to successful ERS-1 and ERS-2 WSC. Orbiting multiple scatterometers at the same time would enable comparisons and further development of this technology that is expected to become a main tool for monitoring global wind conditions.

4 NSCAT CALIBRATION

4.1 Introduction

In addition to radars designed specifically to measure σ^o of illuminated surface, any other radar (imaging radar, altimeter, etc.) can serve as a scatterometer, as long it is calibrated for the scattering measurements. Three issues are important in all scatterometer applications: determination of the covered area, obtaining enough independent samples, and calibration. This dissertation addresses the third issue, calibration of a satellite scatterometer, specifically the NSCAT. The proposed calibration method is relative, aimed at eliminating inter-beam biases. The removal of beam biases permits precise measurements. For accurate measurements, absolute calibration is required. Absolute calibration requires knowledge of the true σ^o value. Relative calibration alone is sufficient to follow main target characteristics inferred by the same instrument. Effort involved in absolute calibration is necessary only when comparing results from different instruments. Absolute calibration relies on "hard" targets, with known σ^o. For few such targets, σ^o can be analytically expressed. Analytical treatment of an extended natural target is too involved, due to enormous number of point scatterers with random phases (chapter 2). Therefore, relative calibration is planned for satellite scatterometer missions, while absolute calibration is performed through local surface truth experiments (aircraft overflights, buoy comparisons, etc.).

This chapter proposes a simple and fast method for relative calibration of the NSCAT. Following the introduction, the goal of calibration is stated. Calibration method using extended area target is formulated. Data sets are selected and tested. Results are presented and compared with the accepted NSCAT calibration corrections. The simple method is shown to produce a set of corrections that make σ^o measurements consistent among all beams.

4.2 The goal of scatterometer calibration

As long as relative calibration is maintained, a scatterometer can serve for most applications, including wind vector retrieval. Multiple-azimuth measurements are required for many applications. In wind vector retrieval, multiple-azimuth looks are needed to resolve wind direction ambiguity [44] (as explained in section 3.2 and illustrated on Figure 7). NSCAT overlaps σ^o measurements from three azimuths (Figure 12). Combining model functions from four σ^o measurements (3 antennas, one of which is dual-polarized), four loci of possible $\sigma^o(\psi)$ intersect at the point of the de-aliased relative wind direction ψ (ψ= azimuth - true wind direction). This mechanism is illustrated on Figure 15, where NSCAT 1 geophysical model function response from NSCAT vertically-polarized beams is plotted at 40^o incidence angle, and assumed north wind of 8 m/s. Accepted convention is to assign 0^o wind direction to the north wind. Figure 15 also shows the advantage of the three-azimuth NSCAT over SASS, which had two azimuth looks (Figure 8). Third azimuth helped remove ambiguity caused by multiple (up to four) intersections of two loci. The intersection of three loci is clearly at the point of the assumed wind (8 m/s, 0^o). Figure 15 is plotted for idealized noise-free measurements. Real measurements will be corrupted by noise, which will move loci of individual beams. Translation of loci, caused by noise, will prevent the intersection point to be clearly identifiable. Therefore, NSCAT wind retrieval algorithm relies on the maximum likelihood estimation (MLE). The MLE algorithm [16, 34, 37] finds the point in the model function look-up table that minimizes sum of differences between model function and measured σ^o from all beams. The vector with the highest likelihood is not necessarily the true wind due to noise. The wind vectors with assigned likelihoods are rather inputs into ambiguity removal algorithm. Based on median filter [34], the ambiguity removal completes the wind vector retrieval.

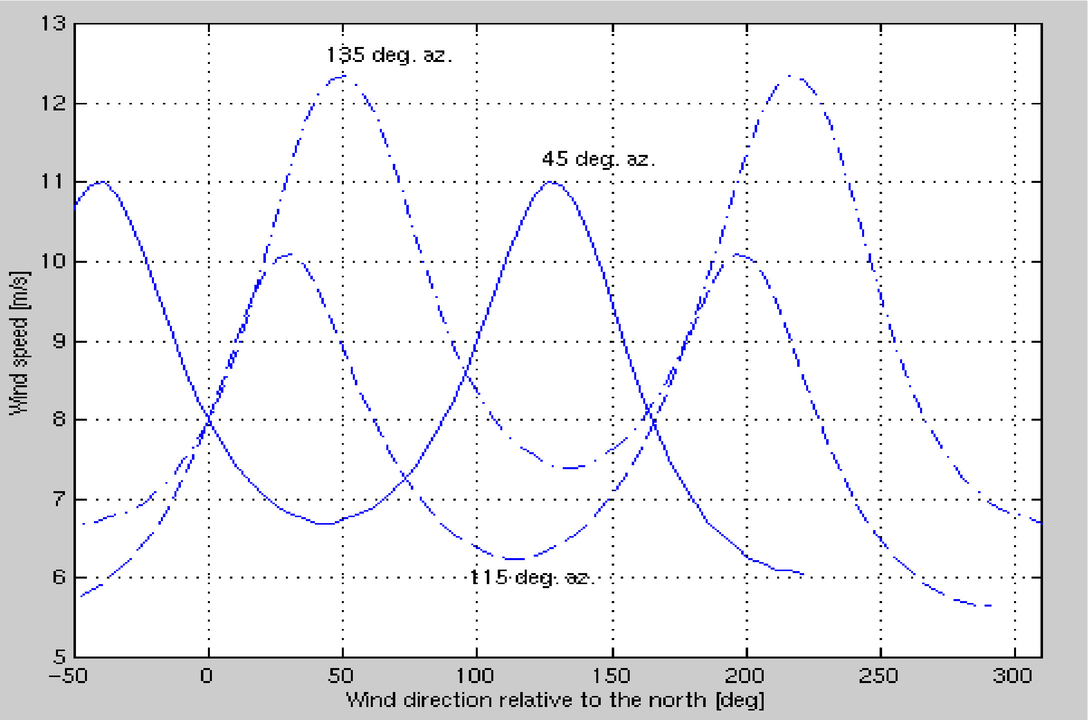

Figure 15: Loci of possible wind vector solutions retrieved from σ^o measurements taken at 40^o incidence by three vertically polarized NSCAT beams.

In addition to random noise, systematic biases in NSCAT beam gains also introduce ambiguity in Figure 15, and shift the intersection point from the true wind solution. Any one or more of biased beams will translate it's $|\vec{w}|(\psi)$ curve and cause inaccurate retrieval. This necessitates NSCAT antennas to be well calibrated. The σ^o calibration must be within few tenths of a dB to meet NSCAT requirements (± 2 m/s or 10 % wind speed and ± 20^o wind direction accuracy in 3-30 m/s range). The antennas are calibrated to within 0.25 dB pre-launch at the JPL cylindrical near-field range [34]. The range consists of a turntable on which antenna is mounted and fed, moving near-field probe and a network analyzer. The assembly is computer-controlled and placed in an anechoic chamber. Temperature sensors are mounted within the NSCAT antenna subsystem to allow on-orbit correction of gain changes due to thermal variations. The gain is additionally controlled by the calibration noise source (noise tunnel diode TN on Figure 13). It is a highly stable power source, used to provide reference to compute the receiver path gain. Transmitted power is also monitored to ensure proper input into radar equation (P_t in equation 2.7). All these hardware measures are aimed at internal calibration. However, careful pre-launch calibration alone is not sufficient for the desired σ^o calibration level [26, 30]. Therefore, post-launch, on-orbit scatterometer calibration/validation activities are planned for scatterometer missions.

The goal of on-orbit relative calibration is to make measurements from all beams consistent among themselves. NSCAT ground processing algorithm calculates σ^o by inverting modified radar equation for extended natural targets (2.7):

$$P_r = \frac{P_t L \lambda^2}{(4\pi)^3} \iint_A \sigma^o \frac{G^2(x,y) F(x,y)}{R^4(x,y)} dA \ , \qquad (4.1)$$

where:

P_r: Measured reflected power received by NSCAT antennas

P_t: Power transmitted by NSCAT antennas

L: System losses (estimated and measured)

λ: Wavelength of transmitted radiation

$G(x,y)$: Antenna gain at point (x,y) on the surface

$F(x,y)$: Doppler filter gain at point (x,y)

$R(x,y)$: Slant range between NSCAT and point (x,y)

dA: Infinitesimal area $dA=dxdy$.

A: NSCAT σ^o cell area (≈ 25 X 7-11 km)

Inverting (4.1), the NSCAT algorithm estimates σ^o as:

$$\sigma^o = P_r K(G,A,R) \left[A P_t \left(\frac{G_p \lambda}{4\pi R^2} \right)^2 \frac{L}{4\pi} \right]^{-1} , \qquad (4.2)$$

where $K(G,A,R)$ is pre-calculated coefficient that approximates double integration in (4.1) and depends on the gain G, cell area A, and distance between NSCAT and the cell center R. G_p is the peak gain. The scatter in σ^o is described by the normalized standard deviation of σ^o measurements:

$$K_p = \frac{\sqrt{\mathrm{var}(\sigma^o)}}{\sigma^o} , \tag{4.3}$$

where *var(x)* denotes the variance of noisy measurements of *x*. Following Long [30], the K_p factor can be decomposed into three independent parts:

$$K_p = K_{pc} + K_{pr} + K_{pm} . \tag{4.4}$$

Kpc denotes the contribution of the communication error. It is a function of signal-to-noise ratio (*SNR*), determined by the instrument design, geometry and the value of σ^o. *Kpc* is inherent in the measurements and is not affected by the calibration. *Kpr* is the normalized standard deviation due to uncertainties in the values of the radar equation (4.2). The relative calibration aims to reduce biases in these parameters among the beams. *Kpm* quantifies contributions of target variability. It includes the effect of all geophysical parameters other than wind speed and direction (denoted with … in (3.1)). *Kpm* also contains effects of varying wind speed and direction within a single wind vector cell. To reduce *Kpm*, the calibration target must be carefully chosen to exhibit σ^o stability. Targets considered for scatterometer calibration, exhibit low *Kpm* factor.

NSCAT ground processing algorithm calculates *Kpc*, *Kpm,* and *Kpr* separately. A suitable approximation for the total normalized standard deviation (4.3) is [30]:

$$K_p = \frac{1 + 2/SNR + 1/SNR^2}{\sqrt{N_p T_p B_c}} , \tag{4.5}$$

where:

SNR: measurement signal-to-noise ratio

N_p: number of transmitted pulses accumulated into one σ^o measurement

T_p: transmit pulse length in seconds

B_c: cell bandwidth in Hertz

Suitable choice of parameters in (4.2) during scatterometer design decreases K_p pre-launch. The goal of the on-orbit calibration is to further reduce K_p by eliminating relative biases among measurements from different antennas. Reducing the K_p parameter is the equivalent to reducing the scatter in σ^o measurements.

4.3 Homogenous land target calibration method

Several methods have been used for on-orbit scatterometer calibration: homogenous land targets, ground stations, and global ocean surfaces. The simple method formulated in this section uses homogenous land targets. Suitable targets for calibration of a scatterometer must exhibit azimuth-independent and temporally stable radar response over large area. Consistency among measurements taken at the same incidence angle by all beams is expected for such a target. Most of the land surfaces exhibit small azimuthal effects. Surfaces with the lowest effect are used for scatterometer calibration. Birrer et. al, [7] proposed maximum likelihood estimation algorithm over a homogenous land target to remove SASS beam biases. He suggested using the method real-time during an NSCAT-like instrument mission. The choice of potential sites is discussed by Kennet and Li [26]. They showed Amazon and Congo tropical rainforest regions to be homogenous over large area. A study of ERS-1 scatterometer applications over land is given in [19] and includes results for Amazon and Congo basins. They confirm homogeneity and negligible azimuthal effects of these targets for C-band.

In this dissertation a simple method is employed which uses homogenous land targets and polynomial model of σ^o response. For any land target, σ^o at the given polarization is a function of location, time, azimuth, and incidence angle. Calibration targets exhibit azimuth-independent response, uniform at a given incidence angle over a large area. Diurnal effects are expected for natural targets, but repeatable response at the same time of day is required to enable grouping sufficient data (multiple passes) into a calibration set. Being a Sun-synchronous satellite, ADEOS subtrack crosses Equator around 10 a.m. (descending) and 10 p.m. (ascending). Repeatable response at these times removes time-dependence if data are separated into ascending and descending passes over the target. Only incidence angle remains a variable. The algorithm formulated here further eases uniform response requirement by dividing large target into smaller location elements. This is a novel approach to strengthen the spatial homogeneity assumption. As area of an element becomes smaller, uniformity assumption becomes stronger. Beam biases on the other hand should not vary with the location element. The only limitation is time required to collect enough data within the location. This time must be long enough to ensure proper modeling, but short enough not to include seasonal effects in the target's response. This results in a trade-off between the size of a homogenous location element and algorithm convergence time: more passes will be needed for smaller location elements to collect enough measurements.

Following Long [30], a *p*-order polynomial is adopted as the model for incidence angle response. The target is divided into *M* location elements. The response from a point within location element *l*, to beam *b* is:

$$\hat{\sigma}_b^o(\theta) = \sum_{i=0}^{p} a_{i,b,l}\vartheta^i + noise \ , \tag{4.6}$$

where $\vartheta = \theta - 40^o$ is taken for numerical stability reasons (40^o is the mean NSCAT incidence angle). Polynomial coefficients $a_{i,b,l}$ are calculated regressing data falling in the same bin defined by the beam, location and the incidence angle. In order to estimate coefficients a, a sufficient number of instantaneous measurements per bin must be collected. The zero-mean noise term is due to uncertainties of parameters in (4.2) and communication noise.

Averaging responses from all beams, the reference set of polynomial coefficients ($A_{i,l}$) becomes:

$$A_{i,l} = \frac{1}{8}\sum_{b=1}^{8} a_{b,i,l} \ , \quad i=1..p. \tag{4.7}$$

Mean incidence angle response at location element *l* is:

$$\overline{\sigma}_l^o(\theta) = \sum_{i=0}^{p} A_{i,l}\vartheta^p \ . \tag{4.8}$$

Corrections required to remove biases in individual beams will force individual beam response to the reference given by (4.8). For beam *b* and location *l*, the required correction is:

$$c_{b,l}(\theta) = \frac{\overline{\sigma}_l^o(\theta)}{\hat{\sigma}_{b,l}^o(\theta)} \quad . \tag{4.9}$$

Biases of an individual beam can not depend on the location element observed. Therefore, averaging corrections from location elements, the corrections to be applied to beam *b* become:

$$c_b(\theta) = 10\log_{10}\left\{\frac{1}{M}\sum_{l=1}^{M}\frac{\overline{\sigma}_l^o(\theta)}{\hat{\sigma}_{b,l}^o(\theta)}\right\} . \tag{4.10}$$

The corrections calculated by (4.10) need to be added (in log space) to instantaneous $\sigma^o(\theta)$ measurements to achieve consistency among beams. Therefore this is a relative method. It forces measurements from individual beams to the mean $\overline{\sigma}_l^o(\theta)$ response from all eight beams (4.8). The method is simple and produces calibration corrections in a relatively short time necessary to collect enough measurements for reliable polynomial modeling. By adjusting $\overline{\sigma}_l^o(\theta)$ to independently determined true value $\sigma_{true}^o(\theta)$, absolute calibration can be achieved. The summary of the formulated method is given in a form of the block chart on Figure 16.

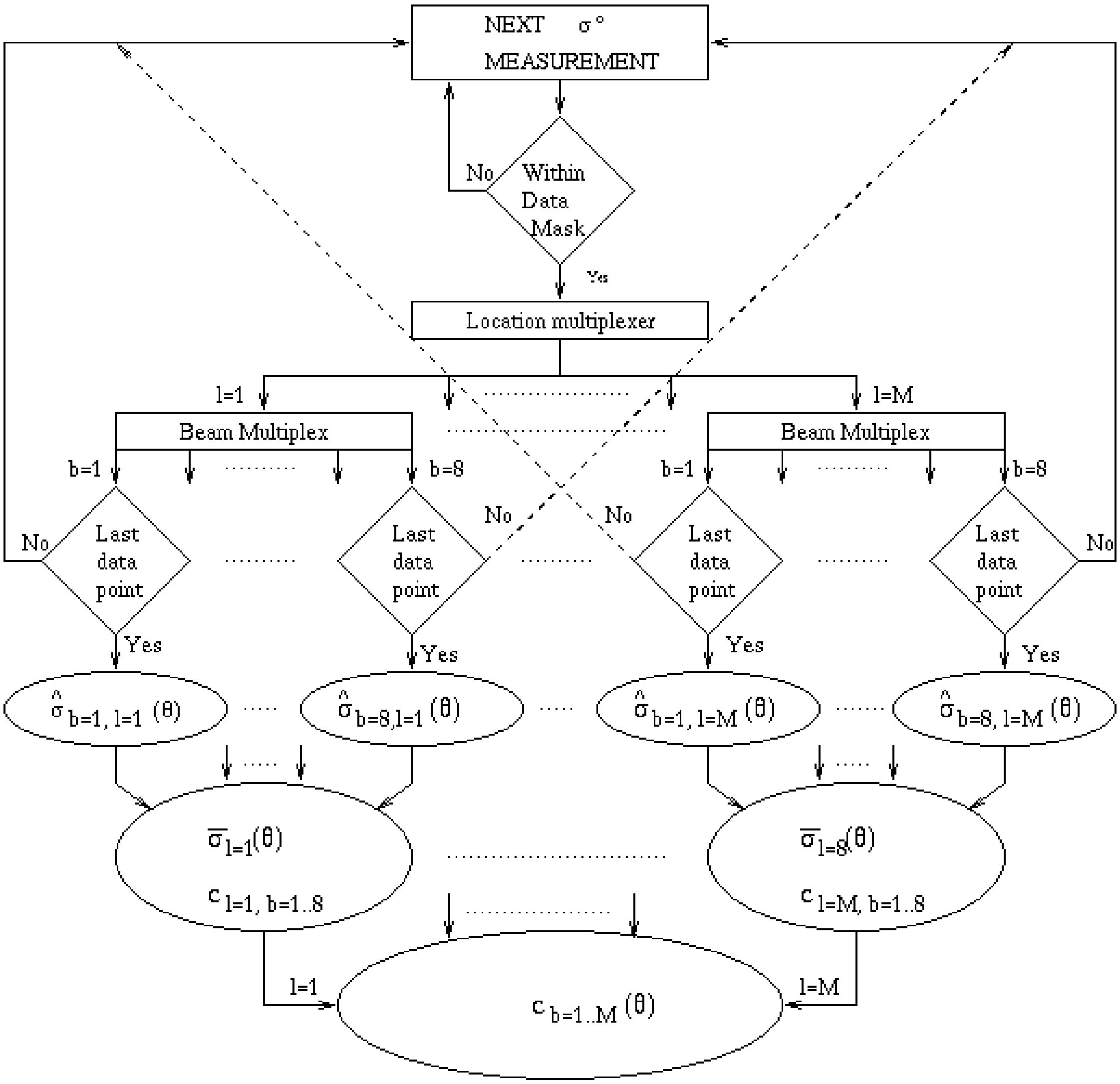

Figure 16: NSCAT Calibration flow chart

4.4 Calibration data

Amazon rainforest is a region dominated by dense tree canopies. The region is subject to relatively small seasonal effects, due to it's Equatorial location. In contrast to cultural vegetation (often fields with regular patterns), such natural vegetation is randomly distributed, both spatially and in height. While experiments were conducted over cultural vegetation and some analytical models exist [42], few studies cover backscattering from tree canopies. This is because of more complicated logistics required for tree canopies. Most terrain surfaces have been investigated using ground/truck-based equipment, which is not applicable, particularly for tall tree canopies. Another factor is that sufficient spatial and temporal averaging must be ensured, due to random distribution. Few studies of canopy radar response are reported in literature separately for ground-based systems, airborne, and spaceborne scatterometers [42]. Typical behavior of most land targets is:

$$\frac{\sigma^o(\theta)}{\cos(\theta)} = const. \tag{4.11}$$

This is expected for a collection of scatterers with varying sizes and orientations [42].

Amazon rainforest is traditionally used as a scatterometer calibration target. It was used as a part of both SASS [7, 30] and ERS-1 [19, 30] missions. It will be used in the dissertation, but the entire target will be divided into location elements as explained in previous section. This original approach eases large area uniformity requirement, since smaller surfaces are more likely to have uniform radar response. SKYLAB passes over Amazon in 1973/74 recognized regional stability that was later confirmed by SASS and ERS-1. Both spatial and polarization independence, together with temporal stability was noticed for an area larger than 3 million km^2. Amazon basin was therefore used during SASS and ERS-1 missions. Some diurnal variations are observed in these studies. Morning passes exhibited up to a dB higher σ^o magnitude. This has been attributed to morning dew on forest leaves [26], or to average orientation of leaves in the canopy at different Sun angles [30]. Although, the reason for this diurnal variation is not completely understood, it is plausible that geophysical properties can cause day/night differences in σ^o response. These differences suggest separating data according to the spacecraft direction into ascending (nighttime) and descending (daytime) passes. Ascending spacecraft direction corresponds to the north-bound movement of the subsatellite point and descending corresponds to the south-bound. Correction terms $c_b(\theta)$ (4.10) should be the same for both directions, because beam biases are instrument related and spacecraft can not differentiate between two directions. Beam corrections, calculated from ascending data alone, are expected to be independently confirmed by the corrections calculated from measurements taken while spacecraft was descending.

After separating measurements into ascending/descending subsets, masks are employed to extract calibration data. Geographical boundaries of isotropic response areas are determined using the Scatterometer Image Reconstruction (SIR) algorithm [14, 29]. SIR is a scatterometer resolution enhancement algorithm developed at Brigham Young University by Dr. David Long. It is based on spatial overlap of measurements taken at nominal resolution during multiple passes over the region. Thus, it relies on temporal stability during the overlap period. The available amount of the resolution enhancement is determined by the number of overlapped measurements. The SIR algorithm models σ^o [dB] over land as a linear function of the measurement incidence angle [6, 26]:

$$\sigma^0(\theta) = A + B\vartheta \ , \tag{4.12}$$

where $\vartheta = \theta - 40^o$ is taken as before for numerical stability, and A and B are constants characterizing the observed target. The ranges of values of these constants are:

$$-0.15 \leq A \leq 0.07 \text{ dB} ,$$
$$-4.4 \leq B \leq 0.6 \text{ dB / deg} . \tag{4.13}$$

The values of A and B are determined by the surface type, vegetation cover, moisture content, etc. [42]. Nominal coarse σ^o scatterometer resolution is enhanced into finer grid. Multiple passes are collected to estimate A and B for elements of this finer grid. Noise in A and B images is inversely proportional to the size of the refined resolution cells (smaller resolution cells $\Rightarrow$ increase in the noise level of A and B estimates). Using iterative approach, A and B land images are generated for resolution as good as 5 km [14, 29]. Modifications in scatterometer design are proposed to achieve even further resolution enhancement in the future [29]. The modifications would include different beam sequence and downlink of individual periodograms. Instead of 25 transmit/receive + 4 noise-only cycles, as explained in section 3.4, sequence that would switch to a next beam after a single measurement is proposed. With moderate increase in the downlink bandwidth, necessary for implemented modifications, this would achieve ultimate resolution of 1-2 km.

Images of A and B coefficients are generated using described SIR algorithm. Increased resolution pixels (5 X 5 km) are defined with their SIR σ^o estimates. Pixels with uniform A and B response are identified and extracted into spatial masks. Criteria for pixel selection is defined by $\overline{\sigma}_A^o(\theta) \pm 0.5$ dB interval, where $\overline{\sigma}_A^o(\theta)$ is the mean value of the entire Amazon region at a given incidence angle. Masks are binary in the sense that a pixel is either accepted (if within the interval) or rejected. NSCAT σ^o cells (≈ 25 X 10 km) cover up to ten SIR pixels (5 X 5 km). To ensure consistency and decrease noise, a conservative approach is adopted, where only NSCAT σ^o cells that contain pixels that are all within the mask are used in the algorithm. Measurements from these cells propagate through the calculation part of the algorithm (Figure 16). This conservative approach increases time necessary to collect sufficient data set for response modeling, but decreases noise in the modeling. NSCAT σ^o cell selection process is illustrated on Figure 17. SIR pixels satisfying:

$$\overline{\sigma}_A^o(\theta) - 0.5 \leq A + B\vartheta \leq \overline{\sigma}_A^o(\theta) + 0.5 \tag{4.14}$$

are given as "+" (accepted) and those pixels outside of the interval (4.14) are denoted as "o" (rejected). NSCAT σ^o cells, containing multiple SIR pixels, are illustrated. The left cell is accepted, since it contains all SIR pixels classified as Amazon ("+"). Cell on the right is rejected since it contains several high-resolution pixels that were classified as non-Amazon ("o"). One of the challenges in generating the algorithm, was correct description of SIR/NSCAT geometry and accurate determination of integrated NSCAT σ^o cell limits.

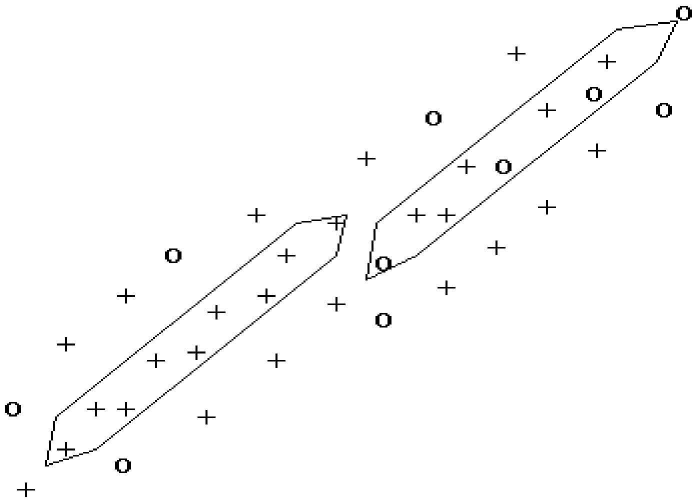

Figure 17: NSCAT σ° cell selection

Using SIR high-resolution binary masks, NSCAT cells over Amazon are selected. The resulting geographical region is shown on Figure 18. This area covers more than 2 million km^2. Amazon River is identifiable by following excluded strip from the Macapa Bay deep into South American continent. Excluded cells, containing significant portion of the river, are identified by 1-3 dB lower σ^0 than neighboring canopy. Other isolated excluded spots on Figure 18 are areas such as Amazon River tributaries and occasional breaks in the canopy. The climate is hot and humid with minimal seasonal effects. Some seasonal effects are observed in a form of fluctuations in the amount of rainfall. Figure 18 also clearly illustrated applicability of high-resolution scatterometry for rainforest monitoring. Polarization independence, noticed during SIR Amazon mask generation, is attributed to random orientation of the scatterers in the uniformly vegetated rainforest. This allows merging measurements from two horizontally polarized NSCAT beams together with six vertically polarized.

Previous scatterometer calibration campaigns, utilizing Amazon basin, used the entire regional data set as a unit. The approach relied on azimuth-isotropic $\sigma^0(\theta)$ response throughout the masked area. In the novel method employed here, this assumption is relaxed by dividing the mask into M smaller location elements, as described in the previous section. The idea behind the introduction of the location elements is that such smaller areas would ensure that all NSCAT σ^0 cells within a location element have the same $\sigma^0(\theta)$. Corrections $c_{b,l}(\theta)$ (4.10) are calculated for each location and averaged to estimate final correction $c_b(\theta)$ (4.11). The idea of mask subdivision is implemented in the

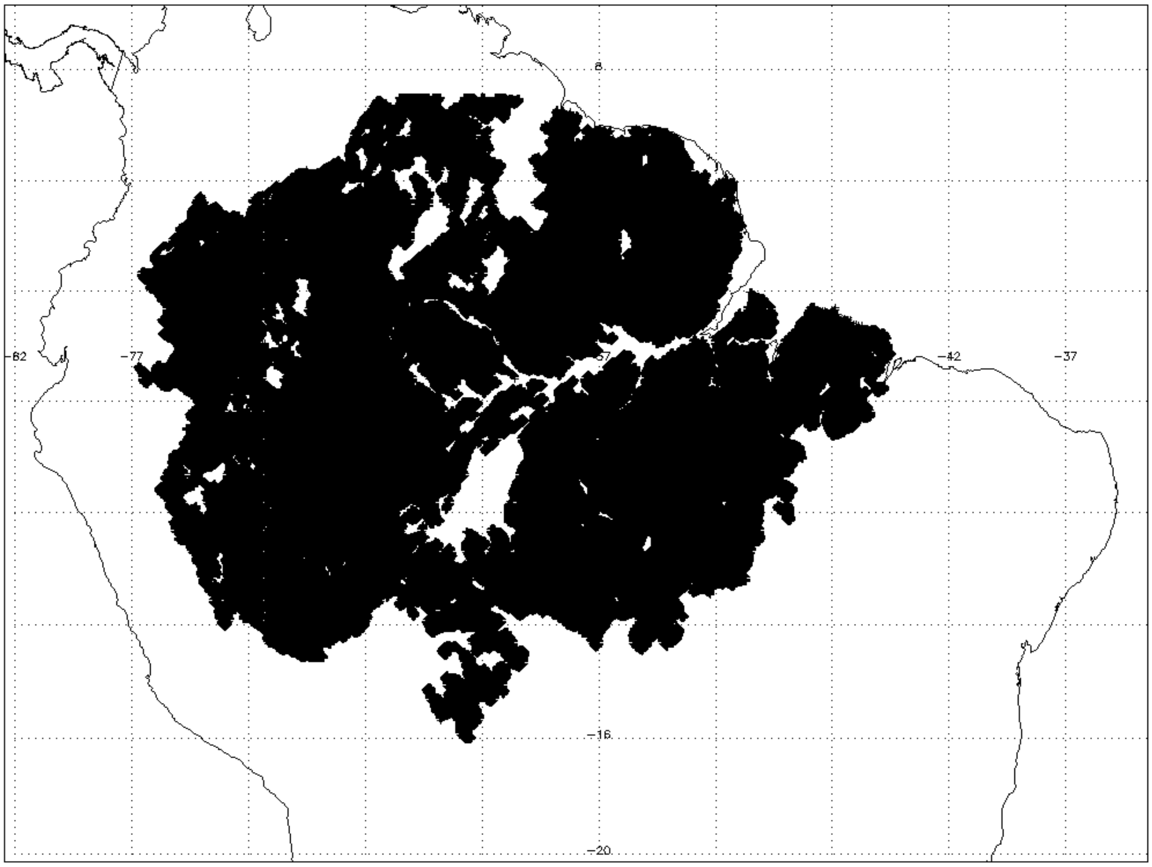

Figure 18: Amazon mask used for calibration data selection

algorithm (Figure 16) by assigning coordinates of the first calibration data point to be the center of the first location cell. Subsequent NSCAT data points are checked according to the distance between assigned location element centers and σ^o cell center of the data point. If this distance is less than arbitrary set distance *D*, data point is included into current location element. Otherwise, data point defines the center of the new location element. Following such grouping mechanism, location elements are formed within the Amazon rainforest SIR mask (Figure 19). Different location elements are distinguished by varying shade of gray on the figure. Distance *D* is arbitrarily set to 500 km, resulting in *M*=29 locations. This number has been chosen among several trials as a compromise between target homogeneity (smaller target desired) and convergence time (larger target desired).

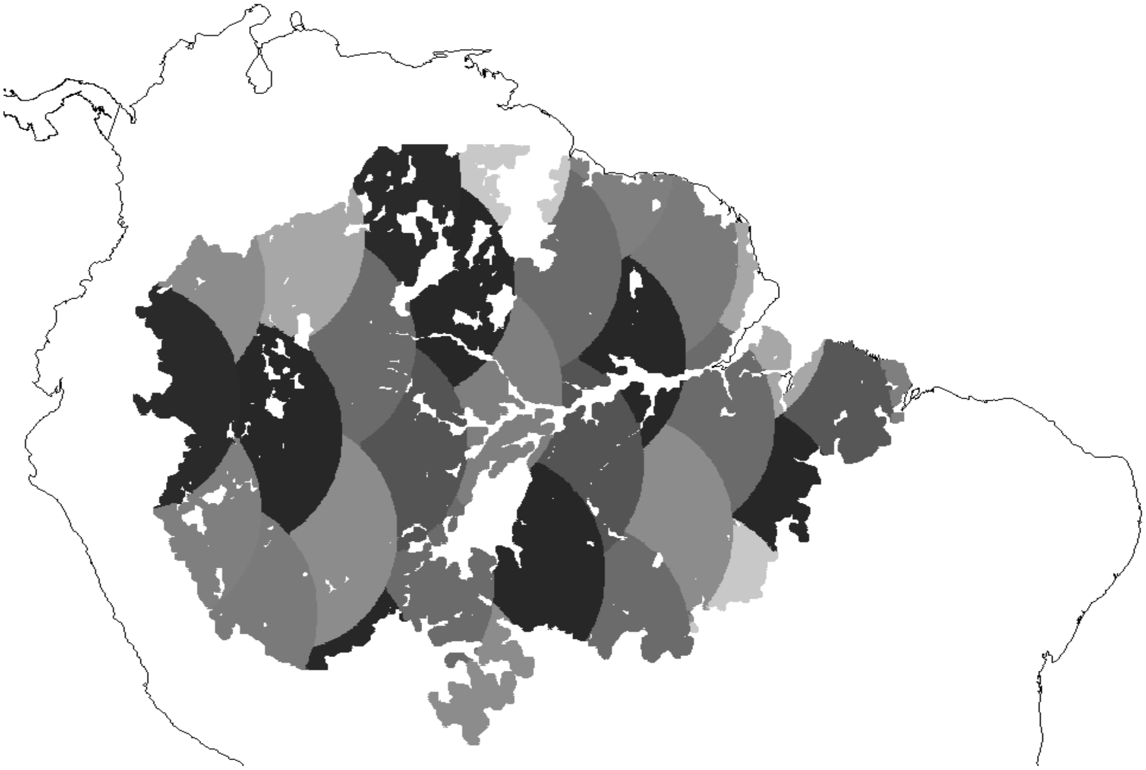

Figure 19: Location elements within Amazon selection mask

Besides traditionally used Amazon rainforest, several other uniform land targets are considered for scatterometer calibration. These include Congo rainforest and Greenland [26]. NSCAT calibration/validation activities were undertaken shortly after ADEOS launch in September 1996 at JPL. During these activities, another large area with uniform σ^o response is detected in central Russia. Following the high-resolution geographical masking procedure, mask of the area is created, as shown on Figure 20. The area stretches ≈90° in longitude and ≈18° in latitude. It covers mostly moderately vegetated plains bounded by Wherkoyanskiy Kherebet mountain range. The area exhibits

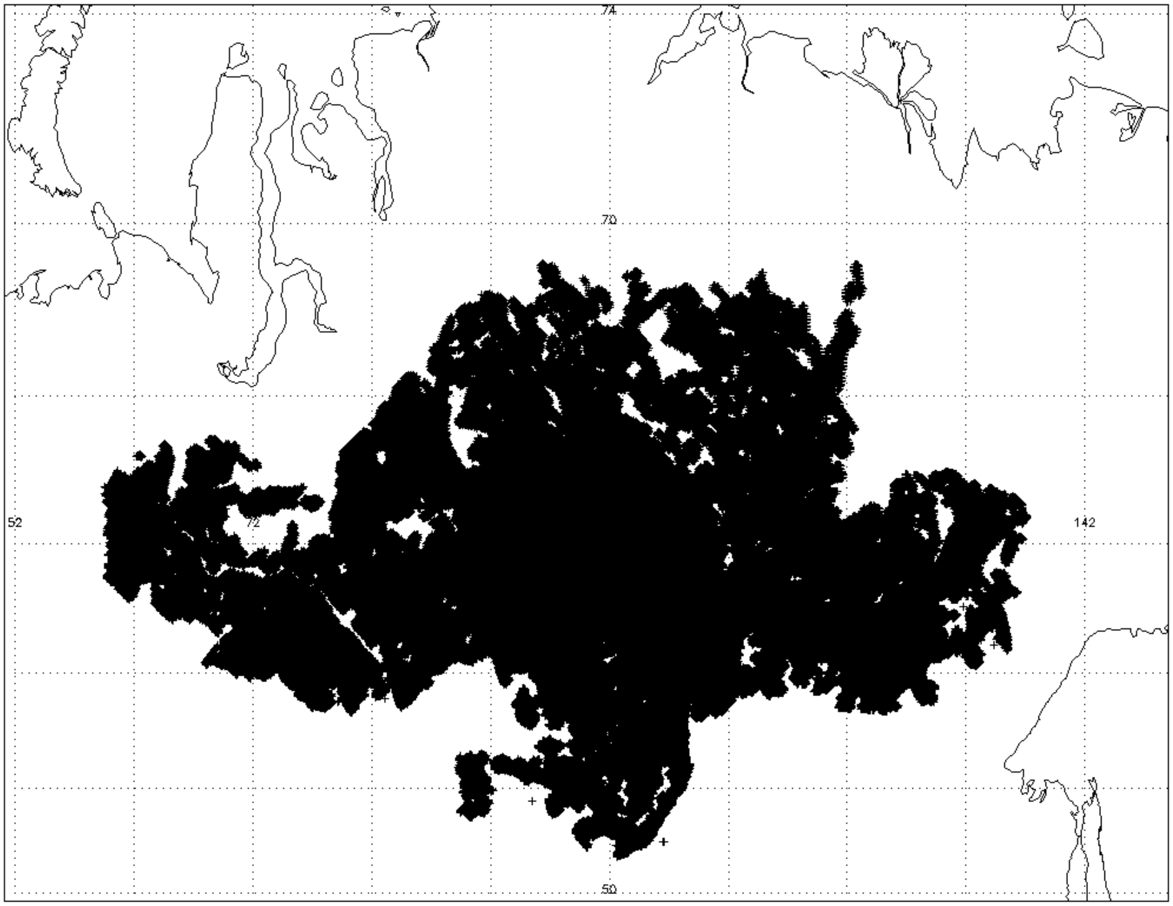

Figure 20: Russian mask used for calibration data selection

azimuth and polarization independence, but standard deviation of σ^o measurements is higher than for Amazon data. Thus, more weight should be given to results based on Amazon data and Russian data will be used to independently confirm calibration derived from Amazon. Further limiting the reliability of Russian data, are severe seasonal changes in the region. Therefore, the time interval for data selection should be kept shorter than for Amazon, to minimize climate-related effects.

4.5 Calibration results

Before presenting results obtained by the outlined method, seasonal effects of the Amazon radar response are investigated. Figure 21 shows mean (average of all beams and ascending/descending average) response $\bar{\sigma}^o(\theta)$ of the Amazon basin in four different months during the first half of the mission. The seasonal effects are manifested as shift in the mean response as mission progressed. Amazon σ^o was ≈ 0.5 dB higher in January 97 than in September. This is attributed to geophysical (rainfall) seasonal changes, since no shift in the system parameters (gain, etc) is noticed.

Using the method described in the preceding section, corrections to measured σ^o values are calculated according to (4.10). Calculated $c_b(\theta)$ are plotted in linear-log space on Figures 22-25. Plots are given for September 96 (Figure 22), November 96 (Figure 23), December 96 (Figure 24), and January 97 (Figure 25). Calibration data sets for each plot are collected during a three-week period in a particular month. This is a compromise between amount of data (reliable modeling) and the algorithm convergence time. Third order polynomial is accepted after showing satisfactory convergence. The figures confirm

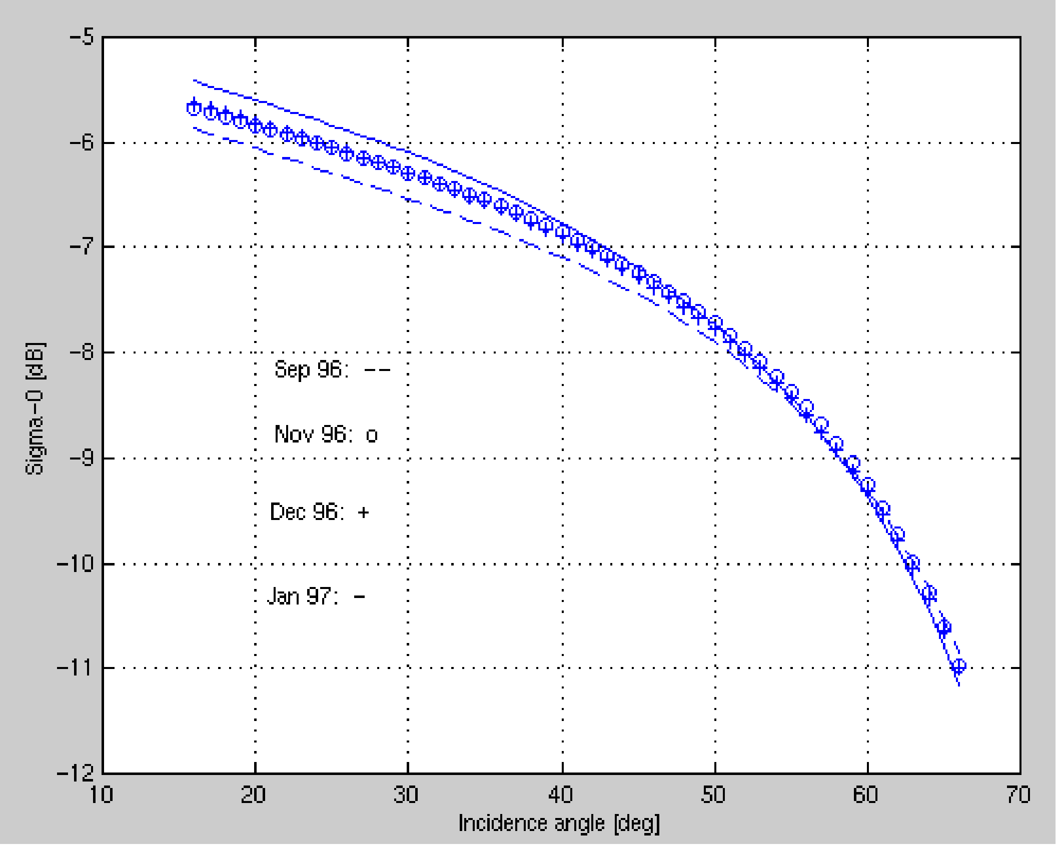

Figure 21: Seasonal effects in Amazon $\overline{\sigma}^{0}(\theta)$ response

stability of the NSCAT measurements, as $c_b(\theta)$ patterns are repeatable throughout the mission duration. Figures are given in two parts, one for the each side of the spacecraft, with upper sub-figure showing results for the right-on-ascend side of the spacecraft (beams 1-4, Figure 11) and the lower sub-figure contains results for the left-on-ascend side (beams 5-8). Among individual beams, beam 3 (horizontally polarized middle beam on the right side) requires the highest correction, while beams 4 and 7 are closest to the average of all beams. The magnitude of calculated corrections justifies on-orbit calibration, because just a few tenths of a dB will significantly degrade the wind retrieval accuracy.

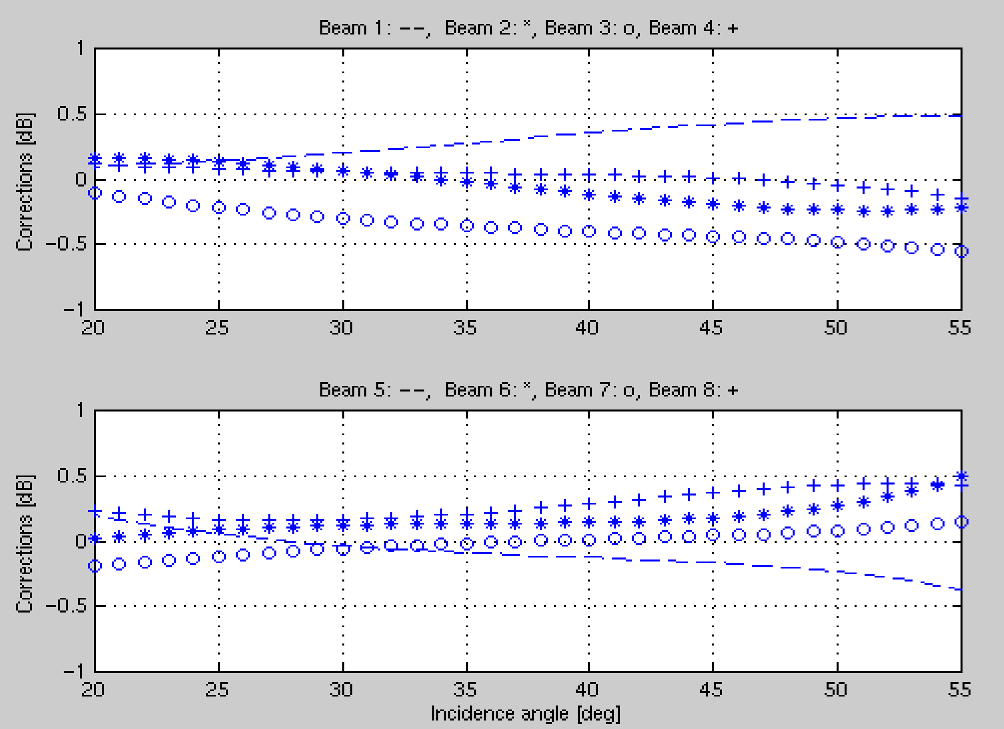

Figure 22: Beam corrections $c_b(\theta)$ calculated based on September 96 data over Amazon

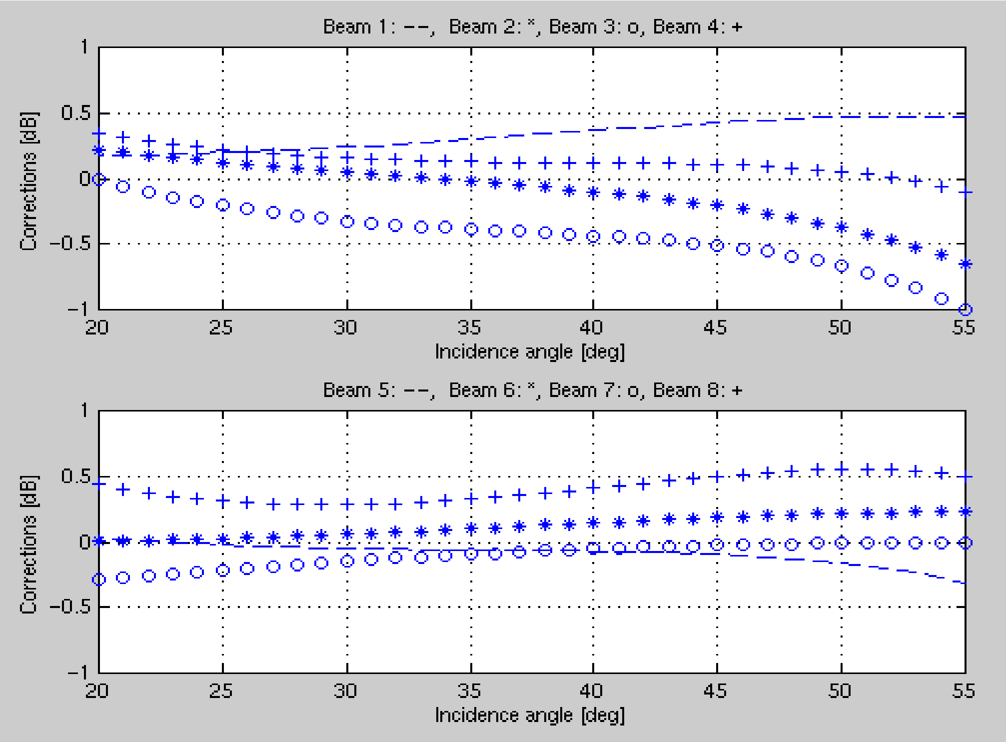

Figure 23: Beam corrections $c_b(\theta)$ calculated based on November 96 data over Amazon

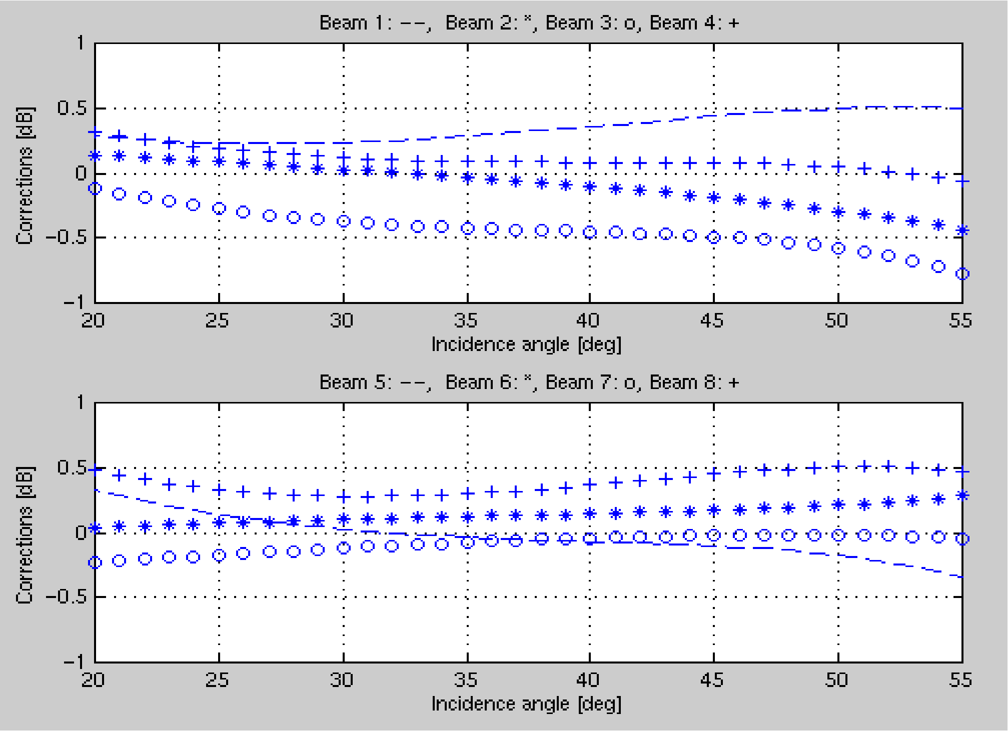

Figure 24: Beam corrections $c_b(\theta)$ calculated based on December 96 data over Amazon

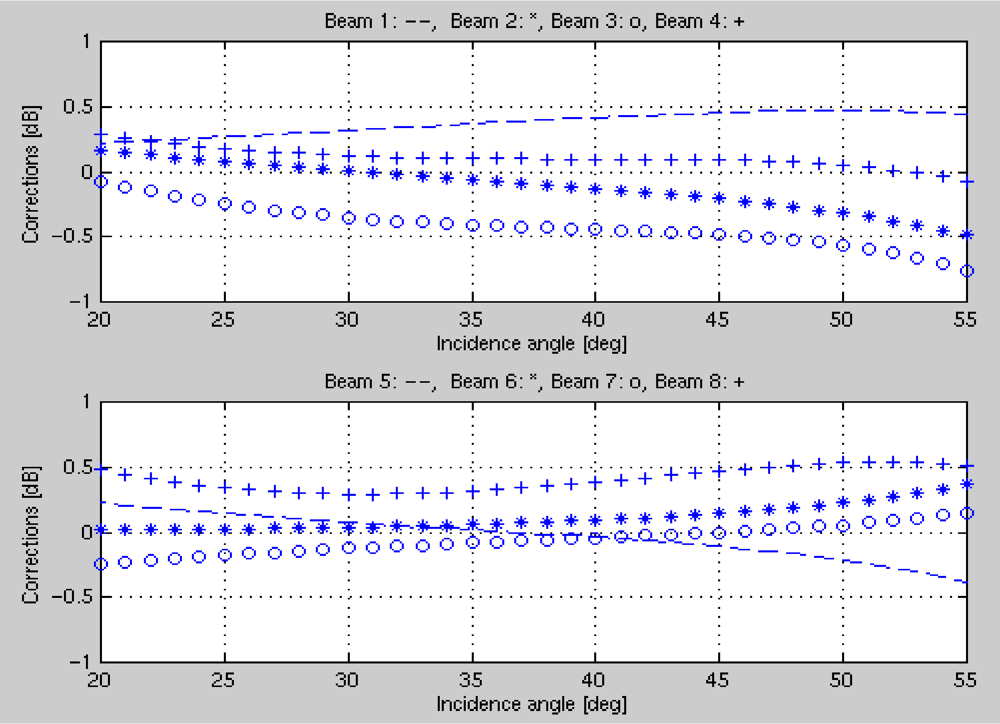

Figure 25: Beam corrections $c_b(\theta)$ calculated based on January 97 data over Amazon

Figure 26 shows beam balance corrections $c_b(\theta)$ calculated based on the entire NSCAT mission data set. All NSCAT measurements taken within boundaries of the Amazon mask (Figure 18) contributed to $c_b(\theta)$ estimation plotted on Figure 26. This correction set is therefore calibration with all seasonal effects (within NSCAT lifetime) averaged out. This is suggested set of $c_b(\theta)$ to be applied toward balancing the entire NSCAT σ^o data set.

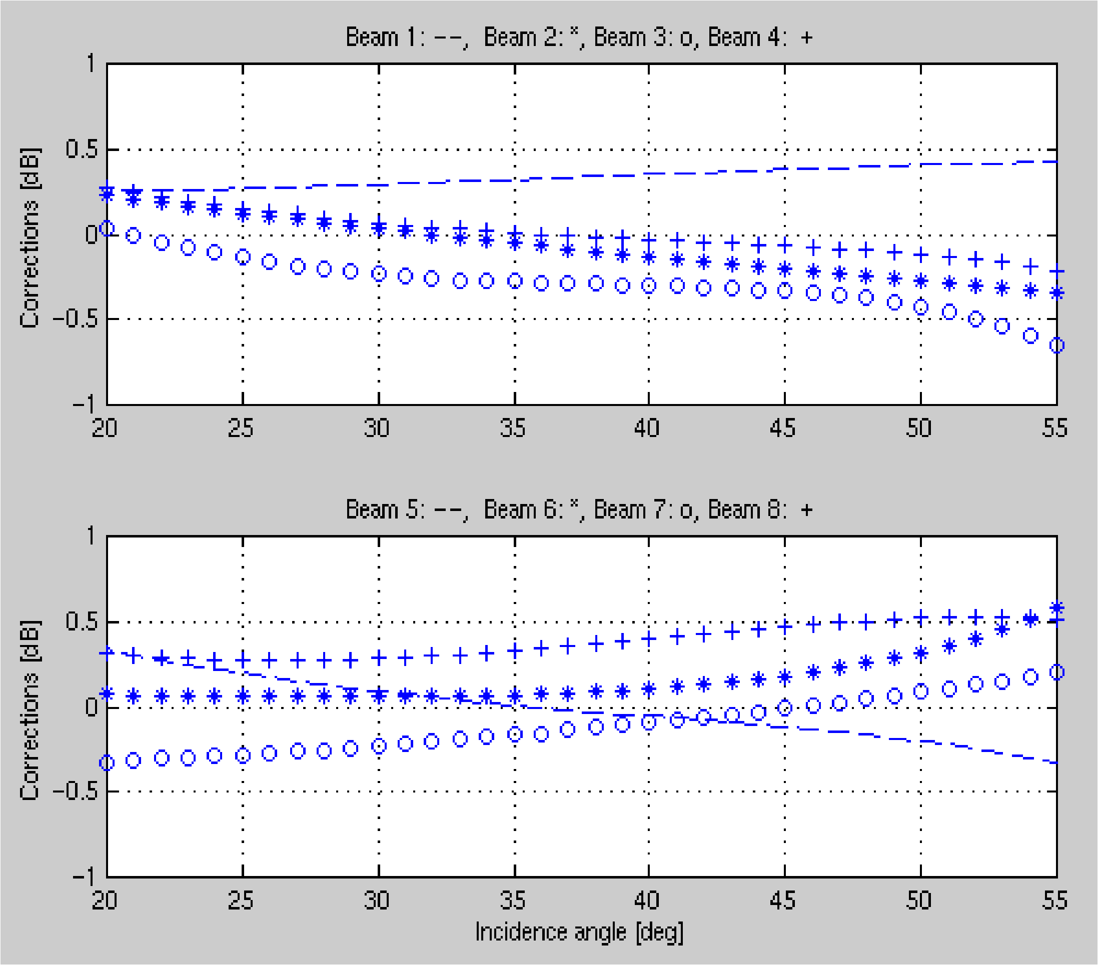

Figure 26: Beam corrections $c_b(\theta)$ calculated based on the entire NSCAT data set (August 96-June 97) taken over Amazon

Results graphed on Figure 26 are tabulated in Appendix A. Tabulated entries are calculated by evaluating the expression for $c_b(\theta)$ (4.10) at incidence angles θ=16+2k, k=0,1,..25 and beams b=1,2,..8. This produces 8 (beams) X 26 (incidences 16-66) matrix, which is a standard JPL format for reporting beam-bias removal results.

Amazon rainforest has been traditionally used land target for scatterometer beam calibration. Additional homogenous area was noticed in central Russia (Figure 20) and is used for independent confirmation of corrections based on Amazon. The seasonal climate effects present at higher latitudes limit usage of Russian data. Vegetation cover also dramatically changes and is not uniform and homogenous as in tropical rainforests. These effects are observed on Figure 27, which shows the mean NSCAT σ^o response over central Russia for the same 4 different periods as shown for Amazon on Figure 21 (September, November, and December 96, and January 97). Scatter in $\overline{\sigma}^o(\theta)$ is larger than for Amazon (Figure 21). Because of this seasonal variation in radar response, results based on Russian data are considered only during periods of snow-free conditions. Snow-covered ground exhibits some azimuthal effects, which disqualifies such areas as calibration targets.

Figure 28 shows $c_b(\theta)$ calculated based on data collected over masked region in central Russia (Figure 20). Data are collected in September 96. A three-week window and third order polynomial are used for modeling, as was done for Amazon data. Results inferred from the Russian data (Figure 28) are in good agreement with the results from Amazon rainforest (Figures 22-26). The shapes of individual $c_b(\theta)$ curves are similar for both calibration targets, with insignificant difference in magnitudes due to measurement

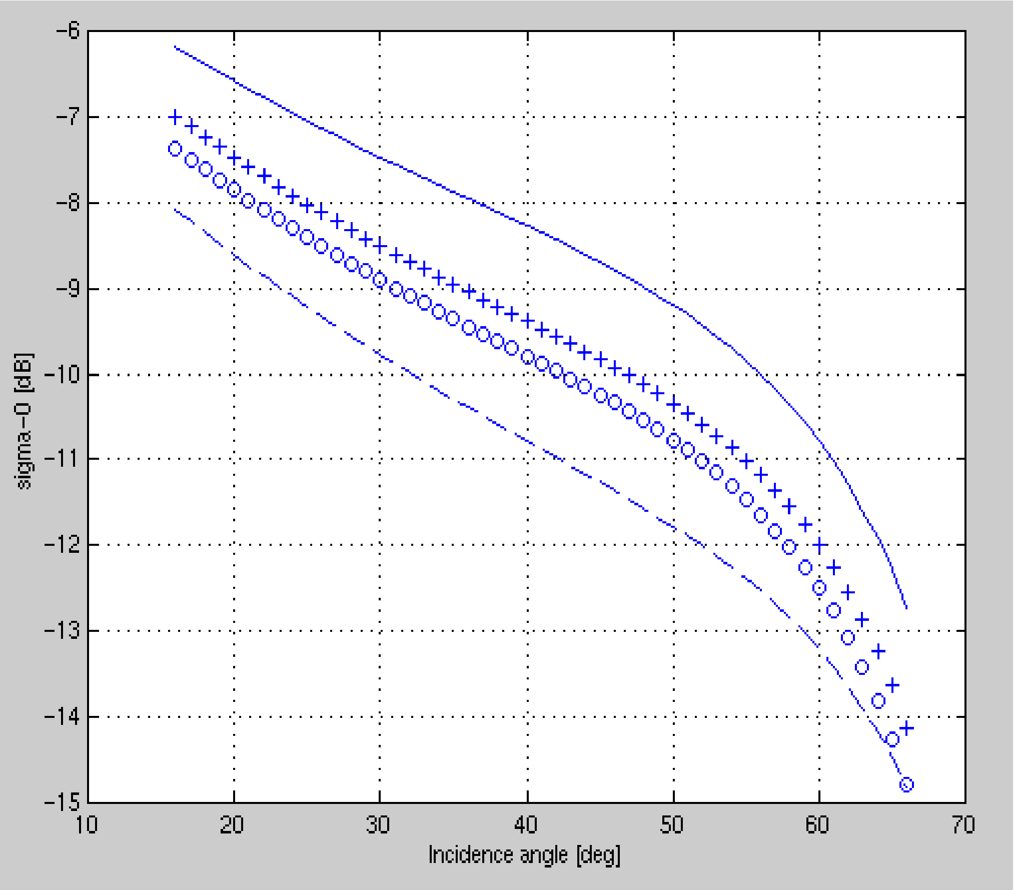

Figure 27: Seasonal effects in Russian $\overline{\sigma}^{0}(\theta)$ response (Sept. 96: '- -'; Nov. 96 : 'o'; Dec. 96: 'x' and Jan. 97: solid)

noise. Calculating $c_b(\theta)$ from σ^o measurements within central Russian mask thus confirms $c_b(\theta)$ beam balance numbers calculated based on more reliable Amazon rainforest data. It also demonstrates the stability of the NSCAT instrument. However numbers tabulated in $c_b(\theta)$ table in Appendix A are derived from Amazon data alone. This is done because of the much higher homogeneity and temporal stability of the Amazon rainforest. The value of the Russian experiment was to independently confirm Amazon results from the qualitative standpoint.

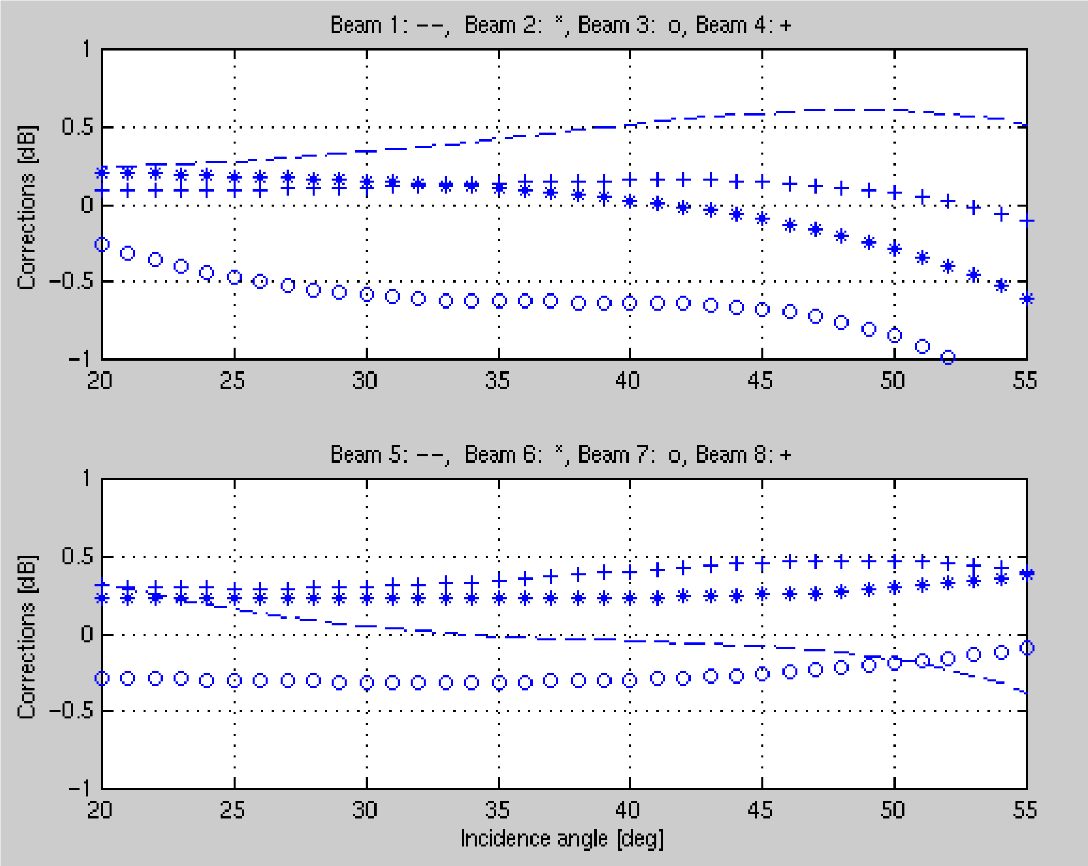

Figure 28: Beam corrections $c_b(\theta)$ calculated based on September 96 data over central Russia

Because of the wind retrieval accuracy requirements, σ^o must be estimated within few tenths of a dB. This calls for post-launch, on-orbit campaigns in addition to pre-launch laboratory tests. As a part of the NSCAT mission, post-launch calibration and validation efforts included several independent methods. Besides distributed land target method detailed in the dissertation, inter-beam balance was attempted using σ^o measurements over open ocean, over ice and the calibration ground station in White Sands, NM. All methods converged to beam balance numbers depicted in Figures 22-26 with small variations among the methods. Because the NSCAT is primarily a wind-observing instrument over the ocean, the method using σ^0 measurements over open ocean was accepted for final NSCAT σ^0 reprocessing. This method uses European Center for Medium Range Weather Forecasting (ECMWF) and US National Weather Service numerical-model wind fields. NSCAT-measured σ^0's are tuned to these modeled fields as a surface truth. ECMWF products are high-resolution wind fields generated globally every six hours. An example of the ECMWF wind field over western pacific is illustrated on Figure 29. This field was modeled according to parameters recorded at 00 universal

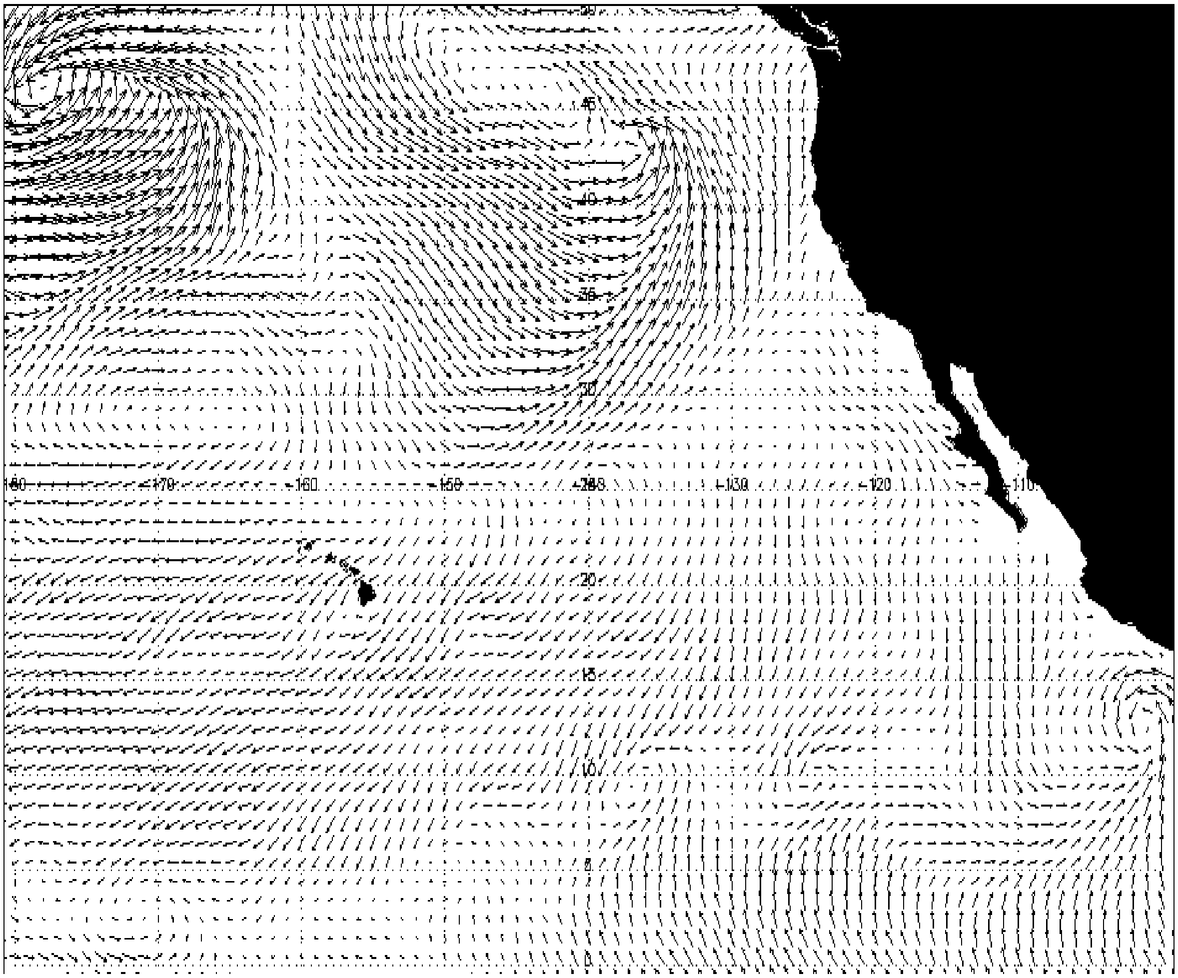

Figure 29: ECMWF wind field model over western Pacific, 10/01/1997, 00 UTC

time on October 1, 97. Beam balancing $c_b(\theta)$ is calculated forcing NSCAT-retrieved winds to such models. σ^o measurements are corrected to produce winds (through model function inversion) that agree well with the ECMWF model. This beam balance numbers are used in final reprocessing of the entire NSCAT σ^o data set, before it's release to the scientific community.

The comparison between this JPL-accepted $c_b(\theta)$ and $c_b(\theta)$ calculated using the homogenous land target method, is given on Figures 30-34. Figure 30 shows $c_b(\theta)$-$c_4(\theta)$ for six vertically polarized beams. Beam 4 (aft beam on right-on-ascend side, Figure 11) is chosen as the reference because two methods use different absolute references and can be compared only when referenced to $c_b(\theta)$ for a fixed beam b. Beam 4 responds the closest to the mean of all beams, but was chosen arbitrarily as a reference and any other beam, regardless of the deviation from the mean, could have been chosen. JPL-accepted $c_b(\theta)$-$c_4(\theta)$ curves are given as dashed lines. They are in very good agreement with the solid line depicting $c_b(\theta)$-$c_4(\theta)$ normalized correction calculated from the Amazon rainforest data. Figure 30 shows comparison for the ascending revolutions alone. Because of the difference in ascending (sub-satellite point moving northward) and descending (southward) based $c_b(\theta)$, the beam balances are calculated separately for the two data sets. This discrepancy will be addressed in next chapter. The descending counterpart of Figure 30 is Figure 31 showing again good agreement between ocean inter-beam calibration method (dashed line) and land target method.

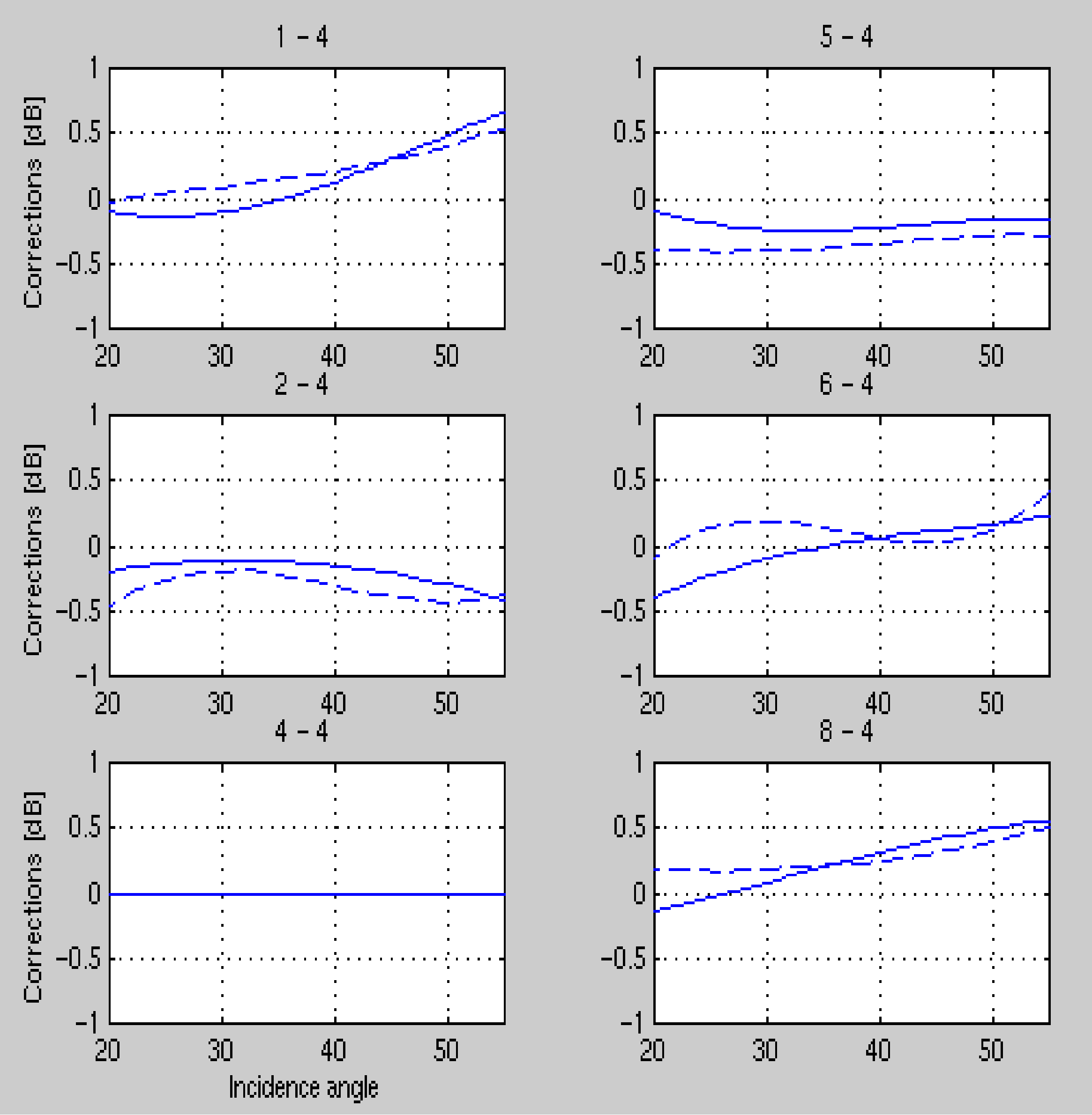

Figure 30: Comparison between JPL-accepted $c_b(\theta)$-$c_4(\theta)$ (dashed line) and $c_b(\theta)$-$c_4(\theta)$ calculated by the homogenous land target method from the Amazon data (solid line). Vertically-polarized beams, ascending data alone

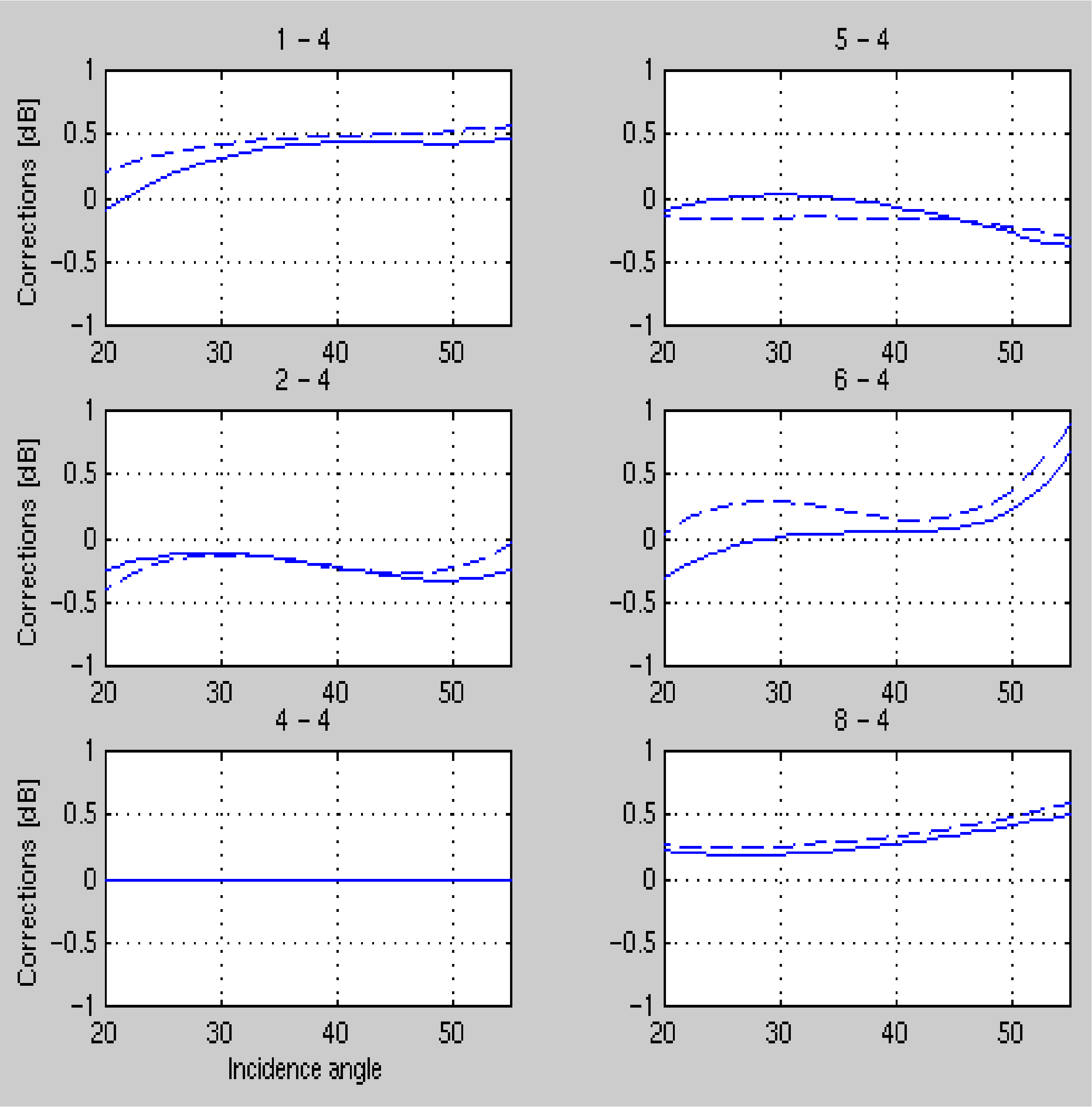

Figure 31: Comparison between JPL-accepted $c_b(\theta)$-$c_4(\theta)$ (dashed line) and $c_b(\theta)$-$c_4(\theta)$ calculated by the homogenous land target method from the Amazon data (solid line). Vertically-polarized beams, descending data alone

The agreement is worse for horizontally polarized beams 3 and 7, as shown on Figure 32. This is due to a different treatment of the horizontal polarization by these two methods. While ocean method uses model function to analyze horizontal polarization, our method relies on the assumption of polarization-independence of the calibration target radar response. The resolution of this question is not in a scope of the dissertation, but would be important for the full acceptance of the homogenous land target method in the future. But even this disagreement does not exceed 0.3 dB for the worst case of ascending beam 7. Other beams agree well for both methods.

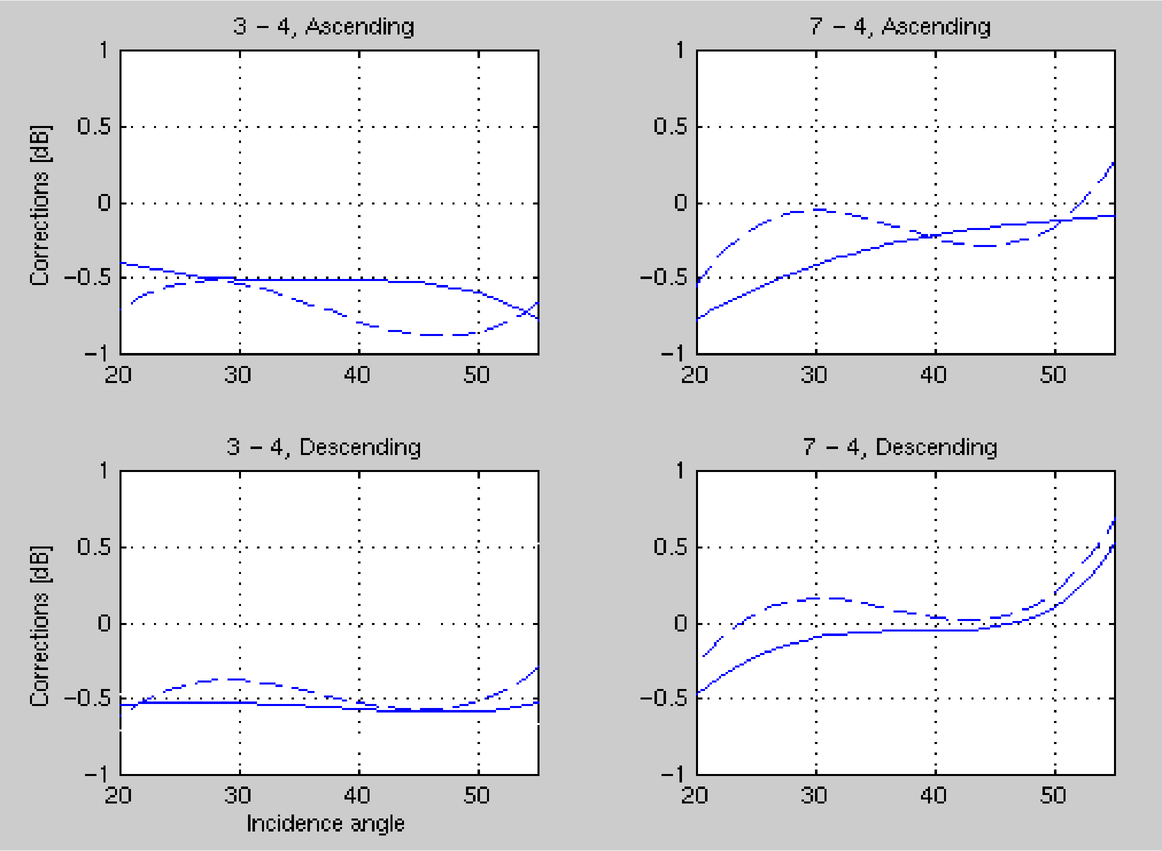

Figure 32: Comparison between JPL-accepted $c_b(\theta)$-$c_4(\theta)$ (dashed line) and $c_b(\theta)$-$c_4(\theta)$ calculated by the homogenous land target method from the Amazon data (solid line). Horizontally-polarized beams

Similar comparison holds for Russian-based data as well. Vertically-polarized beams have close $c_b(\theta)$-$c_4(\theta)$ normalized corrections for both JPL-accepted and land target method (Figure 33).

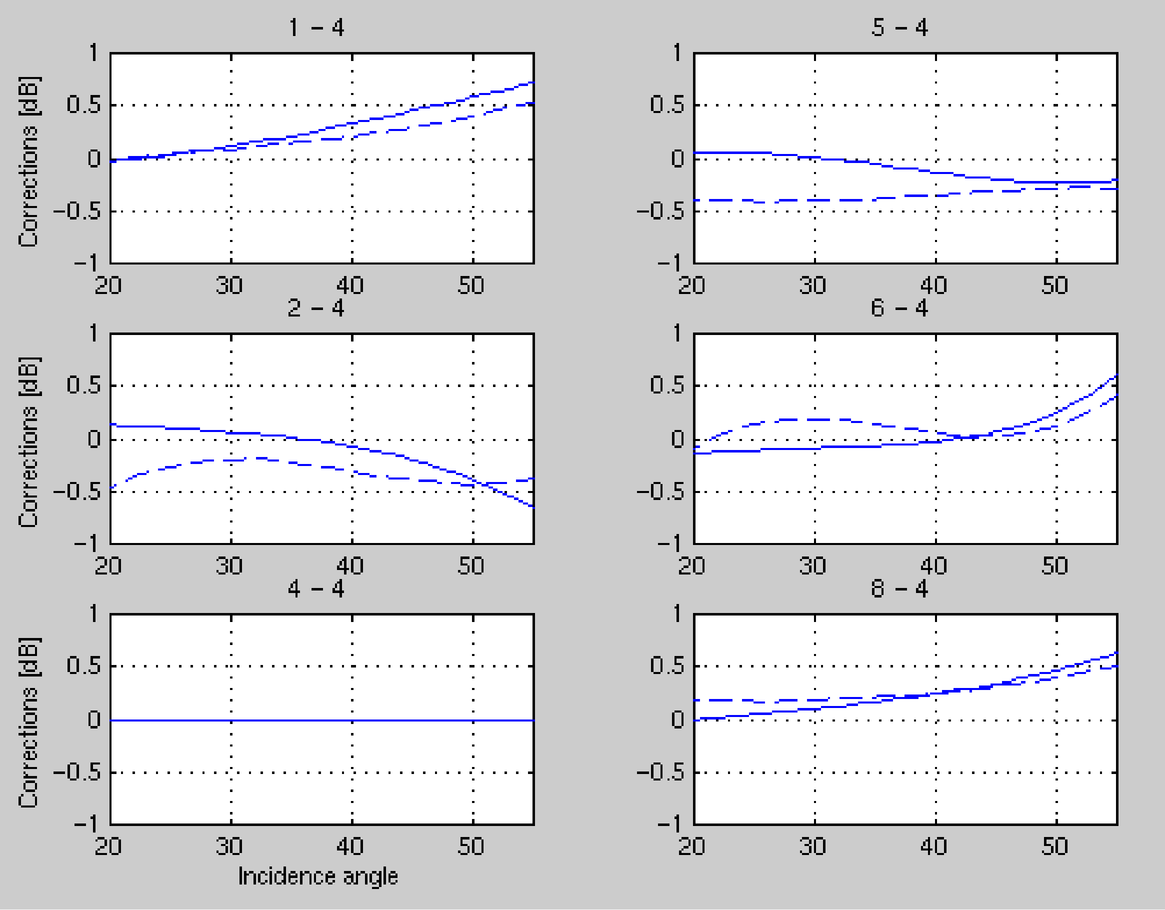

Figure 33: Comparison between JPL-accepted $c_b(\theta)$-$c_4(\theta)$ (dashed line) and $c_b(\theta)$-$c_4(\theta)$ calculated by the homogenous land target method from the central Russian data (solid line). Vertically-polarized beams, ascending data alone

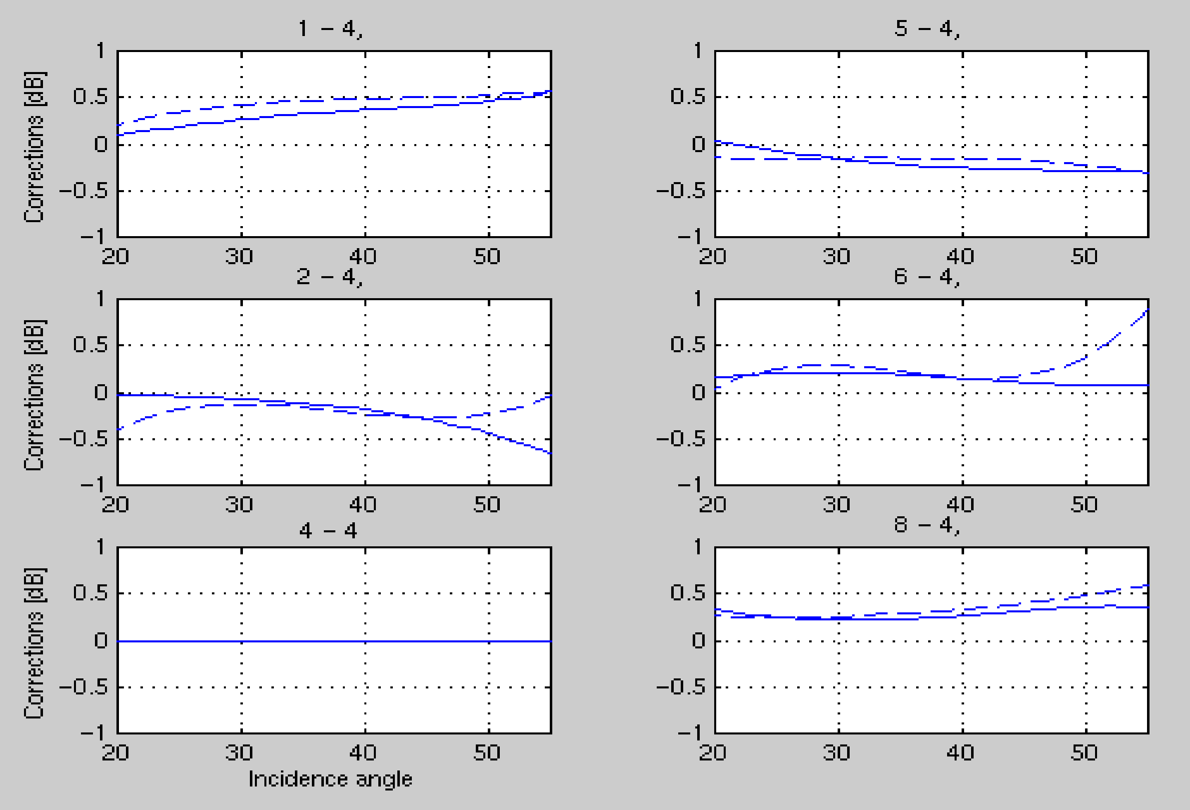

Figure 34: Comparison between JPL-accepted $c_b(\theta)$-$c_4(\theta)$ (dashed line) and $c_b(\theta)$-$c_4(\theta)$ calculated by the homogenous land target method from the central Russian data (solid line). Vertically-polarized beams, descending data alone

The agreement between the methods is again worse for horizontally polarized beams 3 and 7 (Figure 35). The disagreement is higher than for the Amazon data counterpart (Figure 32). This means that the area in central Russia have larger polarization effects in the radar response than the Amazon tropical rainforest.

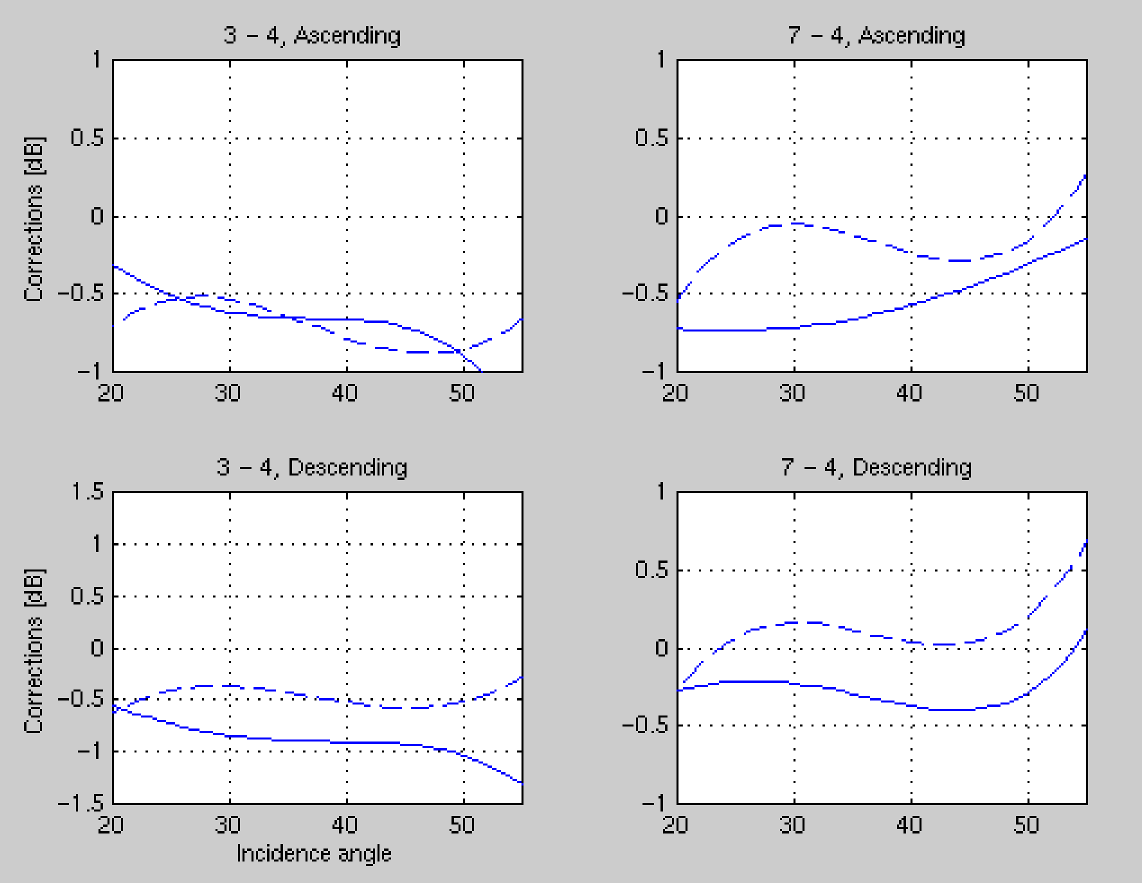

Figure 35: Comparison between JPL-accepted $c_b(\theta)$-$c_4(\theta)$ (dashed line) and $c_b(\theta)$-$c_4(\theta)$ calculated by the homogenous land target method from the central Russian data (solid line). Horizontally-polarized beams

Despite slight disagreements in the results for horizontally polarized beams 3 and 7, the overall agreement between JPL-accepted ocean method and the method proposed by this dissertation is remarkably good. It serves as a confirmation of the beam balancing numbers $c_b(\theta)$ produced by both methods. It is also a confirmation of the validity of the simple method relying on the distributed land targets. In addition to simplicity, the proposed method converges faster than the open-ocean method and does not require additional data or models (such as ECMWF wind field models). Land target method is also independent of the uncertainties in the model function, since it uses only raw σ^o measurements. However, it relies heavily on the assumption of target homogeneity and time stability during the data collection period. This is the reason for careful data selection and filtering described earlier in this chapter. The most important operationally applicable result is the table in Appendix A summarizing $c_b(\theta)$ for all beams (b=1-8) and incidence angles θ=16-66^o with the step of 2^o.

5. ADEOS ATTITUDE DETERMINATION

5.1 Introduction

Diurnal effects in radar σ^o response have been noticed in the past. They were attributed to varying geophysical properties of the target during a 24-hour period. This necessitates separating σ^o measurements into time-of-day bins to ensure homogeneity and remove diurnal geophysical variations. The only remaining effects in such bins are system biases among antenna beams. Since beam balancing is aimed at removing these biases, all such bins should converge to the same set of beam balance corrections $c_b(\theta)$. In other words, relative biases among beams should be the same at any time of day. However, small but stable and repeatable differences are observed in $c_b(\theta)$ calculated from ascending (night) and descending (day) data. Since antenna beams can not differentiate directions of the spacecraft and change gains accordingly, this emerged as a puzzling anomaly during NSCAT calibration and validation activities at the JPL.

An attempt is made in this chapter to explain ascending/descending discrepancy by imperfect knowledge of the spacecraft attitude. The problem is introduced in next section. Stable difference in $c_b(\theta)$, calculated separately based on ascending and descending data is shown for several periods. Attitude set is defined and mathematical model formulated using an objective function. The objective function is parametrically calculated for multiple attitude sets. The set resulting in the lowest difference between ascending and descending based $c_b(\theta)$ (minimum objective function) is suggested as the proper attitude.

It is shown that applying suggested attitude adjustment, decreases standard deviation of σ^o measurements.

5.2 Diurnal effects in beam balancing

Diurnal effects have been previously noticed in the radar response of natural targets [7]. For Amazon σ^o data, the effect manifested as high σ^o in early morning (up to a dB higher then other times of day). This was attributed to morning dew on the forest leaves [7, 26], or different orientation of the canopy following the Sun angles [30]. As a Sun-synchronous satellite, ADEOS overflies the same spot on Earth at the same local time of day. For Equatorial regions, ascending (northward) passes occurred at ≈ 10 p.m. local time and descending (southward) at ≈ 10 a.m. Therefore, data were separated into two sets, each with different $\sigma_b^o(\theta)$ polynomial model. Beam balancing procedure described in previous chapter removes system biases among beams, and must not depend on whether ascending or descending data are used. However, $c_b(\theta)$ calculated based on ascending data, differs from the descending counterpart. This difference is illustrated on Figures 36-39. Results from different periods are shown on these figures. Figure 36 is plotted for a three week period in September 96. A three-week window was also used in November 96 (Figure 37) and January 97 (Figure 38). Figures 36-38 are plotted from data taken over Amazon mask. They show stable and repeatable difference in $c_b(\theta)$ when calculated based on ascending or descending data. Results from all beams are shown, separated to the right-on-ascend (beams 1-4) and left-on-ascend (beams 5-8) side (Figure 11). The magnitudes of differences are within few tenths of a dB:

$$\Delta c = \left| c_{b,A}(\theta) - c_{b,D}(\theta) \right| < 0.5\,\mathrm{dB}, \tag{5.1}$$

where subscript b denotes beam number as before, and additional subscript A or D denotes the spacecraft direction (ascending or descending). However it is not the magnitude of Δc, but it's stability with time that points to a consistent system bias between ascending and descending passes.

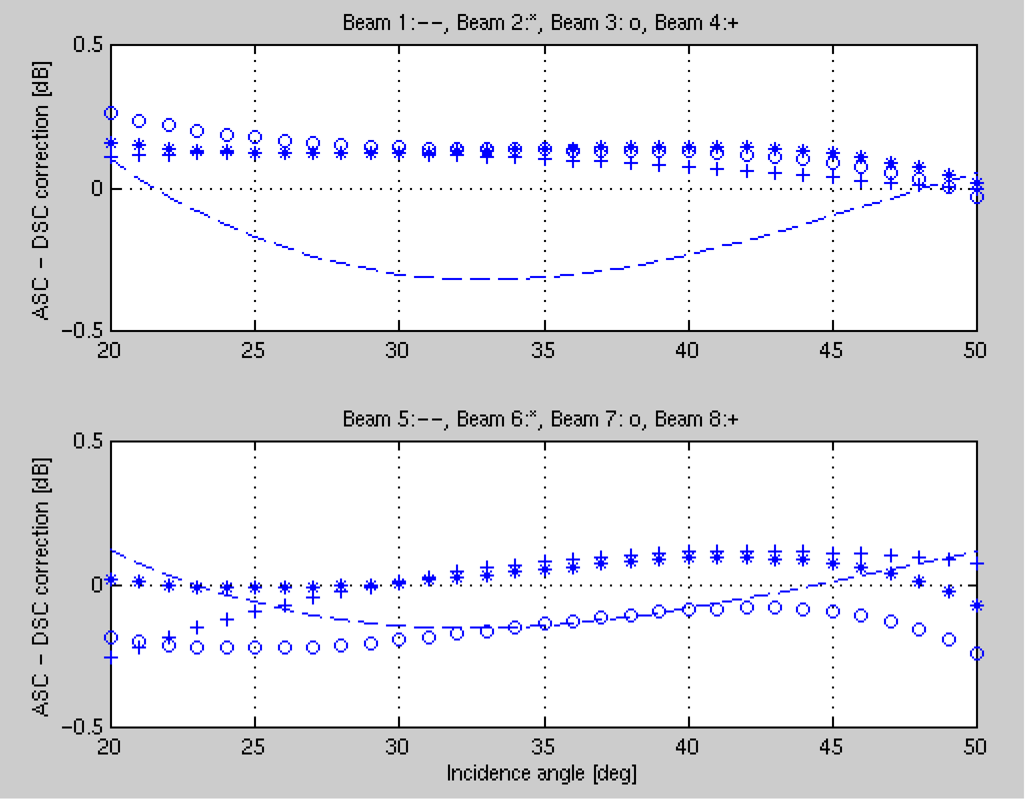

Figure 36: Difference between ascending and descending based beam balance corrections calculated from September 96 data over Amazon

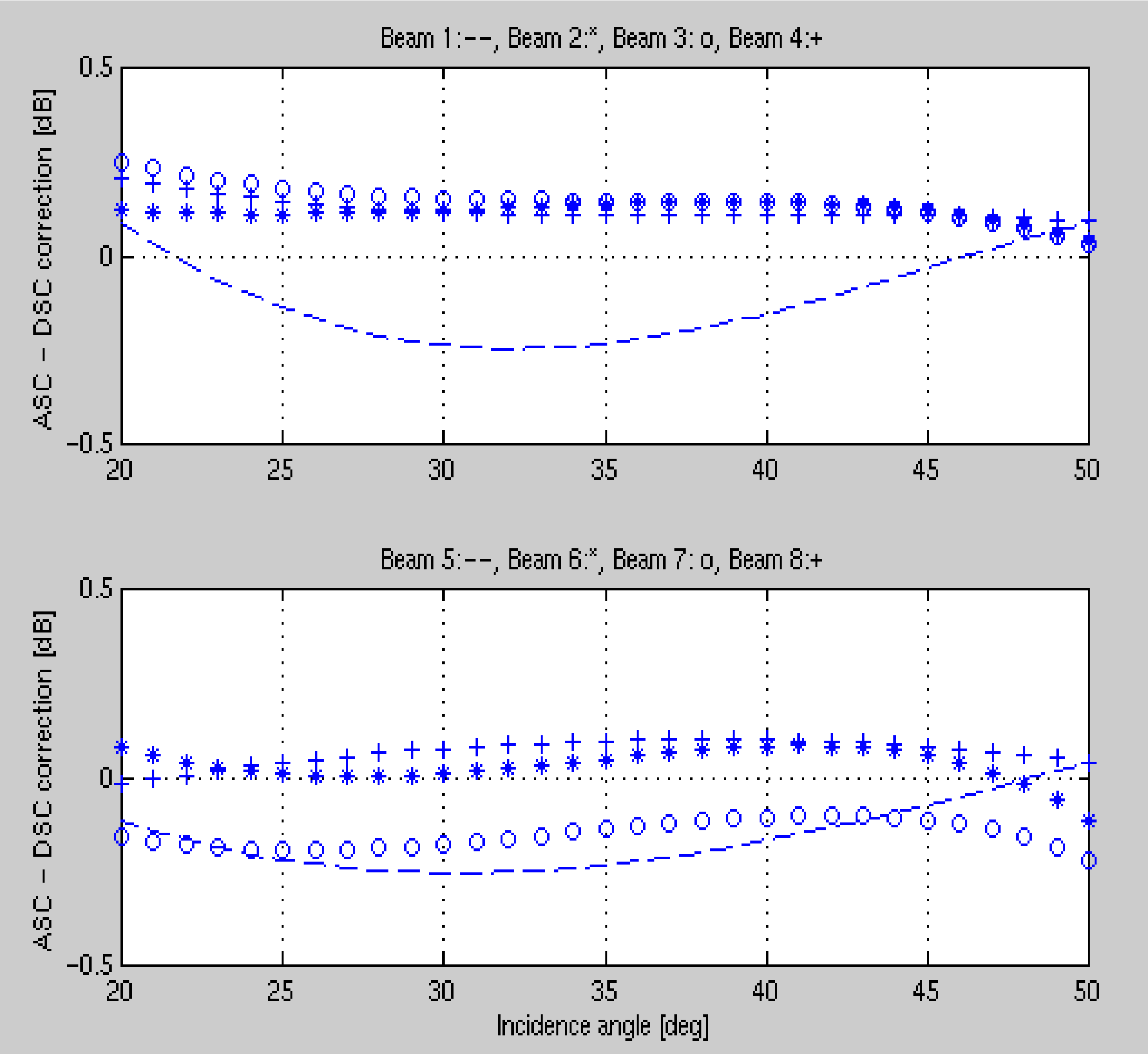

Figure 37: Difference between ascending and descending based beam balance corrections calculated from November 96 data over Amazon

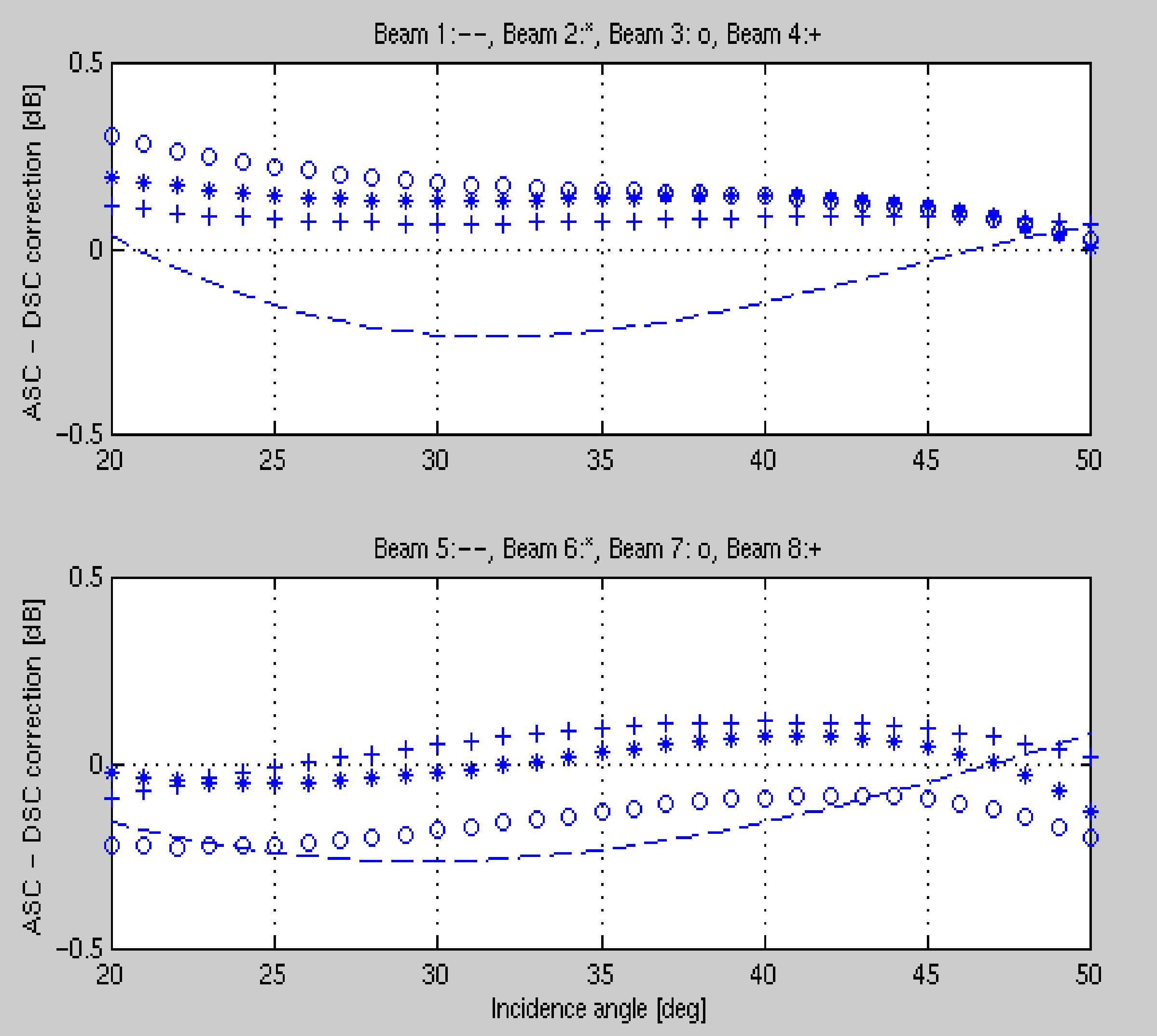

Figure 38: Difference between ascending and descending based beam balance corrections calculated from January 97 data over Amazon

Figure 39 shows Δc plotted from the September 96 data taken over homogenous area in central Russia. Again, magnitudes of differences are within 0.5 dB between 20°-50° incidence angles. However, differences are not the same as for Amazon region. This suggests that Δc is latitude-dependent, as Amazon basin (Equatorial, Figure 18) and central Russia (Figure 20) are separated by ≈ 50^o in latitude. This fact suggests that the system bias causing Δc changes with the latitude during a satellite revolution. The most likely parameter that can behave like that and that can influence σ^o is the spacecraft attitude. The remainder of the dissertation will attempt to attribute $\Delta c \neq 0$ to a mean bias in ADEOS attitude.

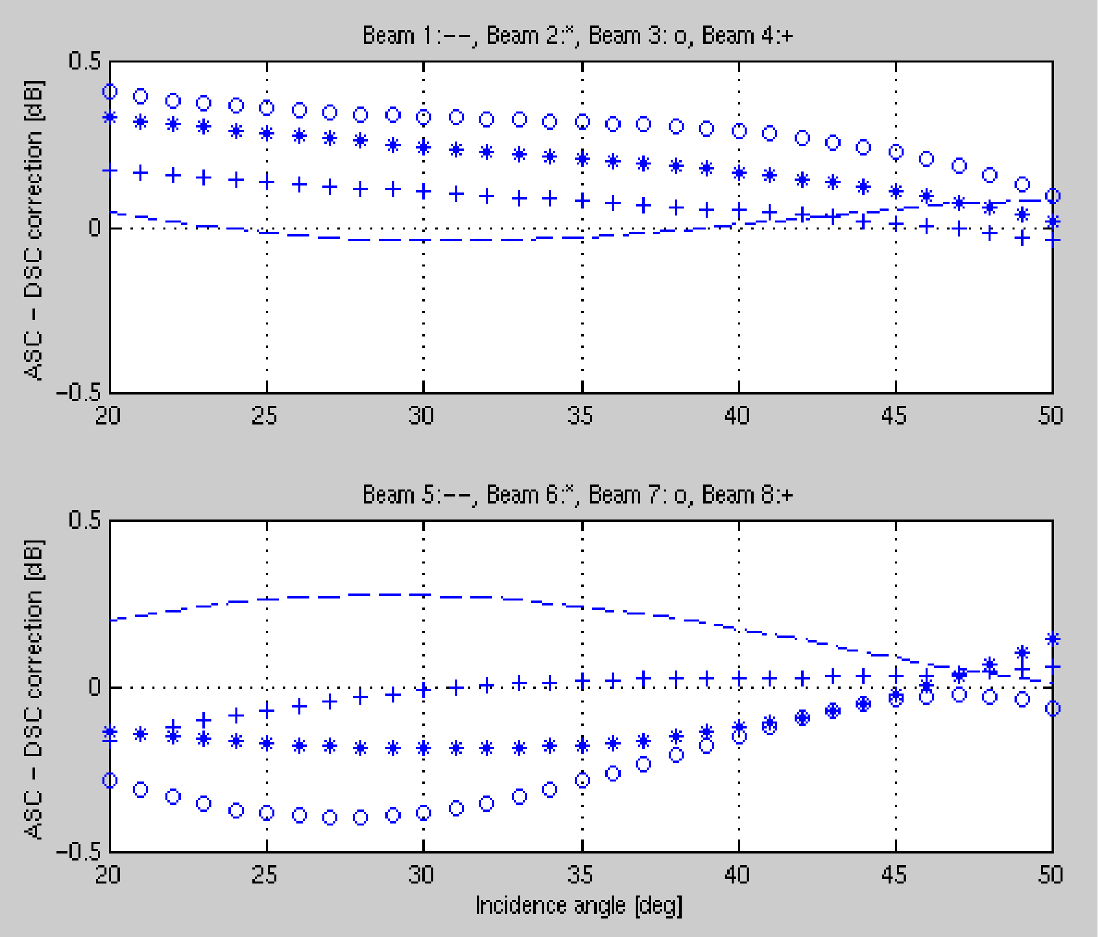

Figure 39: Difference between ascending and descending based beam balance corrections calculated from September 96 data over central Russia.

Diurnal differences in beam balance corrections were present in all other on-orbit NSCAT beam balance methods (ocean, ice, ground station). Therefore, it was decided to use ascending-based $c_{b,A}(\theta)$ separately from descending-based $c_{b,D}(\theta)$. These separated sets of corrections were accepted for the final NSCAT σ^o reprocessing. The results plotted on Figures 22-28 and tabulated in Appendix A are the average of both sets:

$$C_b(\theta) = \frac{1}{2}\left[c_{b,A}(\theta) + c_{b,D}(\theta)\right]. \tag{5.2}$$

The separate corrections made σ^o set consistent among all beams, but the reasons for diurnal difference remained unresolved. This difference can not be a real geophysical property of the target because $c_b(\theta)$ is a measure of relative beam biases alone and is decoupled from target's parameters. Only additional system bias can cause such differences, which is consistent with the assumption that the spacecraft attitude is responsible for this discrepancy.

5.3 ADEOS attitude determination model

Spacecraft attitude is a set of angular variables: roll, pitch, and yaw. These are the angles of spacecraft rotation with respect to three orthogonal axes. Attitude variables are illustrated on Figure 40 for a three-axis stabilized satellite. Yaw axis is the line connecting the spacecraft and Earth's center. Pitch axis is normal to the orbital plane containing velocity vector and yaw axis. Roll axis is orthogonal to both pitch and yaw.

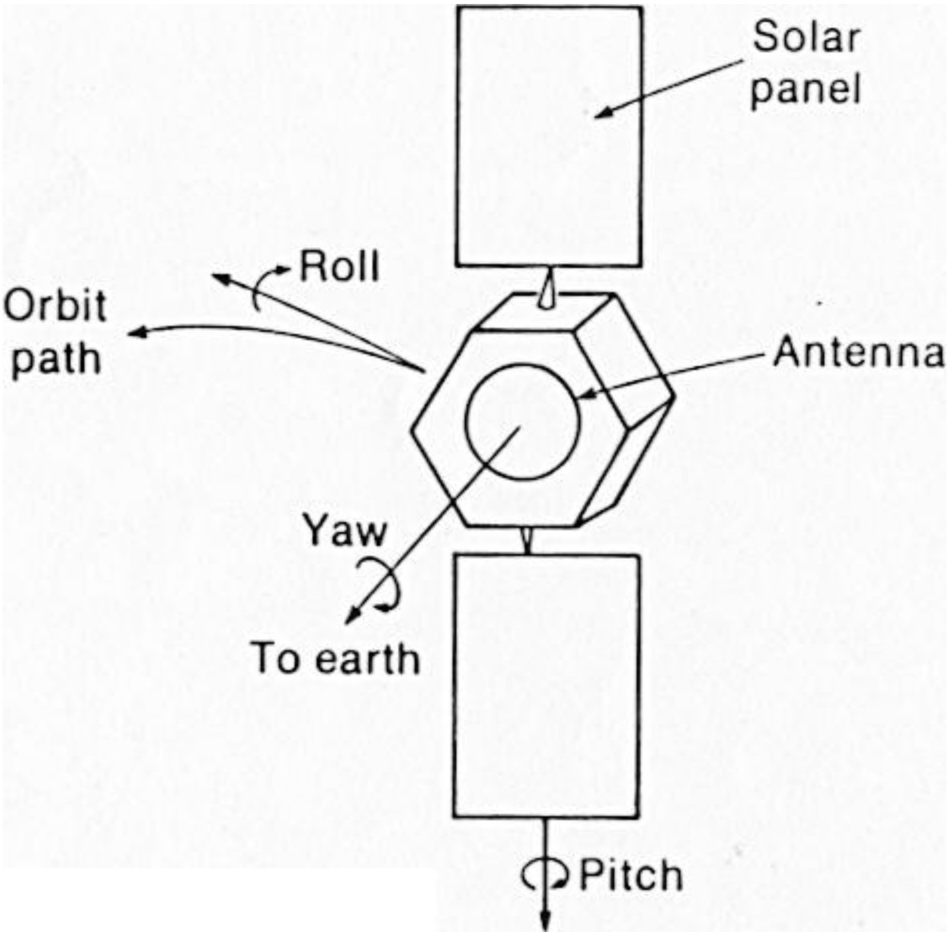

Figure 40: Attitude variables for a three-axes stabilized satellite

The proposed method for ADEOS attitude determination uses NSCAT σ^o measurements. It combines beam balance and variable attitude to estimate the attitude that will produce consistent ascending-based ($c_{b,A}(\theta)$) and descending-based ($c_{b,D}(\theta)$) corrections. Mathematical formulation uses an objective function:

$$J(a_A, a_D) = \sum_{b=1}^{8} \left| \vec{c}_{b,A}(a_A) - \vec{c}_{b,D}(a_D) \right| \tag{5.3}$$

Variable a_A denotes the ascending attitude set:

$$a_A = (r_A, p_A, y_A)\,, \tag{5.4}$$

where r_A, p_A, and y_A are mean roll, pitch, and yaw during ascending passes over Amazon, and a_D is a descending counterpart. Since attitude is assumed to be changing during an orbit, a_A and a_D are not correlated (ascending and descending passes are separated by ≈ 12 hours) and $a_A \neq a_D$. Usual $c_b(\theta)$ representation is substituted in (5.3) by $\vec{c}_{b,X}(a_X)$, where incidence angle dependence is taken into account by the vector representation:

$$\vec{c}_{b,X}(a_X) = \begin{bmatrix} c_{b,X}(\theta_1, a_X) \\ c_{b,X}(\theta_2, a_X) \\ \vdots \\ \vdots \\ c_{b,X}(\theta_N, a_X) \\ \end{bmatrix}. \tag{5.5}$$

The additional subscript X denotes spacecraft direction A: ascending and D: descending. Corrections $c_{b,X}(\theta,a_X)$ are defined in (4.9) and substituting this definition in (5.5) gives:

$$\vec{c}_{b,X}(a_X) = \begin{bmatrix} \bar{\sigma}^o(\theta_1, a_X) - \sigma^o_{b,X}(\theta_1, a_X) \\ \bar{\sigma}^o(\theta_2, a_X) - \sigma^o_{b,X}(\theta_2, a_X) \\ \vdots \\ \vdots \\ \bar{\sigma}^o(\theta_N, a_X) - \sigma^o_{b,X}(\theta_N, a_X) \end{bmatrix}\,, \tag{5.6}$$

where $\overline{\sigma}^{o}(\theta)$ [dB] is, as before, the referent mean response at incidence angle θ from all beams and $\sigma_{b}^{o}(\theta)$ is the response from individual beam *b*. In further derivation, incidence angle dependence will be suppressed for simpler notation:

$$\vec{\varepsilon}_{b.X}(a_X) = \overline{\sigma}^{o}(a_X) - \sigma_{b}^{o}(a_X)\,. \tag{5.7}$$

Using this simplified notation, the objective function (5.3) becomes:

$$J(a_A, a_D) = \sum_{b=1}^{8} \left| \overbrace{\overline{\sigma}_{A}^{o}(a_A) - \sigma_{b,A}^{o}(a_A)}^{\varepsilon_{b,A}(a_A)} - \left[\overbrace{\overline{\sigma}_{D}^{o}(a_D) - \sigma_{b,D}^{0}(a_D)}^{\varepsilon_{b,D}(a_D)} \right] \right| \,. \tag{5.8}$$

It is desired to minimize the objective function (5.8), i.e., to find the attitude that will make $\vec{\varepsilon}_{b,A}(a_A)$ and $\vec{\varepsilon}_{b,D}(a_D)$ as close as possible. Desired attitude can be formally written as a pair of sets *A* and *D* satisfying:

$$(A,D) = Arg\{\min J(a_A, a_D)\}\ , \tag{5.9}$$

where $A=(R_A,P_A,Y_A)$ is the set containing the best mean ADEOS roll, pitch, and yaw for ascending passes and *D* is the descending counterpart.

Calculating $J(a_A,a_D)$ for all trial values of pairs of sets (a_A,a_D) would require unavailable computational resources. NSCAT data processing algorithm relies on the attitude information from the attitude determination and control subsystems on board ADEOS. This information is part of the Level 1.0 data (section 3.5). By changing attitude variables in Level 1.0 records, the effects of attitude on σ^o can be investigated. This is done introducing an approximate procedure based on pre-calculating and tabulating attitude effects. The change in σ^o induced by the attitude bias a_X, compared to the zero-bias (ADEOS reported) attitude is:

$$\Delta\sigma^o(a_X) = \sigma^o(a_X) - \sigma^o(0) \ . \tag{5.10}$$

Combining (5.8) and (5.10), the objective function develops to:

$$J(a_A, a_D) = \sum_{b=1}^{8} \left| \begin{matrix} \overline{\sigma}_A^o(0) + \Delta\overline{\sigma}_A^o(a_A) - \sigma_{b,A}^o(0) - \Delta\sigma_{b,A}^o(a_A) - \\ - \left[\overline{\sigma}_D^o(0) + \Delta\overline{\sigma}_D^o(a_D) - \sigma_{b,D}^o(0) - \Delta\sigma_{b,D}^o(a_D) \right] \end{matrix} \right| \ . \tag{5.11}$$

Regrouping the factors:

$$J(a_A, a_D) = \sum_{b=1}^{8} \left| \begin{matrix} \overbrace{\overline{\sigma}_A^o(0) - \sigma_{b,A}^o(0)}^{c_{b,A}} - \left[\overbrace{\overline{\sigma}_D^o(0) - \sigma_{b,D}^o(0)}^{c_{b,D}} \right] + \\ \underbrace{+ \Delta\overline{\sigma}_A^o(a_A) - \Delta\sigma_{b,A}^o(a_A) - \Delta\overline{\sigma}_D^o(a_D) + \Delta\sigma_{b,D}^o(a_D)}_{T(A,D)} \end{matrix} \right| \tag{5.12}$$

Recognizing beam balance corrections for nominal attitude analysis ($\vec{c}_{b,A}(a_A)$ and $\vec{c}_{b,D}(a_D)$), the objective function separates in two parts. First part is calculated based on the large data set taken over a homogenous target as elaborated throughout chapter 4:

$$\Delta c = c_{b,A}(\theta) - c_{b,D}(\theta) = \vec{c}_{b,A} - \vec{c}_{b,D} \ . \tag{5.13}$$

Second part of (5.12), denoted as $T(a_A,a_D)$ takes into account effect of spacecraft attitude on σ^o. T contains only Δ factors and is zero for nominal, ADEOS reported attitude. All additive terms defining $T(a_A,a_D)$ can be pre-calculated and stored in a look-up table. This enables efficient processing and evaluation of $J(a_A,a_D)$ for various (a_A,a_D) pairs. Dimension of the look-up table is R X 6, since every $\Delta\sigma^o(a_X)$ is defined at given ascending $a_A=(r_A,p_A,y_A)$ or descending $a_D=(r_D,p_D,y_D)$ roll, pitch, and yaw triplet. The other dimension, R, depends on the resolution at which the table is calculated (the step in roll, pitch, and yaw bias at which $\Delta\sigma^o(a_X)$ is evaluated). The triplets a_A and a_D resulting in the minimum value of (5.12) are the proposed attitude adjustment that will make ascending-based and descending-based corrections consistent. This is a restatement of the equation (5.9).

5.4 ADEOS attitude analysis results

The model defined in preceding section is used to propose the proper ADEOS attitude. The objective function $J(a_A,a_D)$ defined by (5.12) is parametrically calculated for different combinations of (a_A,a_D) pairs. This becomes a six dimensional variation since

$$J(a_A, a_D) = J(r_A, p_A, y_A, r_D, p_D, y_D) \ . \tag{5.14}$$

Before actually calculating $J(a_A,a_D)$, the second part of (5.12), $T(a_A,a_D)$, is tabulated for a reasonable range of roll, pitch, and yaw angles. The interval of ± 0.5° around the nominal attitude is accepted, with a step of 0.1°. It is reasonable to expect this interval to cover practical fluctuations in attitude variables. This scheme results in 11^6 entries in the T table (there are 11 steps in X ± 0.5° interval if the step is 0.1°, and there are six attitude variables). First part of the expression (5.12) is the zero-attitude beam balance calculated in chapter 4. Combining the zero-attitude $\Delta c = c_{b,A}(\theta)$- $c_{b,D}(\theta)$ and the look-up table entry $T(a_A,a_D)$, $J(a_A,a_D)$ is numerically evaluated in order to identify arguments (A,D) = $(R_A,P_A,Y_A,R_D,P_D,Y_D)$ resulting in the minimum $J(a_A,a_D)$.

The results for ± 0.5° interval are shown on figures 41-46 and tabulated in tables 3-5. Figure 41 shows separately effect of each attitude variable variation on $J(a_A,a_D)$. Because the minimum $J(a_A,a_D)$ minimizes

$$\sum_{b=1}^{8} \Delta c_b = \sum_{b=1}^{8} \left[c_{b,A}(\theta) - c_{b,D}(\theta) \right] \ , \tag{5.15}$$

$J(a_A,a_D)$ is sensitive to $(a_A - a_D)=(r_A-r_D,\ p_A-p_D,\ y_A-y_D)$ rather than to a_A and a_D alone. Therefore, the objective function is shown versus $a_A - a_D$. Values of the objective function are normalized to the desired minimum value of $J(A,D)$ such that

$$\bar{J}(a_A, a_D) = J(a_A, a_D) - J(A, D) \ , \tag{5.16}$$

where (A,D) are the attitude sets satisfying (5.9). The normalization (5.16) equates the value of the minimum objective function to zero. Figure 41, thus, shows $\bar{J}$ (a_A,a_D) as a function of the difference in ascending and descending attitude a_A - a_D . The plot uses nominal-attitude Δc based on NSCAT measurements taken during three weeks in November 96. The objective function is calculated combining this Δc and $T(a_A,a_D)$ for all cases in the ± 0.5^o range around the zero attitude. The figure therefore shows mean attitude effects averaged over the three-week period and applicable for Equatorial latitudes.

$\bar{J}$ (a_A,a_D) on Figure 41 is almost independent of roll variations (shown as '--' line on the figure). This means that beam balance correction difference is not sensitive to roll and that the roll angle can not be detected using this method. This is not a case for pitch and yaw angles. There is a clearly distinguishable minimum at p_A - p_D = -0.02^o and y_A - y_D = 0.25^o. This means that a consistent $\vec{\varepsilon}_{b,A}(a_A)$ and $\vec{\varepsilon}_{b,D}(a_D)$ pairs are achieved if nominal ADEOS attitude is adjusted such that the ascending pitch angle is slightly decreased relative to the descending pitch angle (' -.- ' line). The ascending yaw angle should be 0.25^o larger than the descending yaw (solid line). The combined effect of significant variables (pitch and yaw) is shown on Figure 42. The three-dimensional plot $J = f(p_A - p_D, y_A - y_D)$ shows the deepest valley along p_A-p_D=-0.02^o and y_A-y_D = 0.25^o. Numerical values corresponding to Figures 41 and 42 are tabulated in Table 3. Although the individual values of attitude variables are listed, it is the differences p_A-p_D and y_A-y_D

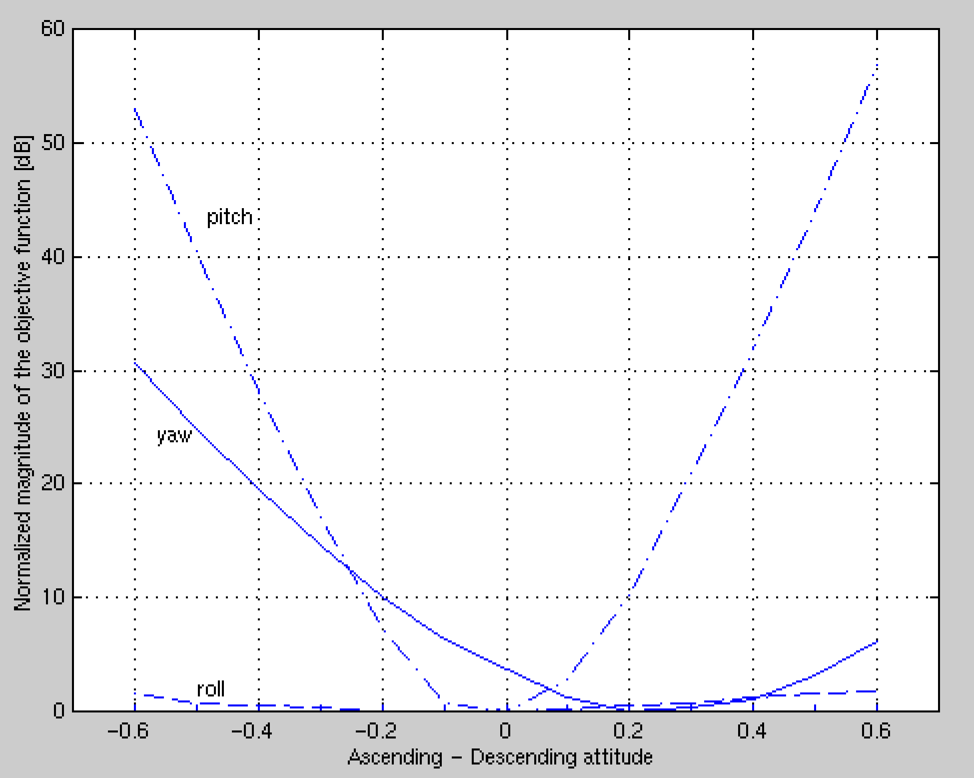

Figure 41: Attitude effects on the objective function for November 96 data over Amazon

that affects beam balance rather than the individual values of angles. Roll angles corresponding to the "best" attitudes *A* and *D* (5.9) are also given, although roll does not affect the objective function, as obvious from Figure 41.

Attitude axis	**Ascending**	**Descending**
roll	0.0°	0.0°
pitch	-0.1°	-0.1°
yaw	0.2°	-0.1°

Table 3: Values of attitude angles resulting in the most consistent ascending and descending based corrections for November 96 data over Amazon (0.1° resolution)

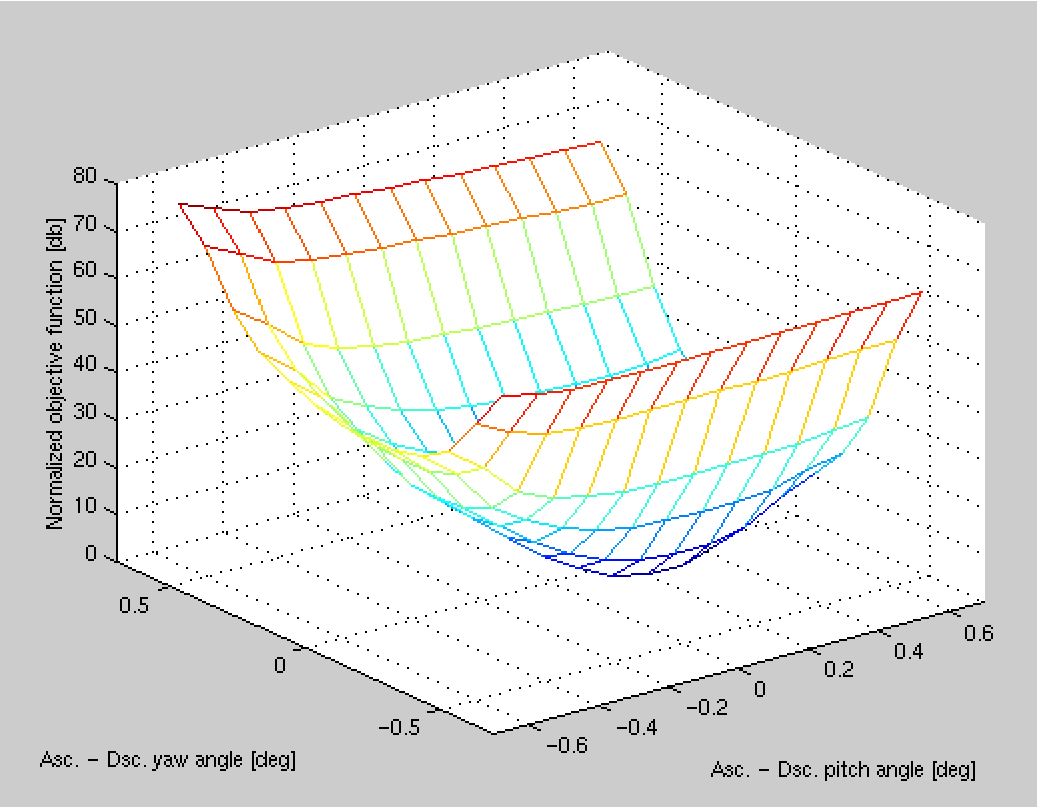

Figure 42: Combined effect of significant attitude variables for November 96 data over Amazon

Figure 43 shows attitude effects on the data taken in January 97 over Amazonian homogenous area. The shapes of $\bar{J}$ (a_A,a_D) versus r_A-r_D, p_A-p_D, and y_A-y_D are very similar to November 96 results. It shows that mean attitude bias has not changed much between two periods. Figure 44 also agrees with Figure 42, showing in three dimensions $\bar{J}$ as a function of both p_A-p_D and y_A-y_D. As for November 96, the deepest valley is at the intersection of p_A-p_D= -0.02^o and y_A-y_D= 0.25^o lines. January 97 ADEOS attitude results are tabulated in Table 4. It is similar to Table 3 for November 96 data, but the best pitch is now 0^o (reported correctly) for both ascending and descending passes, while both ascending and descending yaw angles are higher with ≈ 0.2^o difference.

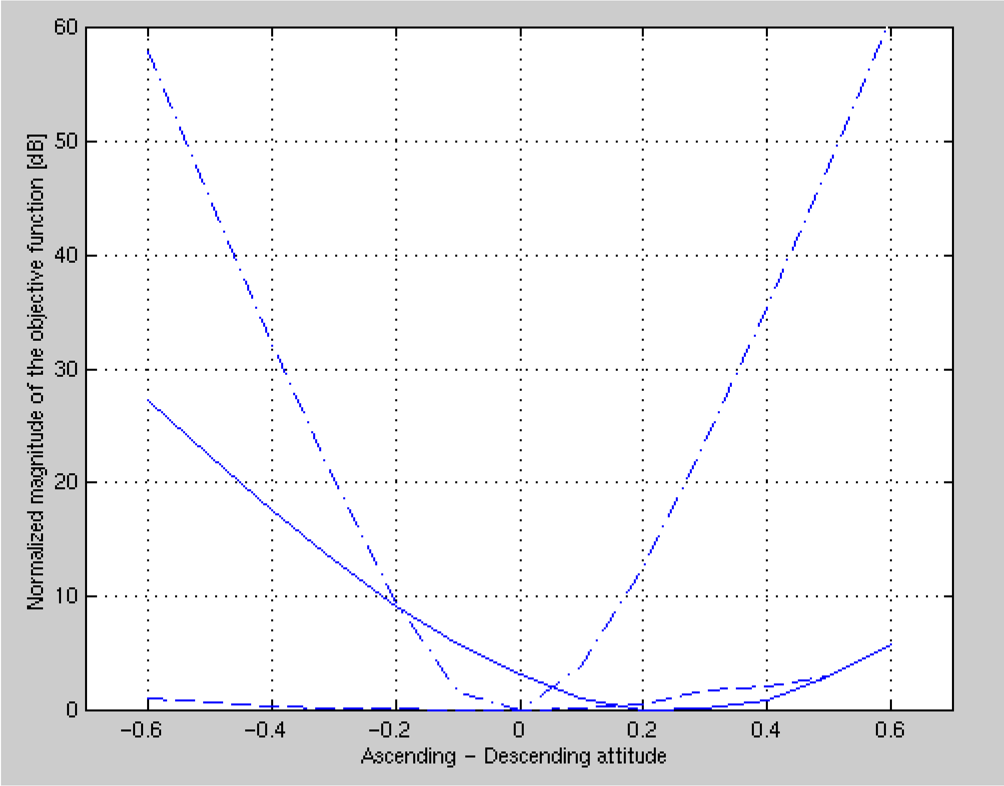

Figure 43: Attitude effects on the objective function for January 97 data over Amazon

Attitude axis	**Ascending**	**Descending**
roll	0.0^0	0.0^0
pitch	0.0^o	0.0^o
yaw	0.3^0	0.1^0

Table 4: Values of attitude angles resulting in the most consistent ascending and descending based corrections for January 97 data over Amazon (0.1^o resolution)

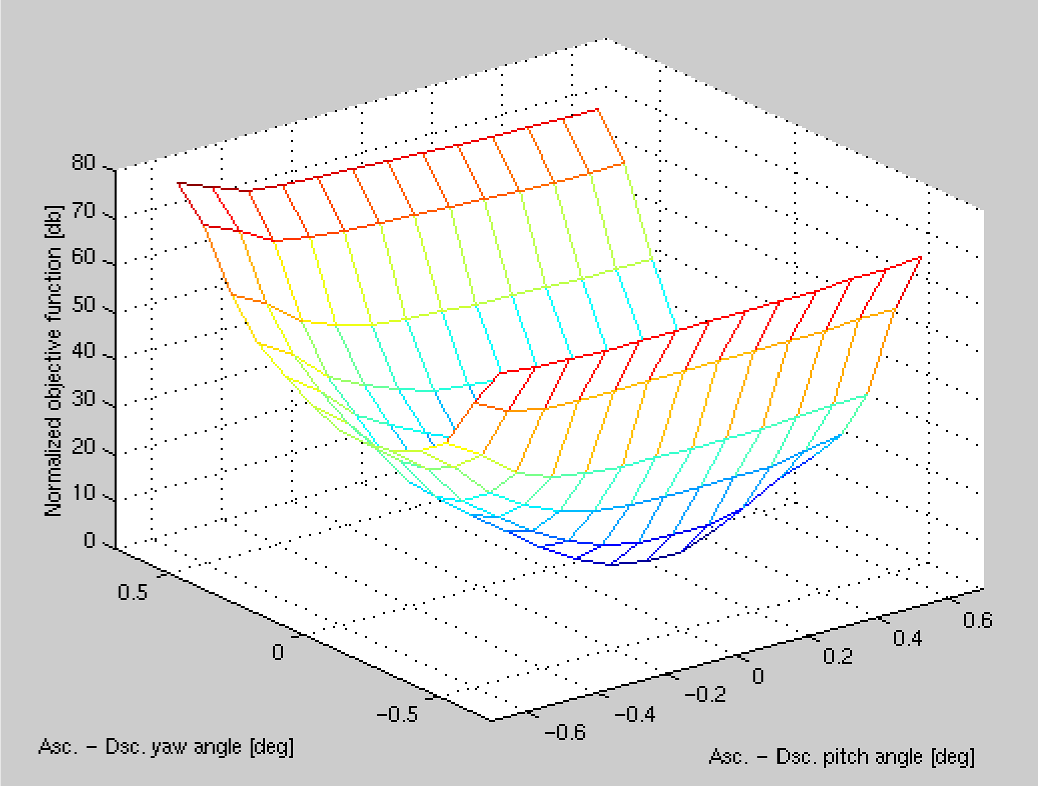

Figure 44: Combined effect of significant attitude variables for January 97 data over Amazon

Since the baseline zero-attitude beam balance correction was calculated also from data over central Russia, the attitude analysis is repeated for this data set as well. The results are plotted on Figure 45. A three-week period in November 96 is used. As for Amazon data, roll effects are negligible, leaving pitch and yaw angles as the attitude variables with clear minimum and large effect on beam balance. A combined effect of pitch and yaw on the objective function is shown on the three-dimensional plot on Figure 46. It shows normalized objective function $\bar{J}$ as a function of both p_A-p_D and y_A-y_D. The best attitude sets A and D are identified in Table 5. However, it is as before the difference p_A-p_D and y_A-y_D that is important, rather than A and D alone.

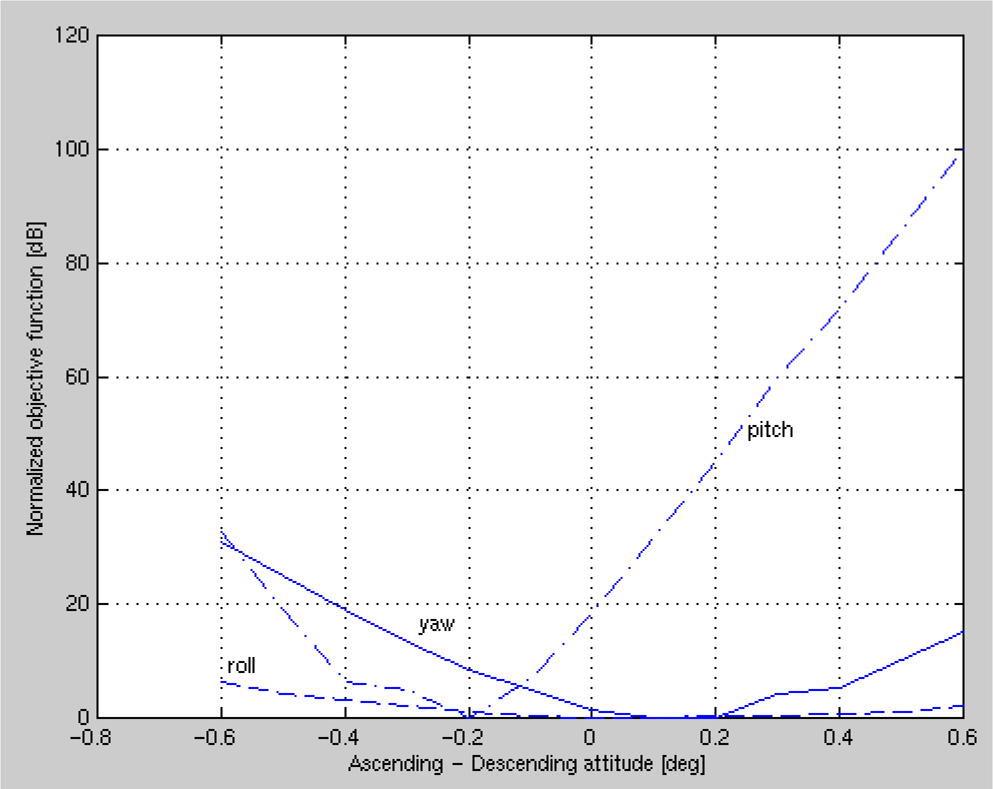

Figure 45: Attitude effects on the objective function for November 96 data over central Russia

The important observation from comparing results from Amazon (Figures 41-44 and Tables 3 and 4) and Russia (Figures 45-46 and Table 5) is the difference between these results. While p_A-p_D= -0.02° and y_A-y_D= 0.25° was estimated from the Amazon data,

Attitude axis	**Ascending**	**Descending**
Roll	0.2^0	0.1^0
Pitch	-0.2°	0.0°
Yaw	0.2^0	0.0^0

Table 5: Values of attitude angles resulting in the most consistent ascending and descending based corrections for November 96 data over central Russia (0.1° resolution)

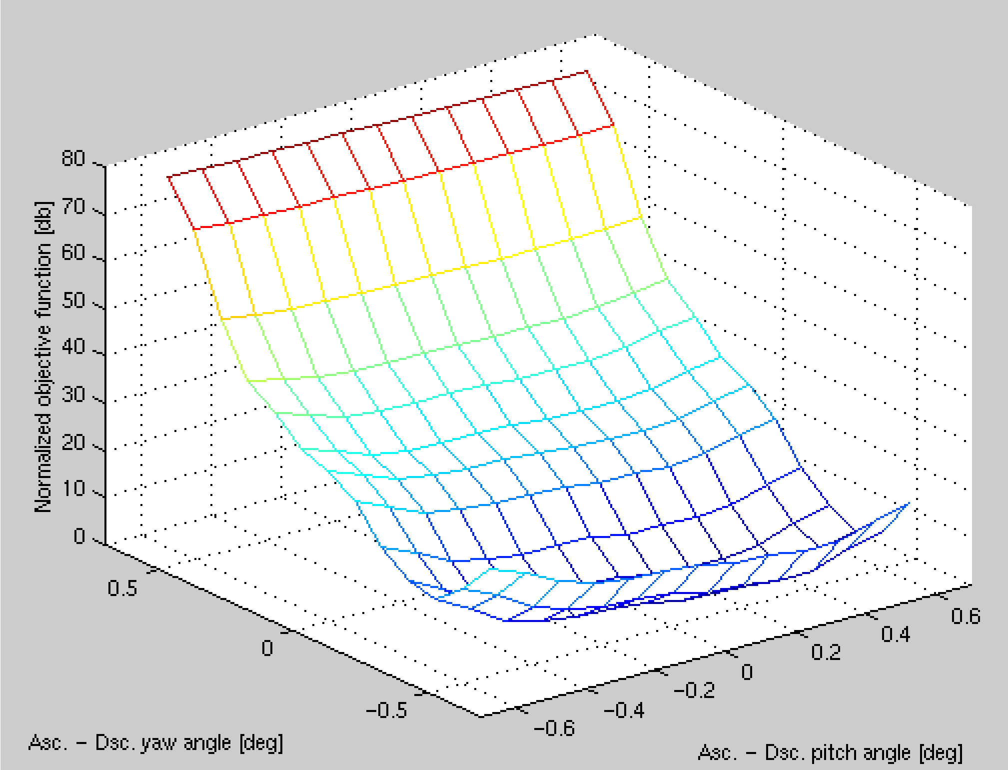

Figure 46: Combined effect of significant attitude variables for November 96 data over central Russia

the corresponding biases from the analysis of the Russian data are p_A - p_D = -0.2^o and y_A - y_D = 0.15^o. This difference points to orbital position dependence of the mean attitude biases. This is in agreement with some other studies (Dr. Joe Hashmall, NASA Goddard Space Flight Center, personal communication) that observed varying attitude throughout a single ADEOS revolution. All similar studies point to inconsistencies in the ADEOS-reported attitude. These inconsistencies are estimated to be no more than 0.3^o, but this bias translates into bias in $\Delta\sigma^o$ significant for required accuracy of the NSCAT instrument.

5.5 The effect of ADEOS attitude adjustment

The final section will show, through a series of plots, the effect of applying attitude adjustment estimated in previous section. Using the look-up table $T(A,D)$, σ^o measurements are adjusted and recalculated. The attitude sets tabulated in Tables 3-5 are used for corresponding σ^o data set. Plots in this section will illustrate the improvement in consistency between ascending and descending data when proposed attitude adjustment is applied.

First set of figures (Figures 47-53) applies to November 96 data taken over Amazon mask. Figure 47 shows raw uncorrected σ^o measurements from all NSCAT beams. Beams are not identified, as only their scatter is important to evaluate beam balance and attitude analysis results. Ascending and descending passes are separated. Figure 48 shows in more detail the scatter (at different incidence angles) in σ^o among all beams from Figure 47. The standard deviation around the mean of all beams is 0.24 dB. After applying the mean ascending/descending beam balance corrections $\frac{1}{2}\left[c_{b,A}(\theta)+c_{b,D}(\theta)\right]$, $\sigma_b^o(\theta)$ response becomes as plotted on Figure 49. The scatter among different beams is reduced and standard deviation decreases to 0.13 dB. The new scatter is plotted as a function of incidence angle on Figure 50. This improvement is achieved with the nominal attitude. Further improvement is reached when attitude is adjusted according to results from previous section. For the adjusted attitude, the beam balance correction is recalculated. When $r_A = 0^o$, $p_A = -0.1^o$, $y_A = 0.2^o$, $r_D = 0^o$, $p_D = -0.1^o$, and $y_D = -0.1^o$, is applied (Table 3), the $\sigma_b^o(\theta)$ response is as in figure 51. The scatter is plotted on Figure 52 and the standard deviation is as low as 0.05 dB. From the plots and the drastically reduced value of standard deviation of σ^o measurements, the effect of attitude adjustment is obvious. It brought the tightest grouping of $\sigma_b^o(\theta)$, for all beams *b*.

Another illustration of the improvement possible by adjusting the ADEOS attitude is shown on Figure 53. The difference between ascending and descending beam balance corrections is shown for both nominal ADEOS (solid line) and adjusted ('--' line) attitude. The improvement is manifested as smaller Δc, i.e., $c_{b,A}(\theta) \rightarrow c_{b,D}(\theta)$, which is a consistent behavior over homogenous targets.

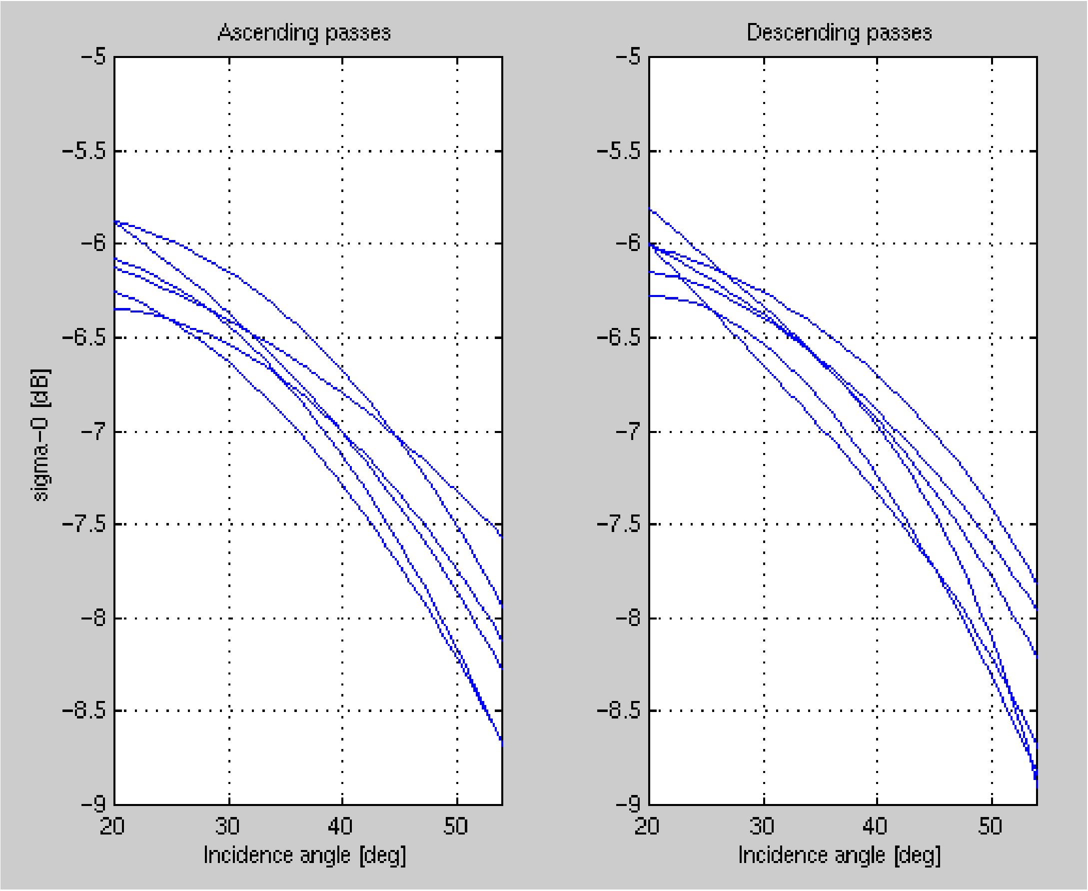

Figure 47: Raw NSCAT $\sigma_b^o(\theta)$ for Amazon November 96 data.

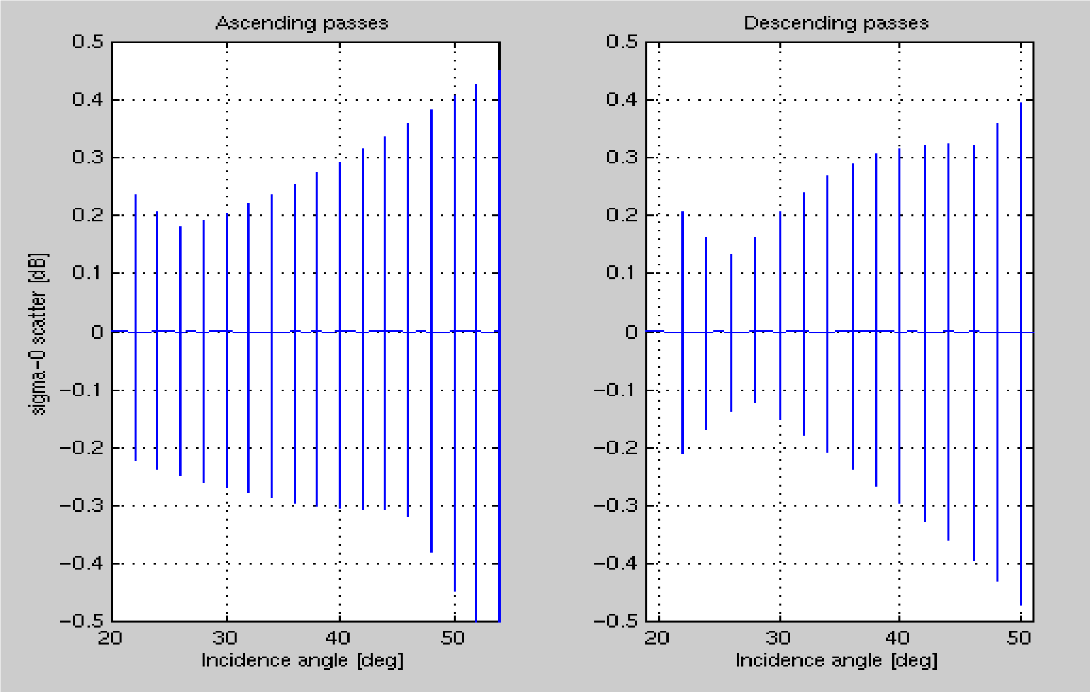

Figure 48: $\sigma_b^o(\theta)$ scatter for raw Amazon November 96 data.

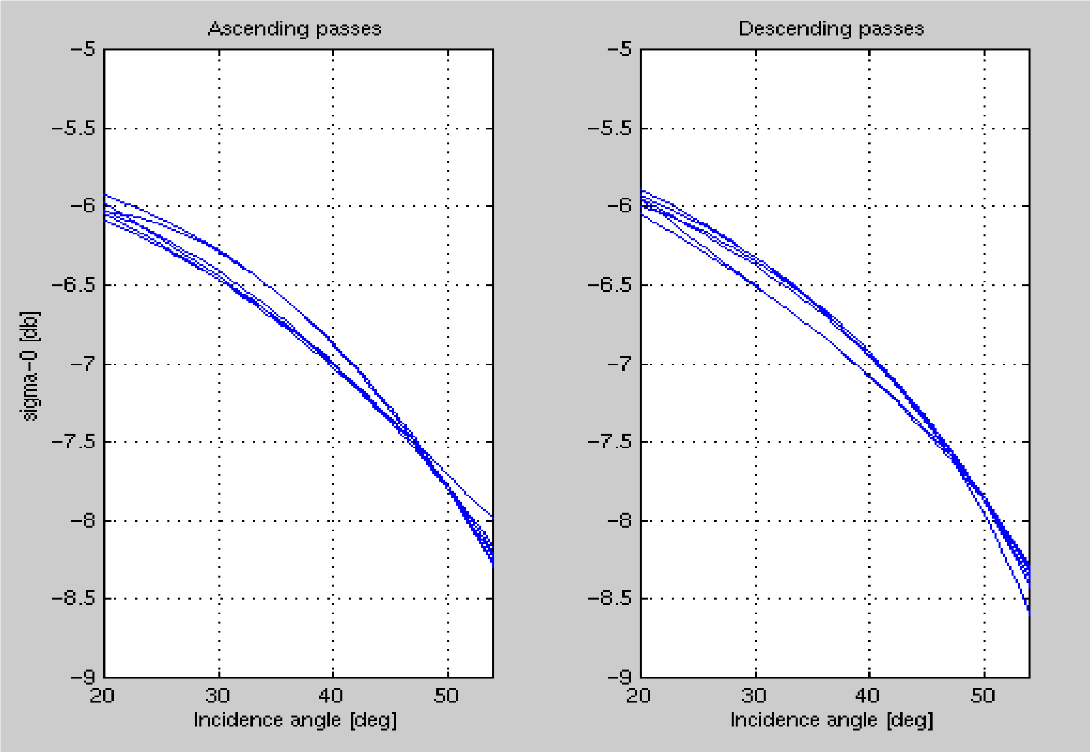

Figure 49: Zero-attitude beam balanced $\sigma_b^o(\theta)$ for Amazon November 96 data.

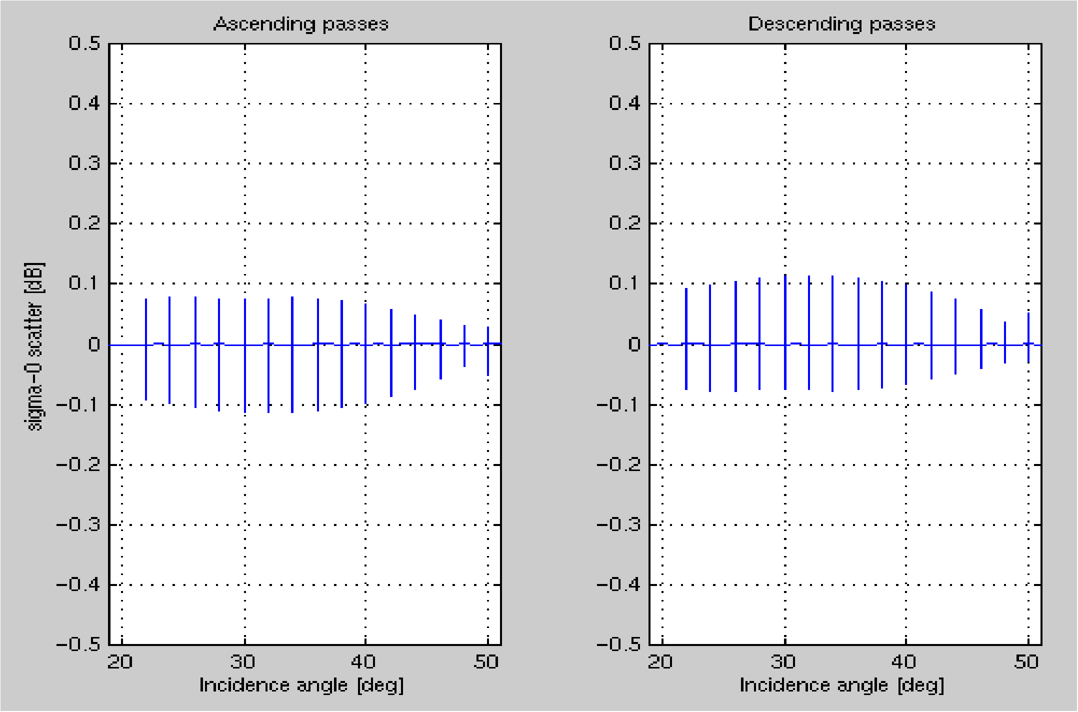

Figure 50: $\sigma_b^o(\theta)$ scatter for zero-attitude beam balanced Amazon November 96 data.

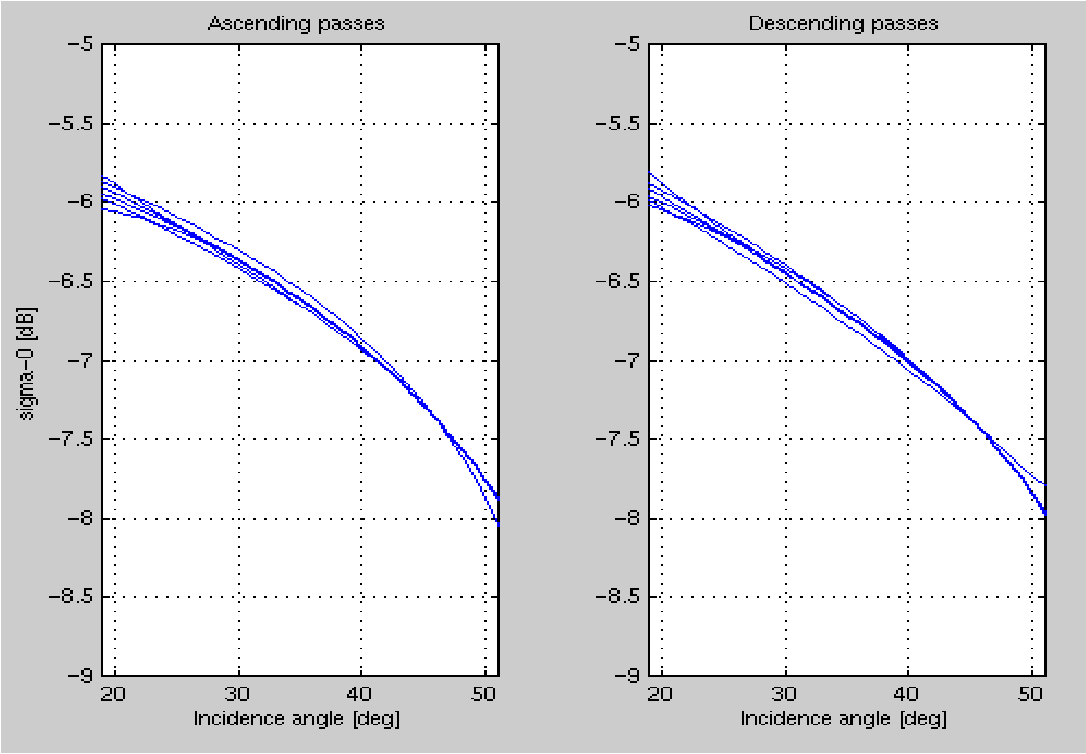

Figure 51: Attitude adjusted beam balanced $\sigma_b^o(\theta)$ for Amazon November 96 data.

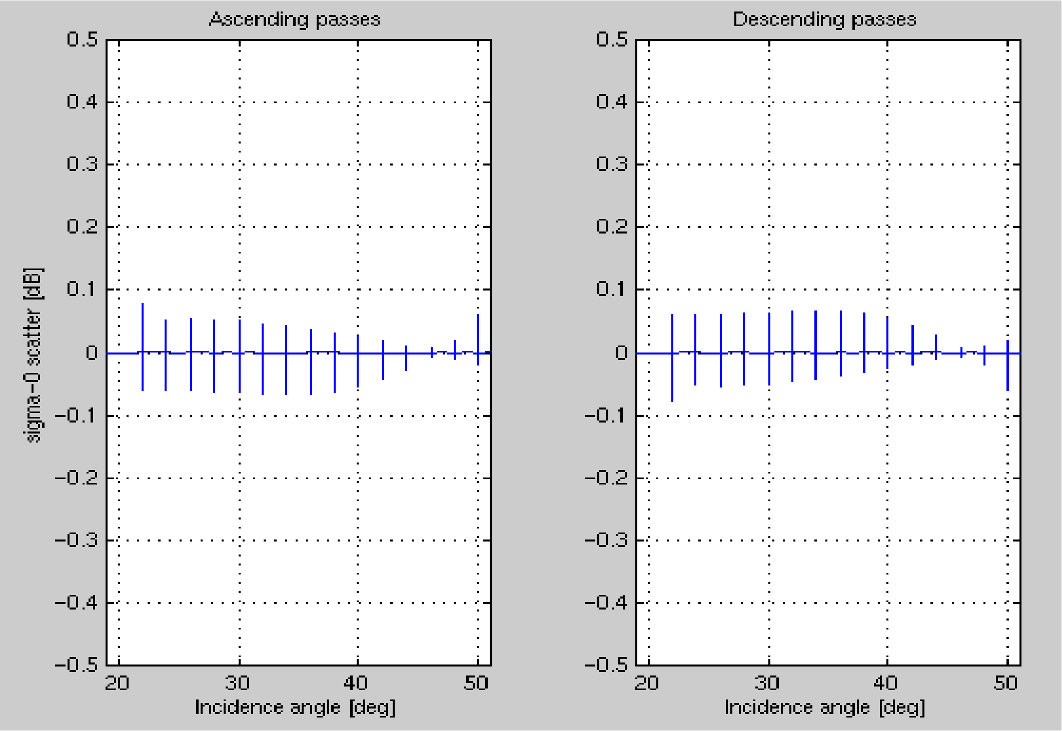

Figure 52: $\sigma_b^o(\theta)$ scatter for attitude adjusted, beam balanced Amazon November 96 data.

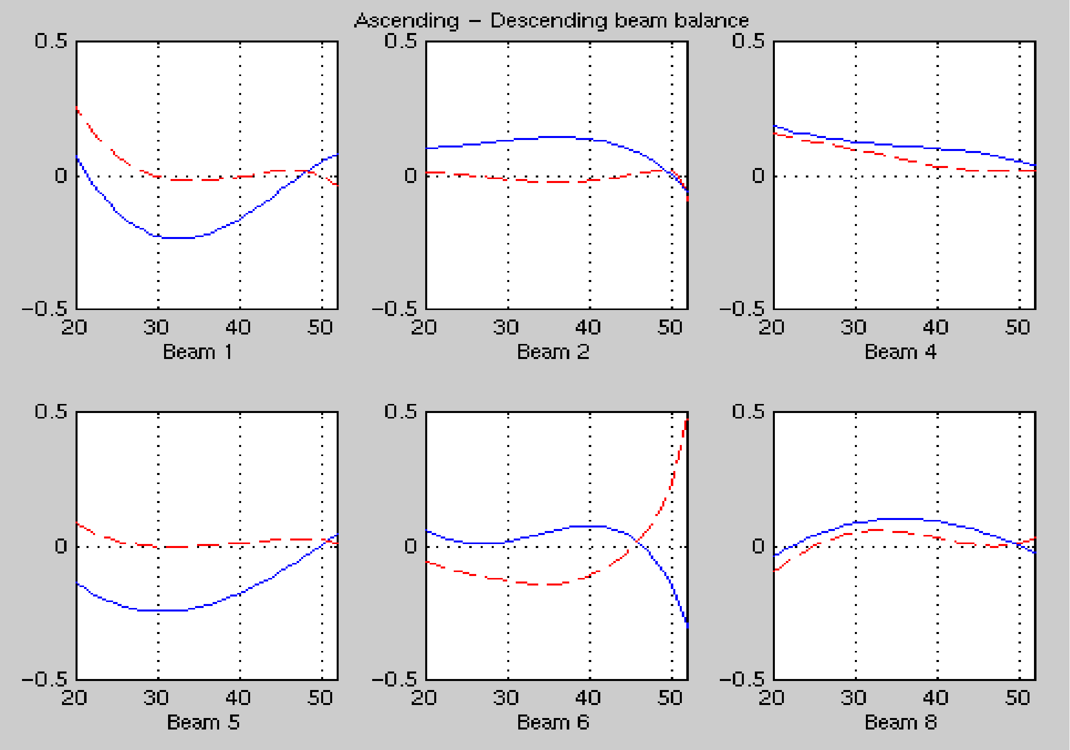

Figure 53: Improvement in NSCAT consistency after attitude adjustment, November 96 Amazon data.

A similar set of plots is repeated for another period. Figures 54-60 illustrate results of analysis of January 97 data over Amazon. Figures 54 and 55 correspond to uncorrected $\sigma_b^o(\theta)$ measurements and the scatter among individual beams, respectively. After correcting beams at nominal attitude, results on Figures 56 and 57 are obtained. There is improvement compared to raw uncorrected $\sigma_b^o(\theta)$ which show significant scatter. Again, further improvement and decrease in Δc is possible when attitude adjustment is applied. For January 97 period, the adjustment is proposed in Table 4: $r_A = 0^o$, $p_A = 0.^o$, $y_A = 0.3^o$, $r_D = 0^o$, $p_D = 0.^o$, and $y_D = 0.1^o$. Attitude adjusted and balanced $\sigma_b^o(\theta)$ response is shown on Figure 58. The corresponding scatter is plotted on Figure 59. The improvement is obvious also on Figure 60, the equivalent of Figure 53, which shows reduced Δc when the proposed attitude is applied

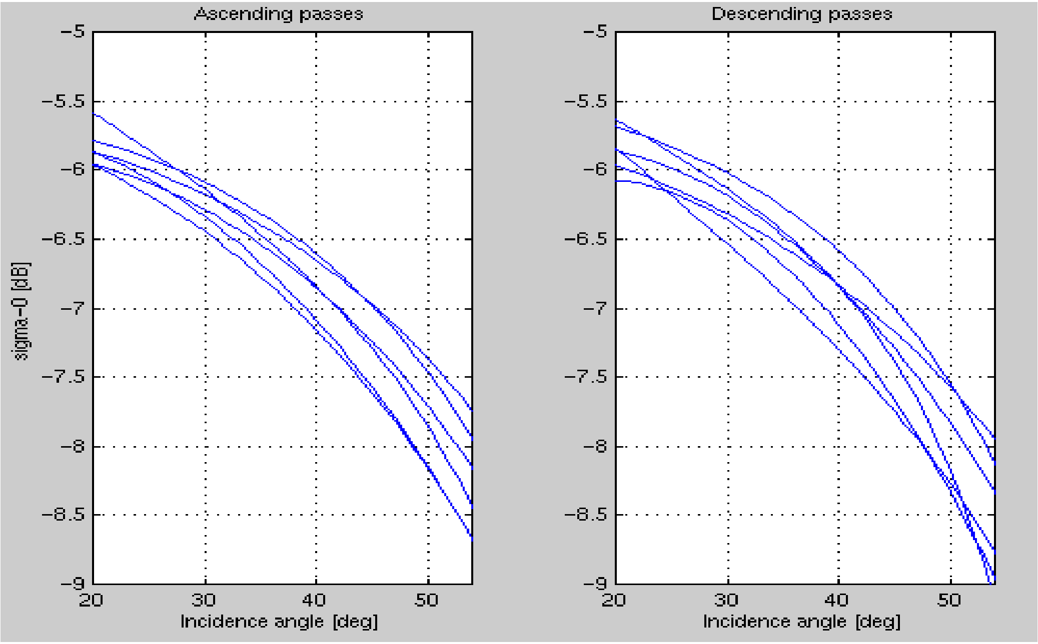

Figure 54: Raw NSCAT $\sigma_b^o(\theta)$ for Amazon January 97 data.

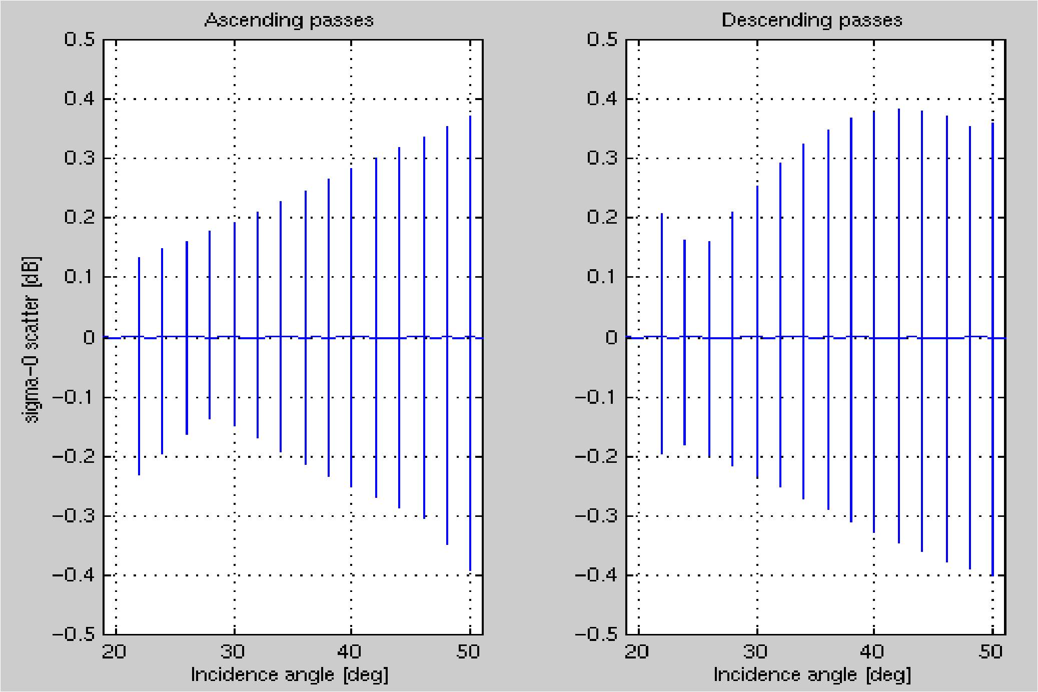

Figure 55: $\sigma_b^o(\theta)$ scatter for raw Amazon January 97 data.

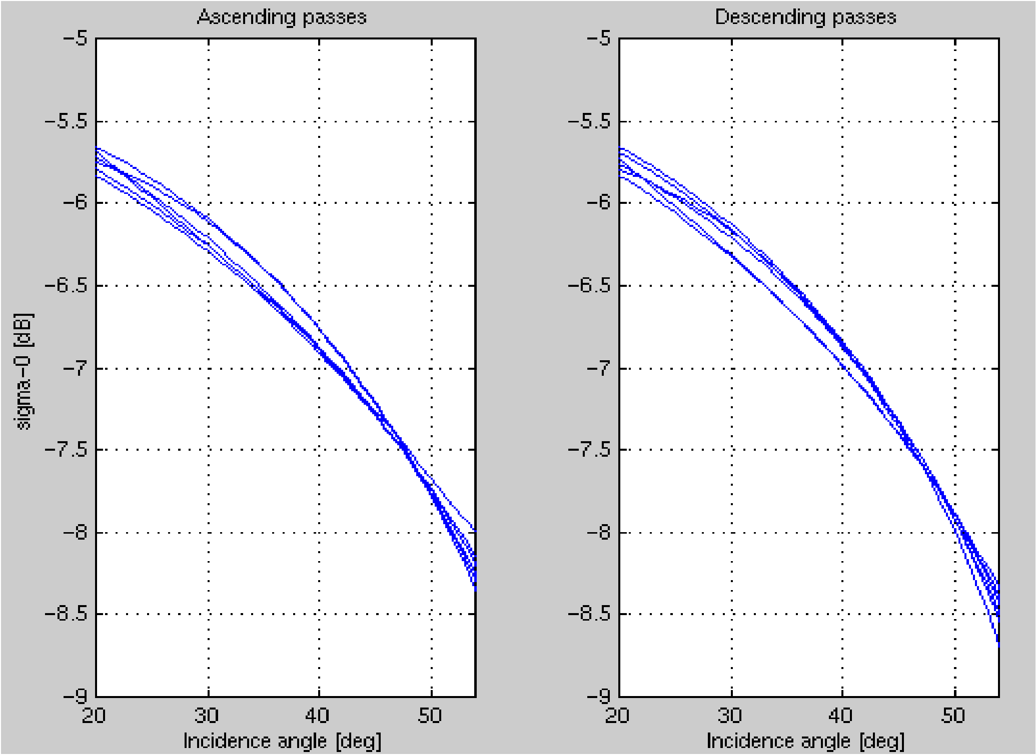

Figure 56: Zero-attitude beam balanced $\sigma_b^o(\theta)$ for Amazon January 97 data.

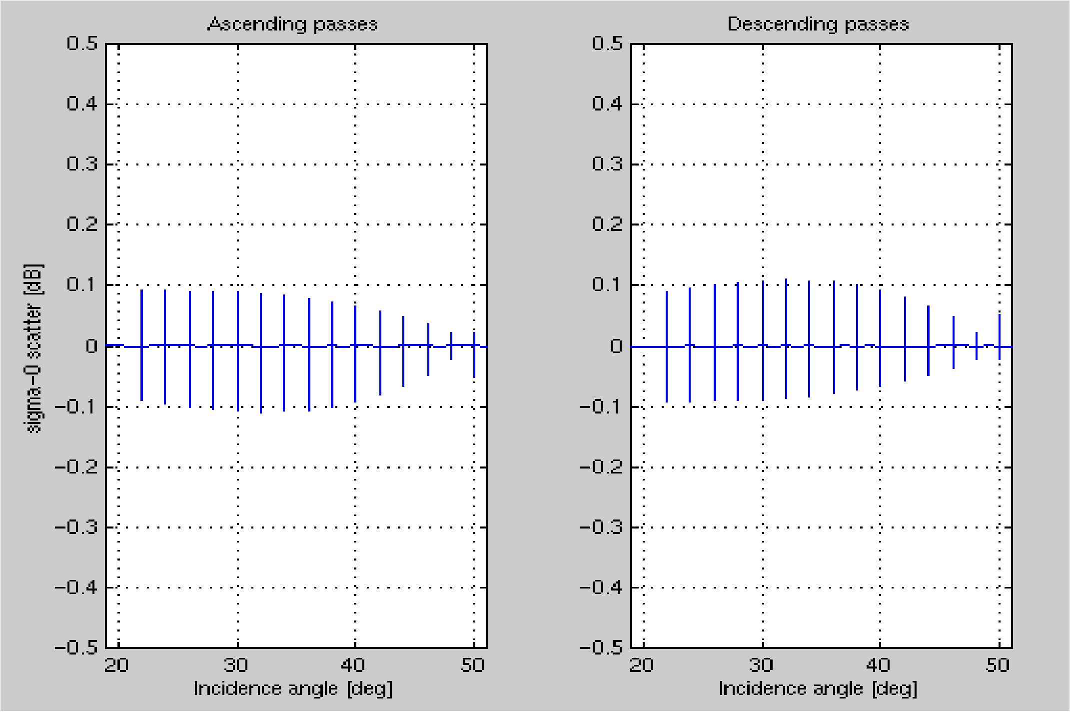

Figure 57 $\sigma_b^o(\theta)$ scatter for zero-attitude beam balanced Amazon January 97 data.

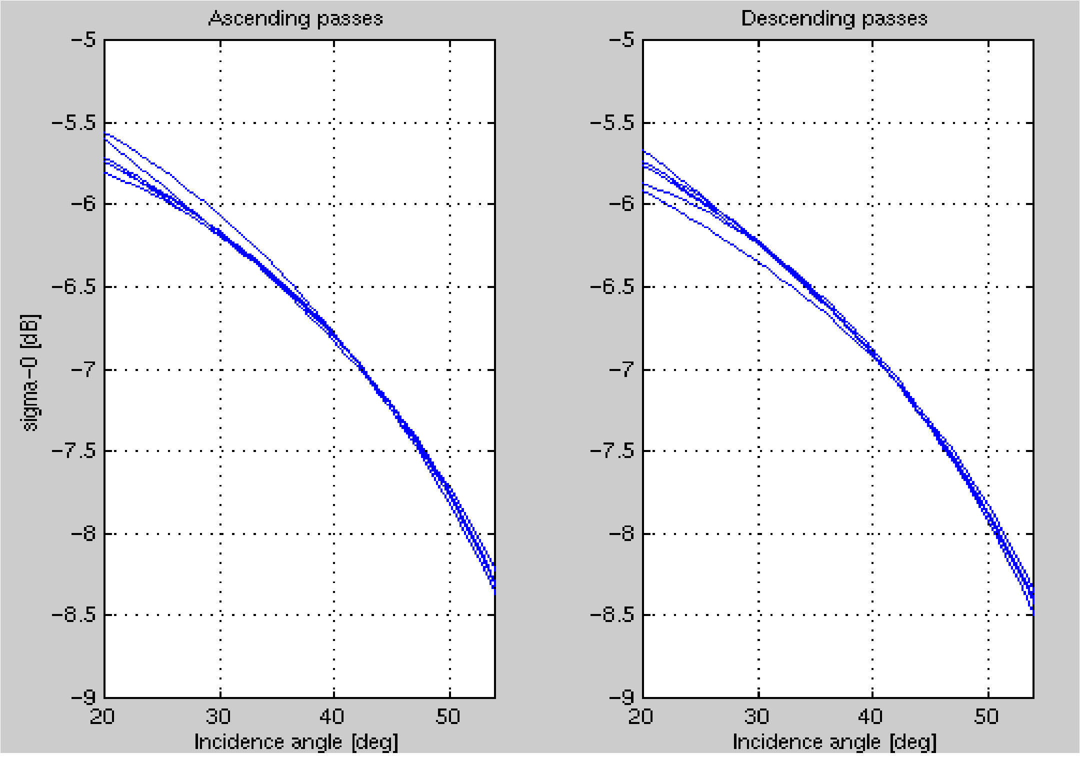

Figure 58: Attitude adjusted beam balanced $\sigma_b^o(\theta)$ for Amazon January 97 data.

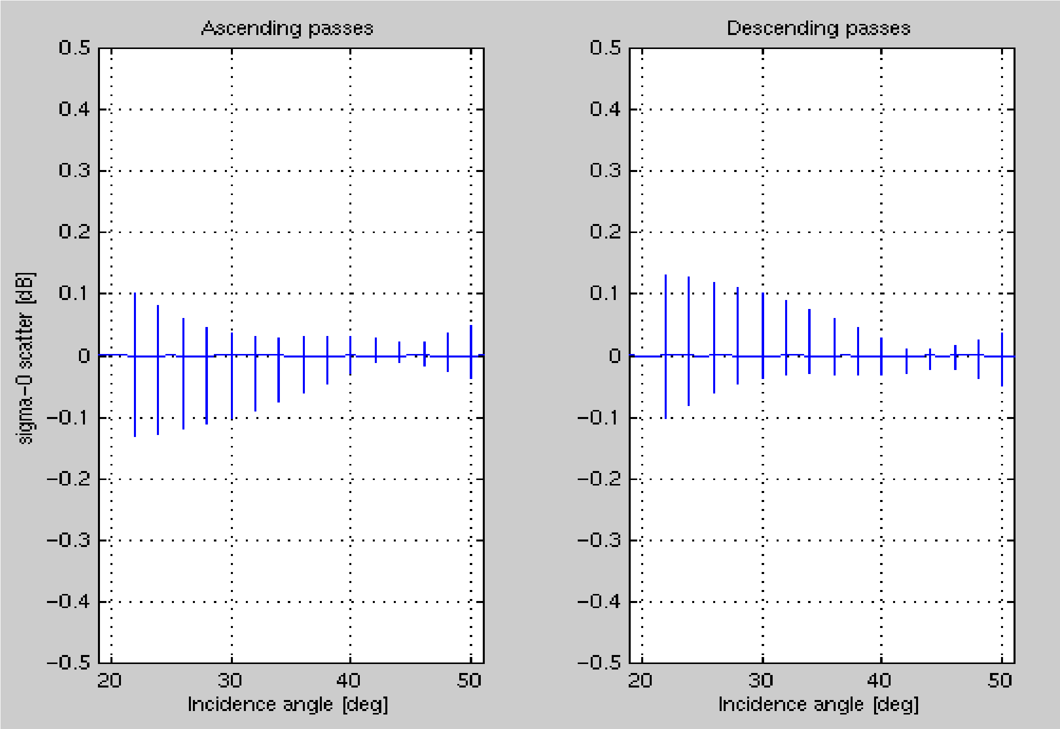

Figure 59 $\sigma_b^o(\theta)$ scatter for attitude adjusted beam balanced Amazon January 97 data.

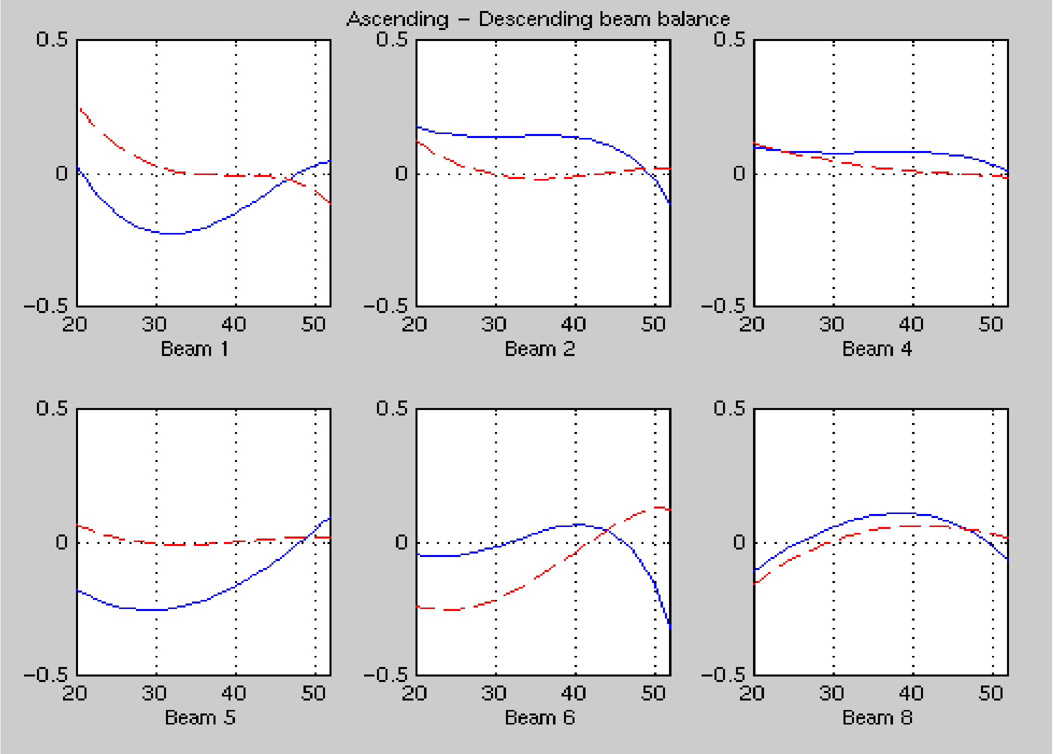

Figure 60: Improvement in NSCAT consistency after attitude adjustment, January 97 Amazon data

The last set of figures illustrates beam balance and attitude adjustment effects on data taken over central Russia. A three-week period in November 96 is chosen. Raw uncorrected $\sigma_b^o(\theta)$ data are plotted on Figure 61, and the corresponding scatter is on Figure 62. Applying nominal attitude beam correction, results in a tighter grouping of individual beam responses and reduced scatter (Figures 63 and 64). Further improvement is achieved if the attitude from Table 5 is applied (r_A=0.2°, p_A= -0.2°, y_A= 0.2°, r_D= 0.1°, p_D= 0°, and y_D= 0°). It is again stressed that this attitude differs from the bias at Equatorial latitudes around Amazon. This points to latitudinal (orbit position) dependence of the ADEOS attitude variations. The improvement is obvious from figures 65-67, although not as dramatic as for more homogenous Amazon target.

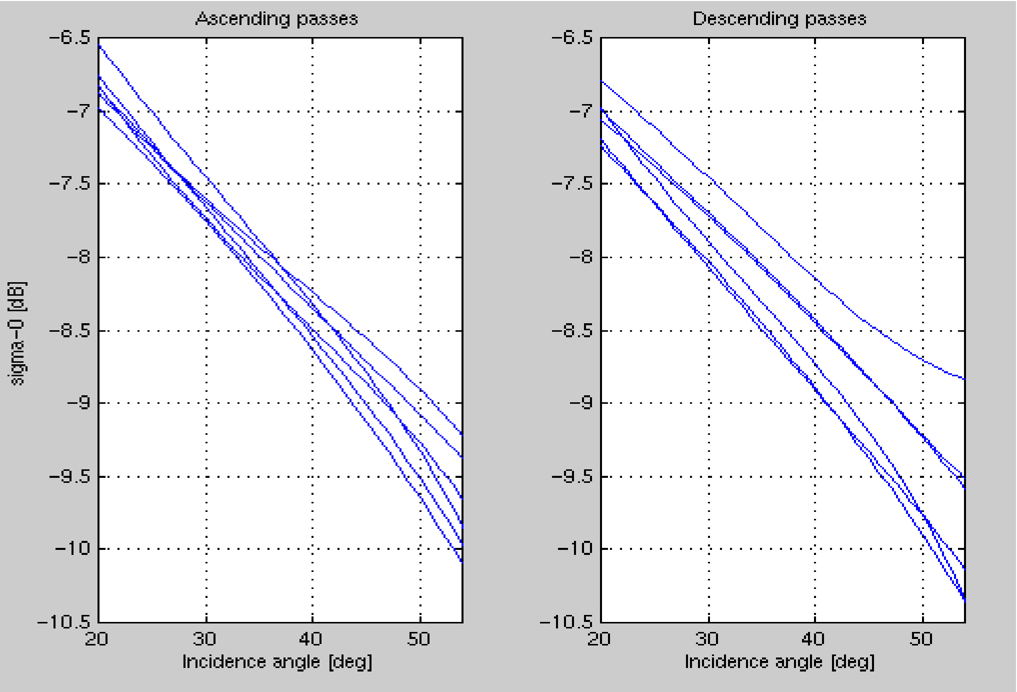

Figure 61: Raw NSCAT $\sigma_b^o(\theta)$ for central Russia November 96 data.

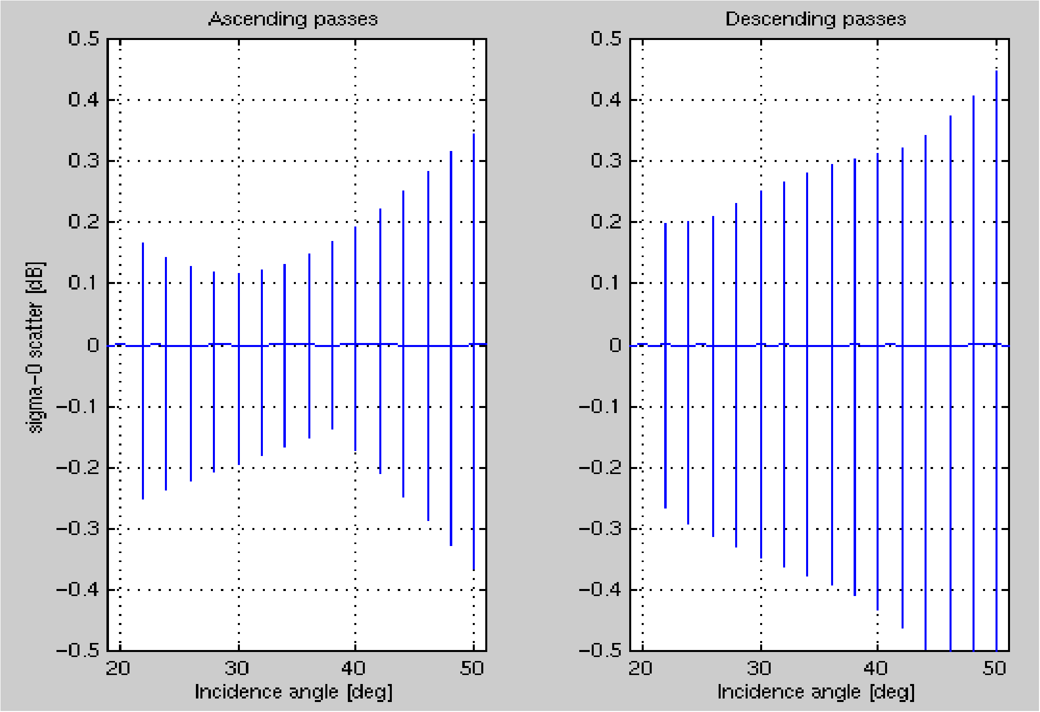

Figure 62 $\sigma_b^o(\theta)$ scatter for raw central Russia November 96 data.

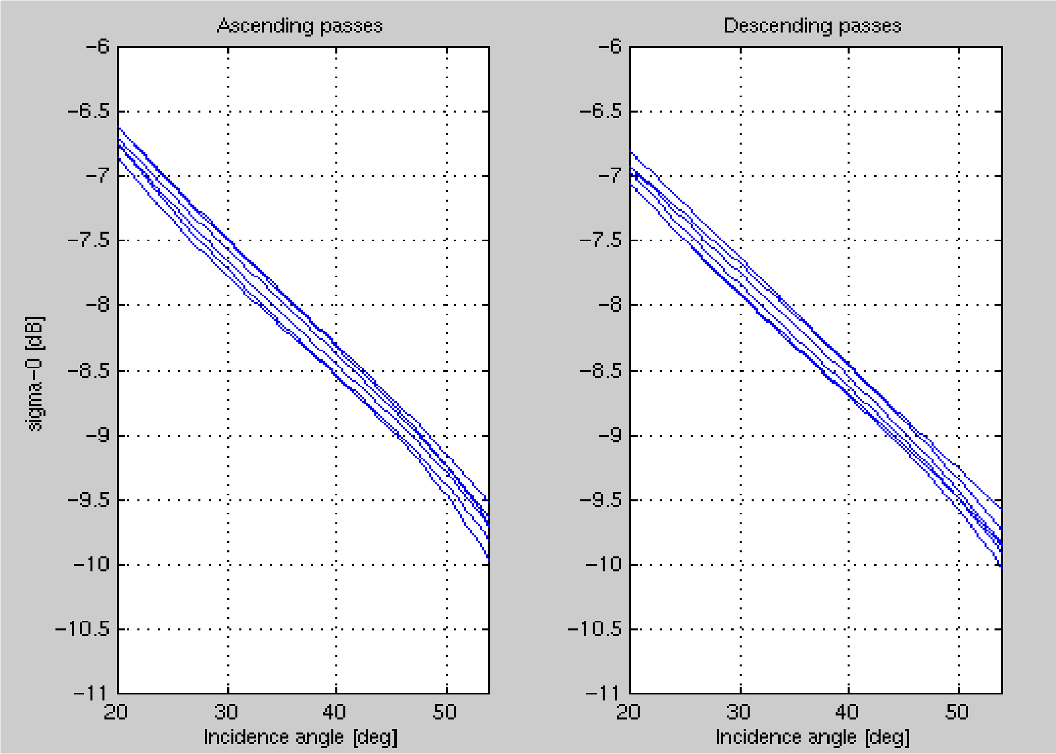

Figure 63: Zero-attitude beam balanced $\sigma_b^o(\theta)$ for central Russia November 96 data.

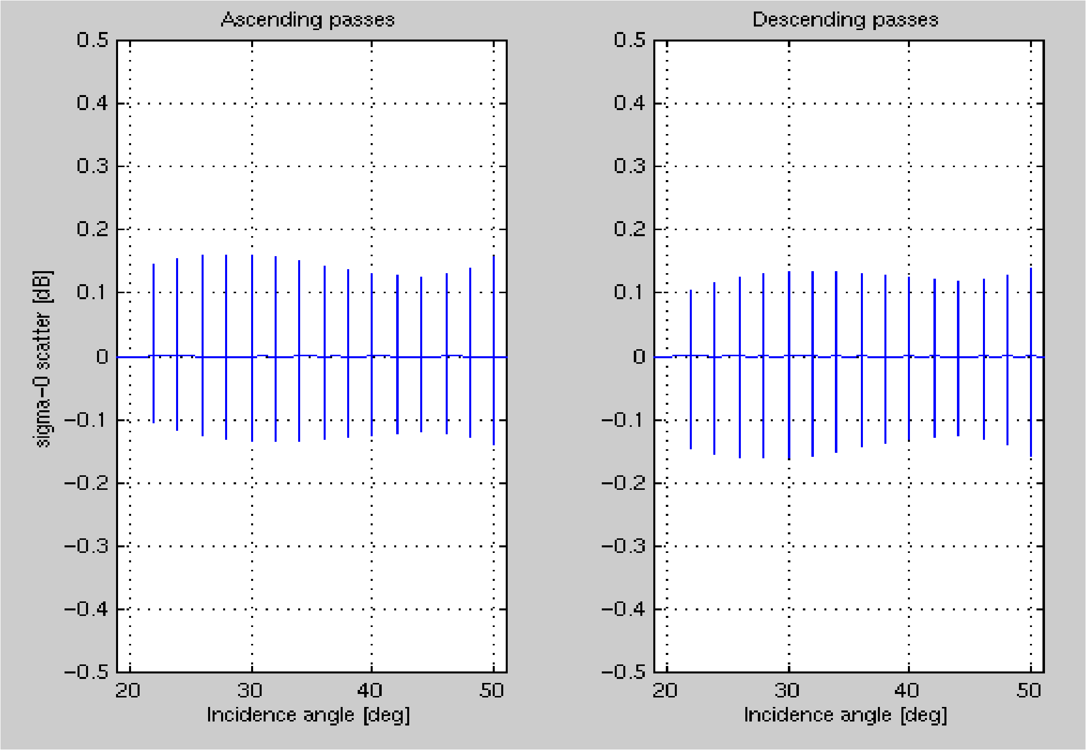

Figure 64: $\sigma_b^o(\theta)$ scatter for zero-attitude beam balanced central Russia November 96 data.

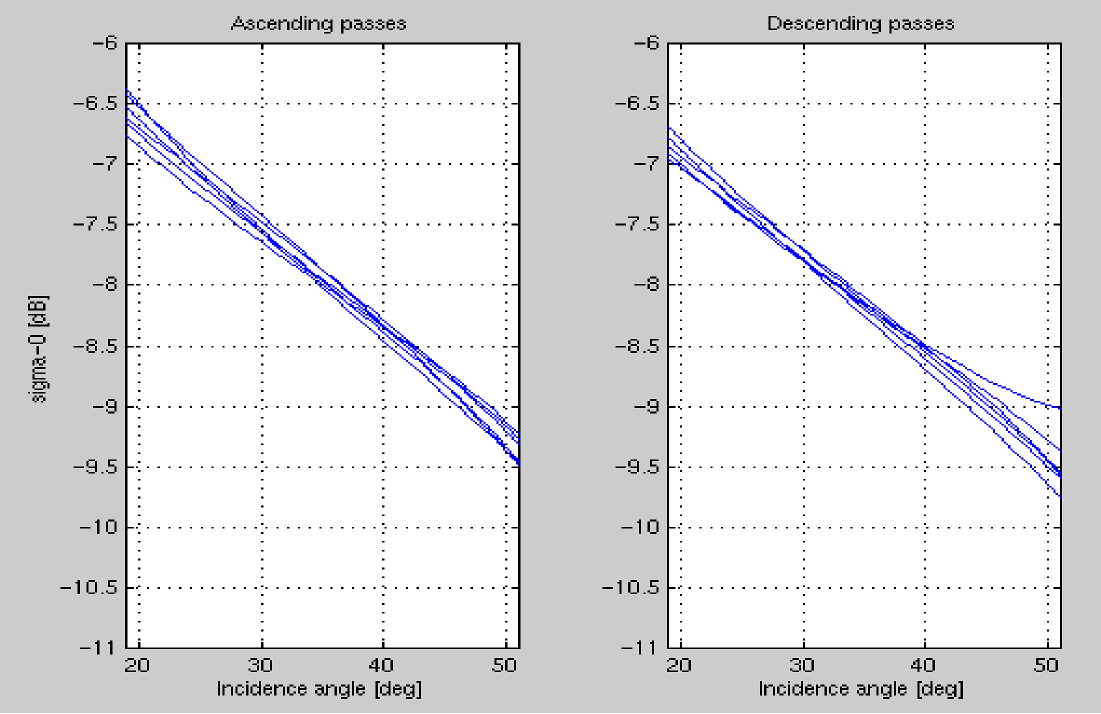

Figure 65: Attitude adjusted beam balanced $\sigma_b^o(\theta)$ for central Russia November 96 data.

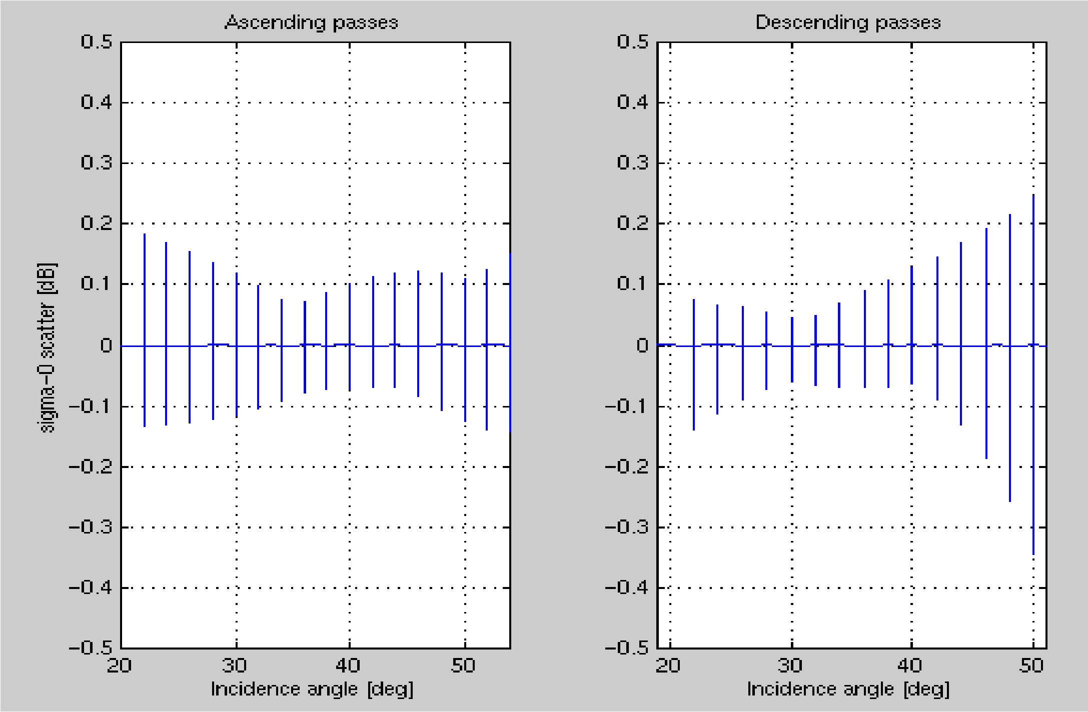

Figure 66: $\sigma_b^o(\theta)$ scatter for attitude adjusted beam balanced central Russia November 96 data.

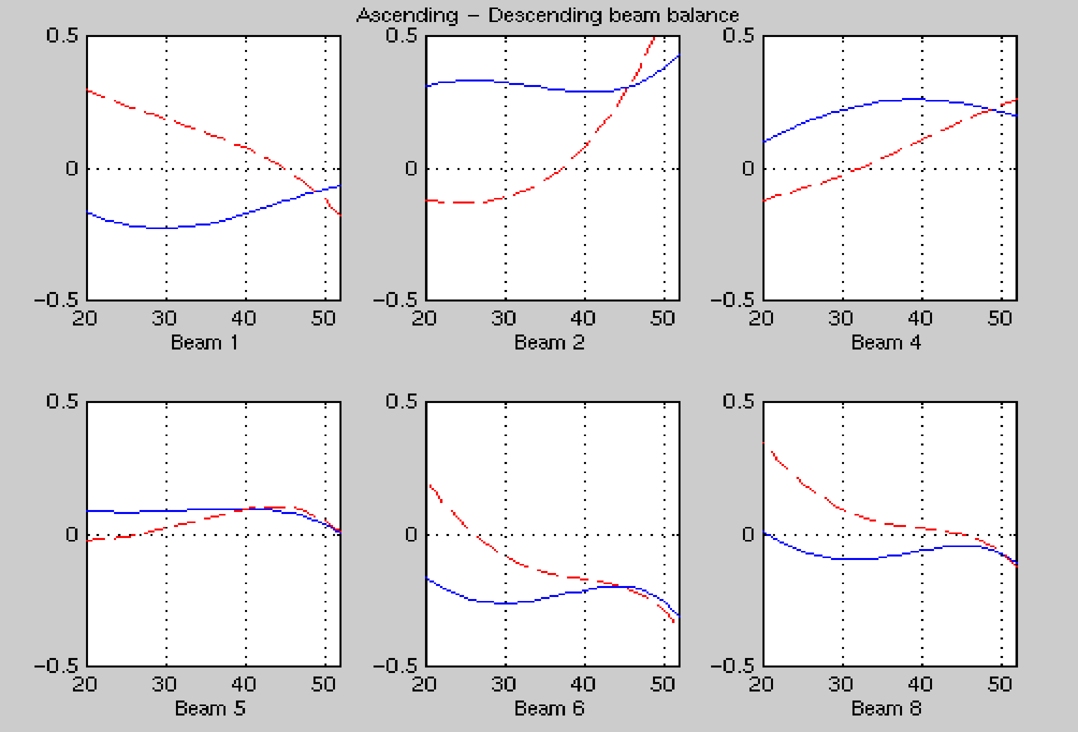

Figure 67: Improvement in NSCAT consistency after attitude adjustment November 96 central Russia data.

The figures in this section illustrate that improved consistency in NSCAT data from ascending and descending passes can be obtained if attitude adjustment is applied in addition to beam balancing. It is another tribute to stability of the NSCAT instrument, which can detect even ADEOS spacecraft biases. In the core of the attitude determination is the beam balance method, based on homogenous land targets. Therefore, it proves the versatility of the method that can be used to signal if other anomalies, besides antenna beam biases, are present in a scatterometer mission.

6. CONCLUSION

This dissertation discussed antenna beam balance of the NASA Scatterometer instrument. Satellite scatterometers are expected to become an important source of ocean and terrain geophysical observations in the future. Retrieval of wind vectors over sea surface is the primary application. Surface wind vectors are considered crucial meteorological variables in determining local weather and global climate patterns. Spaceborne instruments are necessary to provide desired coverage and frequency of observations. Scatterometer measurement geometry uses multiple antenna beams (different azimuth look) in order to enable wind direction ambiguity removal. The beams must be well calibrated and relative biases among them must be eliminated. Pre-launch calibration alone has proven inadequate in the past. On-orbit, post-launch activities are therefore planned for all scatterometer missions.

A simple method is derived that eliminates relative biases among the eight beams produced by NSCAT antennas. The method relies on homogenous large area targets with azimuth-independent radar response. For such targets, σ^o depends on incidence angle alone. The same $\sigma_b^0(\theta)$ is expected for all beams *b*. Amazon tropical rainforest satisfies homogeneity requirement and is selected as the main calibration target in the study. Scatterometer Image Resolution algorithm is used to select points falling within the mask of the homogenous response. To strengthen the homogeneity assumption, the target is divided into smaller location elements. However, results did not change from the treatment of the Amazon as a unit, confirming homogeneity of the selected area.

Data taken over Amazon mask is used to model $c_b(\theta)$ by a third order polynomial. Beam balance corrections are calculated as to force models from all beams to the average model. Beam balance calculation is repeated in several periods during NSCAT lifetime. Results from all periods are close, proving remarkable stability of the instrument before the spacecraft failure. The magnitudes of corrections are several tenths of a dB, which is significant for desired wind retrieval accuracy. This justifies on-orbit calibration prior to data release. The homogenous land target method converged very closely to other post-launch beam balance methods (ocean, ice, and ground station), thus, independently confirming $c_b(\theta)$ that was accepted for the NSCAT final σ^o reprocessing. Since NSCAT is primarily a wind-measuring instrument, the accepted method was correlating measurements to wind field models, such as the European Center for Medium Weather Prediction model.

Because of the diurnal variations in geophysical parameters of natural targets, calibration data are analyzed separately for ascending (night) and descending (day) passes. It is expected that both data sets should converge to the same beam balance corrections $c_b(\theta)$. Corrections quantify end-to-end relative system gain bias and should be constant within an orbit for a given beam. However, a stable systematic difference between corrections calculated based on ascending and descending passes ($\Delta c = c_{b,A}(\theta) - c_{b,D}(\theta)$) is noticed in all balancing methods. It is suggested that attitude bias of the ADEOS spacecraft is causing this difference. This assumption is strengthen by the parametrical analysis showing reduced Δc for adjusted attitude. A cost function is formulated and parametrical approach adopted to estimate the attitude bias. The critical bias is estimated to be 0.2-0.3^{o} difference between ascending and descending yaw angles. Pitch is also a significant attitude variable. Roll biases do not significantly affect beam balance corrections, meaning that spacecraft roll bias can not be detected by beam balance inconsistency. Estimated attitude bias differs for central Russia and Amazon, suggesting latitudinal dependence of the mean attitude bias. The ability to estimate these fine attitude imperfections is another proof of unprecedented stability of the NSCAT instrument. It also shows versatility of the simple beam balancing method that can be used to detect system anomalies other that beam biases alone.

APPENDIX A

BEAM BALANCE TABLE

Inc. angle [deg]	Beam 1 [dB]	Beam2 [dB]	Beam 3 [dB]	Beam 4 [dB]	Beam 5 [dB]	Beam 6 [dB]	Beam 7 [dB]	Beam 8 [dB]
16	0.2388	0.5437	0.2646	-0.0194	0.1755	-0.3634	0.4359	0.3671
18	0.2459	0.4767	0.2201	-0.0021	0.0550	-0.3068	0.3691	0.3219
20	0.2559	0.4226	0.1781	0.0115	-0.0479	-0.2584	0.3117	0.2797
22	0.2685	0.3802	0.1383	0.0219	-0.1352	-0.2176	0.2629	0.2403
24	0.2834	0.3485	0.1008	0.0296	-0.2082	-0.2082	-0.1839	0.2035
26	0.3000	0.3267	0.0654	0.0353	-0.2687	-0.1565	0.1882	0.1689
28	0.3181	0.3138	0.0320	0.0395	-0.3180	-0.1347	0.1608	0.1363
30	0.3373	0.3091	0.0003	0.0430	-0.3574	-0.1176	0.1392	0.1054
32	0.3572	0.3116	-0.0299	0.0466	-0.3883	-0.1041	0.1225	0.0758
34	0.3773	0.3207	-0.0587	0.0510	-0.4119	-0.0930	0.1099	0.0470
36	0.3970	0.3354	-0.0864	0.0572	-0.4298	-0.0832	0.1007	0.0187
38	0.4160	0.3549	-0.1133	0.0663	-0.4432	-0.0730	0.0938	-0.0097
40	0.4337	0.3783	-0.1397	0.0796	-0.4538	-0.0609	0.0885	-0.0387
42	0.4492	0.4045	-0.1659	0.0986	-0.4633	-0.0446	0.0834	-0.0689
44	0.4619	0.4324	-0.1922	0.1254	-0.4736	-0.0218	0.0774	-0.1011
46	0.4708	0.4606	-0.2190	0.1623	-0.4872	0.0106	0.0690	-0.1361
48	0.4749	0.4874	-0.2468	0.2128	-0.5065	0.0566	0.0565	-0.1749
50	0.4725	0.5109	-0.2761	0.2815	-0.5350	0.1213	0.0376	-0.2188
52	0.4620	0.5283	-0.3075	0.3751	-0.5767	0.2120	0.0096	-0.2693
54	0.4409	0.5362	-0.3419	0.5034	-0.6368	0.3393	-0.0308	-0.3285
56	0.4059	0.5301	-0.3803	0.6825	-0.7218	0.5194	-0.0884	-0.3991
58	0.3525	0.5036	-0.4241	0.9406	-0.8407	0.7793	-0.1696	-0.4849
60	0.2740	0.4473	-0.4753	1.3328	-1.0056	1.1679	-0.2832	-0.5916
62	0.1605	0.3477	-0.5372	1.9919	-1.2336	1.7891	-0.4426	-0.7276
64	-0.0046	0.1829	-0.6150	3.3975	-1.5507	2.9321	-0.6689	-0.9072
66	-0.2503	-0.0844	-0.7183	6.3655	-1.9992	6.4422	-0.9981	-1.1559

APPENDIX B

NSCAT LEVEL 1.5 RECORD STRUCTURE

Variable	Type, size [byte]	Dimension	Byte offset	Scale
UTC time	Char, 24	1	0	-
Revolution number	Long,4	1	24	-
Level 1.0 quality flag	Logic,4	1	28	-
Level 1.5 quality flag	Logic,4	1	32	-
Current mode	Byte,1	1	36	-
Current antenna beam	Byte,1	1	37	-
Calibration frame flag	Byte,1	1	38	-
Spare byte	Byte,1	1	39	-
Orbit time	Byte,1	1	40	1
Spacecraft latitude	Long,4	1	44	0.001
Spacecraft longitude	Long,4	1	48	0.001
Spacecraft altitude	Long,4	1	52	1
X position	Long,4	1	56	1
Y position	Long,4	1	60	1
Z position	Long,4	1	64	1
X velocity	Long,4	1	68	1
Y velocity	Long,4	1	72	1
Z velocity	Long,4	1	76	1
Roll	Int,2	1	80	0.001
Pitch	Int,2	1	82	0.001
Yaw	Int,2	1	84	0.001
Spare bytes	Int,2	1	86	-
Center latitude	Long,100	25	88	0.001
Center longitude	Long,100	25	188	0.001
Corner latitude displacement	Int,200	4 X 25	288	0.001
Corner longitude displacement	Int,200	4 X 25	488	0.001
Cell azimuth	Int,50	25	688	0.01
Incidence angle	Int,50	25	738	0.01
Latitude displacement	Int,50	25	788	1
Longitude displacement	Int,50	25	838	1
Antenna angle	Int,50	25	888	0.01
Squint angle	Int,2	1	938	0.01
Antenna gain	Int,50	25	940	0.01
Estimated received power	Int,50	25	990	0.01
Estimated noise power	Int,50	25	1040	0.01

Variable	Type, size [byte]	Dimension	Byte offset	Scale
Signal to noise ratio	Int,50	25	1090	0.01
σ^0	Int,50	25	1140	0.01
Kp coefficient A	Int,50	25	1190	0.00001
Kp coefficient B	Int,50	25	1240	0.00001
Kp coefficient C	Int,50	25	1290	0.00001
σ^0 quality flag	Int,50	25	1340	-
Along-track grid index	Int,50	25	1390	1
Cross-track grid index	Byte,25	25	1440	1
Doppler channel number	Byte,25	25	1465	1
Surface flag	Byte,25	25	1490	-
Atmospheric attenuation	Byte,25	25	1515	0.002
Spare	Byte,4	4	1540	-

APPENDIX C

FORTRAN PROGRAM FOR COARSE DATA SELECTION

```
        PROGRAM SELECT
c       Execution: select start_rev end_rev

c       Variable declarations
        integer cells
        parameter cells=25
        INTEGER      l15recl,rev, oper_mode,beam _no, cal_frame,
   $          l15_qual_flg
        INTEGER*4 orb_tim
        REAL*8 center_lat(CELLS),
   $    center_lon(CELLS),
   $    lat_error(CELLS),
   $    lon_error(CELLS),
   $    incidence_angle(CELLS),
   $    corner_lat_1(CELLS),
   $    corner_lon_1(CELLS),
   $    corner_lat_2(CELLS),
   $    corner_lon_2(CELLS),
   $    corner_lat_3(CELLS),
   $    corner_lon_3(CELLS),
   $    corner_lat_4(CELLS),
   $    corner_lon_4(CELLS),
   $    corr_sigma(CELLS)

    parameter l15recl=1544
    character l15rec(l15recl),arev*5,argv*4
    character l15_file*60,froot*21
    integer f,signed,unsigned
    data froot/'/external/Common/L15/'/

c       Open output files and read start and end revs from command line
        open(39,file='Amazon_asc',access='append',fileopt='eof')
        open(40,file='Amazon_dsc',access='append',fileopt='eof')
        open(41,file='Russia_asc',access='append',fileopt='eof')
        open(42,file="Russia_dsc",access='append',fileopt='eof')
        call GETARG(1,argv)
        read(argv,'(i)')irev1
        call GETARG(2,argv)
        read(argv,'(i)')irev2

c       For all revs between and including irev1 and irev2 do the following:
        do irev=irev1,irev2
        write(arev,'(i5.5)') irev
        l15_file = froot//'S15'//arev//'.DAT'
        ierr=lstat(l15_file,istat)
        if (ierr .ne. 0) then
```

```
                      go to 25
            end if
            open (unit=11,name=l15_file,access='direct',recl=l15recl)

c           Read data of interest from L1.5 file
            f=14000             ! Maximum number of frames per file
      iframe=4
      do while ( iframe .le. f )
      read (unit=11,err=20,end=21,rec=iframe) l15rec
            signed = 1
        unsigned = 0
            nb=1
      j=37
      oper_mode = int_ext(l15rec,j,nb,unsigned)
      j=j+nb
            beam_no =int_ext(l15rec,j,nb,unsigned)
            nb=4
        j=41
        orb_tim = (int_ext(l15rec,j,nb,unsigned))
        j=j+nb
        sc_lat = real(int_ext(l15rec,j,nb,signed))*1.e-3
        j=j+nb
        sc_lon = real(int_ext(l15rec,j,nb,unsigned))*1.e-3
        j=j+nb
        sc_alt = real(int_ext(l15rec,j,nb,unsigned))
        j=j+nb
        x_pos = real(int_ext(l15rec,j,nb,signed))
        j=j+nb
        y_pos = real(int_ext(l15rec,j,nb,signed))
        j=j+nb
        z_pos = real(int_ext(l15rec,j,nb,signed))
        j=j+nb
        x_vel = real(int_ext(l15rec,j,nb,signed))
        j=j+nb
        y_vel = real(int_ext(l15rec,j,nb,signed))
        j=j+nb
        z_vel = real(int_ext(l15rec,j,nb,signed))
      nb=4
      j=89
      do i=1,25
        center_lat(i) = real(int_ext(l15rec,j,nb))*1.e-3
        j=j+nb
      enddo
      do i=1,25
        center_lon(i) = real(int_ext(l15rec,j,nb))*1.e-3
        j=j+nb
      enddo
            nb=2
        j=689
            do i=1,25
          beam_azi(i) = real(int_ext(l15rec,j,nb,unsigned))*1.e-2
          j=j+nb
        enddo
        do i=1,25
```

```
       incidence_angle(i) = real(int_ext(l15rec,j,nb,unsigned))*1.e-2
         j=j+nb
       enddo
           nb=2
       j=1141
       do i=1,25
         corr_sigma(i) = real(int_ext(l15rec,j,nb,signed))*1.e-2
         j=j+nb
       enddo
       do i=1,25
         coeff_a(i) = real(int_ext(l15rec,j,nb,unsigned))*1.e-5
         j=j+nb
       enddo
       do i=1,25
         coeff_b(i) = real(int_ext(l15rec,j,nb,unsigned))*1.e-6
         j=j+nb
       enddo
       do i=1,25
         coeff_c(i) = real(int_ext(l15rec,j,nb,unsigned))*1.e-6
         j=j+nb
       enddo

c          Write data of interest in output files
           do i=1,25
c   **************** AMAZON********************************
           if ( (center_lat(i) .gt. -23.9) .and. (center_lat(i) .lt.
    $      6.9) .and. (center_lon(i) .gt. 280.1) .and. (
    $      center_lon(i) .lt. 326.9) .and. (corr_sigma(i) .lt.
    $      50) .and. (corr_sigma(i) .gt. -100) .and. (beam_no
    $      .ne. 9) .and. (beam_no .ne. 9) .and. (incidence_angle(i)
    $      .lt. 65) .and. (incidence_angle(i) .gt. 1) .and. (z_vel
    $           .gt. 0) ) then
           write(39,19)beam_no,center_lat(i),center_lon(i),
    $                incidence_angle(i),corr_sigma(i)
 19        format(I1,1x,F6.2,1x,F6.2,1x,F5.2,1x,F7.2)
           endif
           if ( (center_lat(i) .gt. -23.9) .and. (center_lat(i) .lt.
    $      6.9) .and. (center_lon(i) .gt. 280.1) .and. (
    $      center_lon(i) .lt. 326.9) .and. (corr_sigma(i) .lt.
    $      50) .and. (corr_sigma(i) .gt. -100) .and. (beam_no
    $      .ne. 9) .and. (beam_no .ne. 9) .and. (incidence_angle(i)
    $      .lt. 65) .and. (incidence_angle(i) .gt. 1) .and. (z_vel
    $       .lt. 0) ) then
      write(40,19)beam_no,center_lat(i),center_lon(i),
    $        incidence_angle(i),corr_sigma(i)
      endif

c     ******************* RUSSIA ********************************
           if ( (center_lat(i) .gt. 51.0) .and. (center_lat(i) .lt.
    $      69.3) .and. (center_lon(i) .gt. 59.0) .and. (
    $      center_lon(i) .lt. 133.5) .and. (corr_sigma(i) .lt.
    $      50) .and. (corr_sigma(i) .gt. -100) .and. (beam_no
    $      .ne. 9) .and. (beam_no .ne. 9) .and. (incidence_angle(i)
    $      .lt. 65) .and. (incidence_angle(i) .gt. 1) .and. (z_vel
```

```
    $              .gt. 0) ) then
            write(41,19)beam_no,center_lat(i),center_lon(i),
    $                     incidence_angle(i),corr_sigma(i)
            endif
            if ( (center_lat(i) .gt. 51.0) .and. (center_lat(i) .lt.
    $       69.3) .and. (center_lon(i) .gt. 59.0) .and. (
    $       center_lon(i) .lt. 133.5) .and. (corr_sigma(i) .lt.
    $       50) .and. (corr_sigma(i) .gt. -100) .and. (beam_no
    $       .ne. 9) .and. (beam_no .ne. 9) .and. (incidence_angle(i)
    $       .lt. 65) .and. (incidence_angle(i) .gt. 1) .and. (z_vel
    $        .lt. 0) ) then
      write(42,19)beam_no,center_lat(i),center_lon(i),
    $          incidence_angle(i),corr_sigma(i)
      endif

            enddo
            iframe=iframe+1
            enddo
25          continue
20          print*,'end'
21          print*,'end'
            close(11)
            enddo

            close(39)
            close(40)
            close(41)
            CLOSE(42)
            end
c***********     The end of the main program *******************
            INTEGER FUNCTION INT_EXT(REC,N,M,signed)
        character rec(*)
        integer n,m,signed
        integer*4 int4
        character ib(4)
        equivalence (int4,ib)
        int4    = 0
        nn      = n
        mm      = 5 - m
        do i = mm,4
               ib(i) = rec(nn)
               nn = nn + 1
        enddo
cc   check for 2-byte (signed) negative integers
cc   note: there are no signed 1-byte integers
        if ((m .eq. 2) .and. (signed .eq. 1) ) then
           if (btest(int4,8*m-1)) then
                ib(1) = char(255)    ! this is probably a bit faster
                 ib(2) = char(255)
           endif
        endif
        int_ext = int4
        return
        end
```

APPENDIX D

MATLAB ROUTINES FOR FINE DATA SELECTION, BEAM BALANCE, AND ATTITUDE ANALYSIS

Fine_sel.m

```
% This program selects NSCAT measurements that are taken over Amazon
% rainforest. Measurements should be pre-selected in Amazon_*sc file
% formatted as              Beam   Lat    Lon    Inc    Sig0.
% The output of the program is file AMS which contains selected
% entries that are within Amazon mask. Data are NOT changed by this
% program, only selection is performed !!

clear;
%         Open files and fill appropriate arrays
fid = fopen('SASS_bitmask1_cor_ed','r');       % SIR Amazon mask
M = fread(fid,[744,1128],'integer*1');         % Use fread for binary
load Amazon_asc;          AA=Amazon-asc;
Lat = AA(:,2);
Lon = AA(:,3);
rows=length(AA);

%         Transform lats/lons into indexes corresponding to mask grid
%         These commands are SIR-specific
I = round(24.0*(7.0*ones(size(Lat))-Lat)+1);
J = round(24.0*(Lon-280.0*ones(size(Lon)))+1);

%         Select data classified as Amazon
Ams=[];
k4=rows-2;
for k=3:k4
          if ( rem(k,1000) == 0)
                    k
          end
%         Check if measurement coordinates included in SIR mask
          C = M(I(k-2),J(k+2)) * M(I(k-1),J(k+2)) * M(I(k),J(k+2)) * M(I(k+1),J(k+2)) * M(I(k+2),J(k+2));
          C = C * M(I(k-2),J(k+1)) * M(I(k-1),J(k+1)) * M(I(k),J(k+1)) * M(I(k+1),J(k+1)) *
M(I(k+2),J(k+1));
          C = C * M(I(k-2),J(k)) * M(I(k-1),J(k)) * M(I(k),J(k)) * M(I(k+1),J(k)) * M(I(k+2),J(k));
          C = C * M(I(k-2),J(k-1)) * M(I(k-1),J(k-1)) * M(I(k),J(k-1)) * M(I(k+1),J(k-1)) * M(I(k+2),J(k-
1));
          C = C * M(I(k-2),J(k-2)) * M(I(k-1),J(k-2)) * M(I(k),J(k-2)) * M(I(k+1),J(k-2)) * M(I(k+2),J(k-
2));
          if (C == 1)                  % Include measurement for calibration
```

```
                Ams=[Ams;AA(k,:)];
        end
end

fid2 = fopen('ASA','A');
count = fprintf(fid2,'%1.0f %6.2f %6.2f %5.2f %5.2f\n',Ams');
fclose('all');
```

Beam _bal.m

```
%       This program performs collocation, polynomial approximation of
%       measurements from the reference beam, and difference calculations
%       between measured and modeled values for all beams. The input is
%       selected ASA file. Collocation is performed in cells of radius D.
%       The output is in matrices R11-R81 containing sigma-0, incidence angles and location indexes

clear;
rd=pi/180;              % degrees -> radians
load A_Dec96/ASAuc;
AMS=ASAuc;
ind=find(AMS(:,5)~=0);
AMS=AMS(ind,:);
rows=(nzmax(AMS))/6;
D=500;
Lats=AMS(:,2);
Lons=AMS(:,3);
AMS(:,5)=10.^(0.1*AMS(:,5));
R=[];                   % Final solution (differences) will be in this matrix
O=[];
A=[];
R11=[];R21=[];R31=[];R41=[];R51=[];R61=[];R71=[];R81=[];
EE11=[]; EE21=[]; EE31=[]; EE41=[]; EE51=[]; EE61=[]; EE71=[]; EE81=[];
I=[];

%       Check uniform distribution of beams
b1=find(AMS(:,1)==1);
b2=find(AMS(:,1)==2);
b3=find(AMS(:,1)==3);
b4=find(AMS(:,1)==4);
b5=find(AMS(:,1)==5);
b6=find(AMS(:,1)==6);
b7=find(AMS(:,1)==7);
b8=find(AMS(:,1)==8);

fid2 = fopen('COL','w');    % File to contain collocation indexes
%       Initialize arrays needed in collocation
Flag=zeros(rows,1);
g=0;
G=zeros(rows,1);

%       Start looping through AMS file
```

```
for k1=1:rows
if (Flag(k1) == 0)            % Check if not yet collocated
          D11=0; D21=0; D31=0; D41=0; D51=0; D61=0; D71=0; D81=0;
          A1=zeros(4,1);
    g=g+1;
    G(k1)=g;
    Mi=[k1];                  % Assign new cell number if not yet collocated

%         Loop through all remaining measurements
    k3=k1+1
    for k2=k3:rows
    if (Flag(k2) == 0)        % Check if not yet collocated
          c=acos(cos((Lats(k1)-Lats(k2))*rd)*cos((Lons(k1)-Lons(k2))*rd));
          d=6378*c;
          if (d < D)                    % Check if point k2 in the cell defined by k1&D
            Flag(k2)=1;
       Mi=[Mi k2];
            G(k2)=g;                    % Collcate k2 with k1 if d < D
          end
    end
    end
% *********** The end of the collocation for a single cell*************

%         Start approximation and difference calculations, extract data
%         needed for polynomial approximation for the current cell
     Beamc=AMS(Mi,1);
     Incc=AMS(Mi,4);
     Sigc=AMS(Mi,5);

%         Bin measurements according to beams
            bi11=find(Beamc == 1);
      bi21=find(Beamc == 2);
      bi31=find(Beamc == 3);
      bi41=find(Beamc == 4);
      bi51=find(Beamc == 5);
      bi61=find(Beamc == 6);
      bi71=find(Beamc == 7);
      bi81=find(Beamc == 8);
      n1=nzmax(bi11);

          if (nzmax(bi11) > 50)         % 50 points enough for reliable modeling
           S1=Sigc(bi11);
           I1=Incc(bi11)-40*ones(nzmax(bi11),1);
                    I1=Incc(bi11)-mean(Incc(bi11));
                    minc=mean(Incc(bi11));
           s=min(n1,3);
           A1=polyfit(I1,S1,s);

                    %I11=Incc(bi11)-40*ones(nzmax(bi11),1);
           I11=Incc(bi11)-mean(Incc(bi11));
           IP11=polyval(A1,I11);
           ee11=Sigc(bi11)./IP11;
           EE11=[EE11;ee11];
           i11=Incc(bi11);
```

```
 D11=mean(Sigc(bi11)./IP11);
 R11=[R11;Sigc(bi11) ee11 i11 g*ones(size(ee11))];

        if (nzmax(bi21) > 0)      %beam 2
                 %I21=Incc(bi21)-40*ones(nzmax(bi21),1);
                I21=Incc(bi21)-mean(Incc(bi11));
                IP21=polyval(A1,I21);
                ee21=Sigc(bi21)./IP21;
                EE21=[EE21;ee21];
                i21=Incc(bi21);
                D21=mean(Sigc(bi21)./IP21);
                R21=[R21;Sigc(bi21) ee21 i21 g*ones(size(ee21))];
 else
     D21=0;
 end

 if (nzmax(bi31) > 0)
        %I31=Incc(bi31)-40*ones(nzmax(bi31),1);
        I31=Incc(bi31)-mean(Incc(bi11));
        IP31=polyval(A1,I31);
        ee31=Sigc(bi31)./IP31;
        EE31=[EE31;ee31];
        i31=Incc(bi31);
        D31=mean(Sigc(bi31)./IP31);
        R31=[R31;Sigc(bi31) ee31 i31 g*ones(size(ee31))];
 else
     D31=0;
 end

if (nzmax(bi41) > 0)
         %I41=Incc(bi41)-40*ones(nzmax(bi41),1);
        I41=Incc(bi41)-mean(Incc(bi11));
        IP41=polyval(A1,I41);
        ee41=Sigc(bi41)./IP41;
        EE41=[EE41;ee41];
        i41=Incc(bi41);
        D41=mean(Sigc(bi41)./IP41);
        R41=[R41;Sigc(bi41) ee41 i41 g*ones(size(ee41))];
 else
     D41=0;
 end

if (nzmax(bi51) > 0)
          %I51=Incc(bi51)-40*ones(nzmax(bi51),1);
        I51=Incc(bi51)-mean(Incc(bi11));
        IP51=polyval(A1,I51);
        ee51=Sigc(bi51)./IP51;
        EE51=[EE51;ee51];
        i51=Incc(bi51);
        D51=mean(Sigc(bi51)./IP51);
        R51=[R51;Sigc(bi51) ee51 i51 g*ones(size(ee51))];
 else
     D51=0;
 end
```

```
if (nzmax(bi61) > 0)
                 %I61=Incc(bi61)-40*ones(nzmax(bi61),1);
                I61=Incc(bi61)-mean(Incc(bi11));
                IP61=polyval(A1,I61);
                ee61=Sigc(bi61)./IP61;
                EE61=[EE61;ee61];
                i61=Incc(bi61);
                D61=mean(Sigc(bi61)./IP61);
                R61=[R61;Sigc(bi61) ee61 i61 g*ones(size(ee61))];
  else
           D61=0;
  end

if (nzmax(bi71) > 0)
                %I71=Incc(bi71)-40*ones(nzmax(bi71),1);
                I71=Incc(bi71)-mean(Incc(bi11));
                IP71=polyval(A1,I71);
                ee71=Sigc(bi71)./IP71;
                EE71=[EE71;ee71];
                i71=Incc(bi71);
                D71=mean(Sigc(bi71)./IP71);
                R71=[R71;Sigc(bi71) ee71 i71 g*ones(size(ee71))];
  else
           D71=0;
  end

  if (nzmax(bi81) > 0)
                %I81=Incc(bi81)-40*ones(nzmax(bi81),1);
                I81=Incc(bi81)-mean(Incc(bi11));
                IP81=polyval(A1,I81);
                D81=mean(Sigc(bi81)./IP81);
                ee81=Sigc(bi81)./IP81;
                EE81=[EE81;ee81];
                i81=Incc(bi81);
                R81=[R81;Sigc(bi81) ee81 i81 g*ones(size(ee81))];
  else
                D81=0;
end

if (nzmax(A1) == 3)
                A1=[A1(1);A1(2);A1(3);0];
elseif (nzmax(A1) == 2)
                   A1=[A1(1);A1(2);0;0];
  elseif (nzmax(A1) == 1)
                   A1=[A1(1);0;0;0];
  elseif (nzmax(A1) == 0)
                  A1=[0;0;0;0];
else
                A1=A1';
  end
                a=[A1]
                A=[A a];
                I=[I minc];
end
```

```
%           Number of measurements in the bin
             o11=nzmax(bi11);
             o21=nzmax(bi21);
             o31=nzmax(bi31);
             o41=nzmax(bi41);
             o51=nzmax(bi51);
             o61=nzmax(bi61);
             o71=nzmax(bi71);
             o81=nzmax(bi81);
            OO=[o11;o21;o31;o41;o51;o61;o71;o81];
            O=[O OO];

%           Mean differences in each bin
            DD=[D11;D21;D31;D41;D51;D61;D71;D81];
            R=[R DD];

end
end

% ******************* RESULTS  ****************************%
i11=find( (R11(:,2)>0.2) & (R11(:,2)<2) );
R11=R11(i11,:);
i21=find( (R21(:,2)>0.2) & (R21(:,2)<2) );
R21=R21(i21,:);
i31=find( (R31(:,2)>0.2) & (R31(:,2)<2) );
R31=R31(i31,:);
i41=find( (R41(:,2)>0.2) & (R41(:,2)<2) );
R41=R41(i41,:);
i51=find( (R51(:,2)>0.2) & (R51(:,2)<2) );
R51=R51(i51,:);
i61=find( (R61(:,2)>0.2) & (R61(:,2)<2) );
R61=R61(i61,:);
i71=find( (R71(:,2)>0.2) & (R71(:,2)<2) );
R71=R71(i71,:);
i81=find( (R81(:,2)>0.2) & (R81(:,2)<2) );
R81=R81(i81,:);

x=16:2:66;
a1=polyfit(R11(:,3)-40,R11(:,2),3);
a2=polyfit(R21(:,3)-40,R21(:,2),3);
a3=polyfit(R31(:,3)-40,R31(:,2),3);
a4=polyfit(R41(:,3)-40,R41(:,2),3);
a5=polyfit(R51(:,3)-40,R51(:,2),3);
a6=polyfit(R61(:,3)-40,R61(:,2),3);
a7=polyfit(R71(:,3)-40,R71(:,2),3);
a8=polyfit(R81(:,3)-40,R81(:,2),3);
y1=polyval(a1,x-40);
y2=polyval(a2,x-40);
y3=polyval(a3,x-40);
y4=polyval(a4,x-40);
y5=polyval(a5,x-40);
y6=polyval(a6,x-40);
y7=polyval(a7,x-40);
y8=polyval(a8,x-40);
```

```
%	Mean of differences
EE=[EE11;EE21;EE31;EE41;EE51;EE61;EE71;EE81];
Col=[Lats Lons G];
count2 = fprintf(fid2,'%6.2f %6.2f %5.0f\n',Col');	% Collocation
fclose('all');
```

Calc_at_tab.m

```
%	This file calculates differences in sigma0 due
%	attitude change. It does NOT mask data over Amazon
%	to increase the execution speed.
clear
x=16:1:66;
OF=123;
ATa=[]; ata=[];

% Zero attitude file
fc=int2str(OF);
File=strcat(' AA',fc)
lfile=strcat('load',File);
eval(lfile);
matrix=strcat('AA=',File,';');
eval(matrix);
AMS=AA;

% Beam balance for the zero attitude file
ind=find((AMS(:,5)~=0) & (AMS(:,4)>15) & (AMS(:,1)~=5) & (AMS(:,1)~=6));
AMS=AMS(ind,:);
AMS(:,5)=10.^(0.1*AMS(:,5));
b1=find(AMS(:,1)==1);
b2=find(AMS(:,1)==2);
b3=find(AMS(:,1)==3);
b4=find(AMS(:,1)==4);
b7=find(AMS(:,1)==7);
b8=find(AMS(:,1)==8);
a=polyfit(AMS(:,4)-40,AMS(:,5),3);
a1=polyfit(AMS(b1,4)-40,AMS(b1,5),3);
a2=polyfit(AMS(b2,4)-40,AMS(b2,5),3);
a3=polyfit(AMS(b3,4)-40,AMS(b3,5),3);
a4=polyfit(AMS(b4,4)-40,AMS(b4,5),3);
a7=polyfit(AMS(b7,4)-40,AMS(b7,5),3);
a8=polyfit(AMS(b8,4)-40,AMS(b8,5),3);
S=10*log10(polyval(a,x-40));
S1=10*log10(polyval(a1,x-40));
S2=10*log10(polyval(a2,x-40));
S3=10*log10(polyval(a3,x-40));
S4=10*log10(polyval(a4,x-40));
S7=10*log10(polyval(a7,x-40));
S8=10*log10(polyval(a8,x-40));

% Go through all files
```

```
i=1;
for r=-5:5          % Roll
r=r/10.0;
for p=-5:5          % Pitc
p=p/10.0;
for y=-5:5          % Yaw
y=y/10.0;

        %           Open appropriate attitude file
        fc=int2str(i);
        File=strcat(' AA',fc)
        lfile=strcat('load',File);
        eval(lfile);
        matrix=strcat('AA=',File,';');
        eval(matrix);
        AMS=AA;

        % calculate corrections for the given attitude file
        ind=find((AMS(:,5)~=0)&(AMS(:,4)>15)&(AMS(:,1)~=5)&(AMS(:,1)~=6))
        AMS=AMS(ind,:);
        AMS(:,5)=10.^(0.1*AMS(:,5));
        b1=find(AMS(:,1)==1);
        b2=find(AMS(:,1)==2);
        b3=find(AMS(:,1)==3);
        b4=find(AMS(:,1)==4);
        b7=find(AMS(:,1)==7);
        b8=find(AMS(:,1)==8);
        a=polyfit(AMS(:,4)-40,AMS(:,5),3);
        a1=polyfit(AMS(b1,4)-40,AMS(b1,5),3);
        a2=polyfit(AMS(b2,4)-40,AMS(b2,5),3);
        a3=polyfit(AMS(b3,4)-40,AMS(b3,5),3);
        a4=polyfit(AMS(b4,4)-40,AMS(b4,5),3);
        a7=polyfit(AMS(b7,4)-40,AMS(b7,5),3);
        a8=polyfit(AMS(b8,4)-40,AMS(b8,5),3);
        s=10*log10(polyval(a,x-40));
        s1=10*log10(polyval(a1,x-40));
        s2=10*log10(polyval(a2,x-40));
        s3=10*log10(polyval(a3,x-40));
        s4=10*log10(polyval(a4,x-40));
        s7=10*log10(polyval(a7,x-40));
        s8=10*log10(polyval(a8,x-40));

        d=s-S; d1=s1-S1;d2=s2-S2; d3=s3-S3; d4=s4-S4; d7=s7-S7; d8=s8-S8;
        ata=[0 r p y d; 1 r p y d1; 2 r p y d3; 3 r p y d7; 4 r p y d8;
           5 r p y d4; 6 r p y d2];
        ATa=[ATa;ata];
        cfile=strcat('clear AA',fc);
        eval(cfile);
i=i+1;
end
end
end
save ATa2 ATa
```

Find_best_at.m

```
%       This program finds the best attitude resulting
%       in the lowest difference between the ascending
%       and descending beam corrections
clear;
load A_Nov96/ABBuc;             %Initialize working files
load ATT_Nov96/ATa;
load ATT_Nov96/ATd;
l=10; u=35;       % AD (7-37 == 22-52)
ll=4+l; uu=ll+(u-l);
ba1=ba1(l:u); ba2=ba2(l:u); ba3=ba3(l:u); ba4=ba4(l:u); ba5=ba5(l:u);
ba6=ba6(l:u); bd1=bd1(l:u); bd2=bd2(l:u); bd3=bd3(l:u); bd4=bd4(l:u);
bd5=bd5(l:u); bd6=bd6(l:u);
Res=[];

i=1;
for ra=-5:1:5                 % Attitude ranges
ra=ra/10.0
for pa=-5:1:5
pa=pa/10.0
for ya=-5:1:5
ya=ya/10.0
for rd=-5:1:5
rd=rd/10.0;
for pd=-5:1:5
pd=pd/10.0;
for yd=-5:1:5
yd=yd/10.0;

inda=find((ATa(:,2)==ra) & (ATa(:,3)==pa) & (ATa(:,4)==ya));
indd=find((ATd(:,2)==rd) & (ATd(:,3)==pd) & (ATd(:,4)==yd));
Delta=ATa(inda,:); Deltd=ATd(indd,:);
dao=Delta(1,ll:uu); ddo=Deltd(1,ll:uu);

d=zeros(size(ba1));
for b=1:6
        beam=int2str(b); asc=strcat('ba',beam); dsc=strcat('-bd',beam);
        sdif=strcat(asc,dsc);
        d1=eval(sdif);
        d2=d1+dao-ddo;
        da=Delta(b+1,ll:uu);      dd=Deltd(b+1,ll:uu);
        d3=abs(d2-da+dd);
        d=d+d3;
end

dif=sum(d);
Res(i,:)=[ra pa ya rd pd yd dif];

i=i+1;
end
end
end
end
```

```
end
end

fid2 = fopen('Results','W');
count=fprintf(fid2,'%5.2f  %5.2f  %5.2f  %5.2f  %5.2f  %5.2f     %5.2f\n',Res');
fclose('all');
```

LIST OF REFERENCES

[1] Allen, T. D., A Review of Seasat. In *Satellite Microwave Remote Sensing*, T. D. Allen, ed., Ellis Howars, Ltd., pp. 11-44 (1983).

[2] Alhumaidi, S. M., Development of a Geophysical Model function for a radar Scatterometer Using Neural Networks, Ph.D. dissertation, Florida Institute of Technology, Melbourne, FL (1997).

[3] Attema, E. P. W., The Active Microwave Instrument On-board the ERS-1 Satellite, *Proc. IEEE*, vol. 79, No.6 (1991).

[4] Bachman, C. G., *Radar Targets*, Lexington Books, Lexington, MA (1982).

[5] Balanis, C. A., *Advanced Engineering Electromagnetics*, Villey, New York (1989).

[6] Bass, F. G., I. M. Fuks, *Wave Scattering from Statistically Rough Surfaces*, Pergamon Press, New York (1979).

[7] Birer, I. J., E. M. Bracalante, E. M. Dome, G. J. Sweet, and G. Berthold, σ^o Signature of the Amazon Rain Forest Obtained from the Seasat Scatterometer, *IEEE Trans. Geoscience and remote Sensing*, Vol. Ge-20, no. 1, pp. 11-17 (1982).

[8] Boggs, D. H., The SEASAT Scatterometer Model Function: The Genesis of SASS 1, JPL Report 622-230, California Institute of Technology, Pasadena, CA (1981).

[9] Brekhovskikh, L. M., *Waves in Layered Media*, Academic Press, New York (1960).

[10] Chang, A. T., A. S. Milman, Retrieval of Ocean Surface and Atmospheric Parameters from Multichannel Microwave Radiometric Measurements, *IEEE Trans. Geosci. Rem. Sensing*, GE-20, pp. 217-224 (1982).

[11] Claasesen, J. P., R. K. Moore, H. S. Fung, and W. J. Pierson, Jr, Radar Sea Return and the RADSCAT Satellite Anemometer, *Oceans '72, IEEE International Conference record: Engineering in the Ocean Environment* (IEEE Publication 72 CHO 660-1 OCC), Newport, RI, pp. 180-185 (1972).

[12] Cutrona, L. J., Synthetic Aperture Radar, Chapter 23 in *Radar Handbook*, M. I. Skolnik, ed., Mc-Graw-Hill Book Company, New York, pp 717-729, (1962)

[13] Daley, J. C., Wind Dependence of Radar Sea Return, *J. Geophys. Res*., 78, pp. 7823-7888 (1973).

[14] Daum, D. R., D. G. Long, and Davis, W. B., Reconstruction Enhanced resolution Images from Spaceborne Microwave Sensors, *Proc. International Geoscience and Remote Sensing Symp*., Pasadena, CA, pp. 2231-2233 (1994).

[15] Deepak, A., ed., *Remote Sensing of Atmospheres and Oceans*, Academic Press, New York (1980).

[16] Dunbar, R. S., s. V. Hsiao, and B. H. Lambrigsten, Science Algorithm Specifications for the NASA scatterometer Project, JPL report D-5610, Jet Propulsion Laboratory, Pasadena, CA (1988).

[17] Elachi, C., *Introduction to Physics and Techniques of Remote Sensing*, John Villey & Sons, New York (1987).

[18] Elachi, C., *Spaceborne Radar Remote Sensing: Applications and Techniques*, IEEE Press, New York (1988).

[19] Frison, P. L., and E. Mougin, Use of ERS-1 Wind Scatterometer Data Over land Surfaces, *IEEE trans. Geoscience and Remote Sensing*, Vol. 34, no.2, pp.550-560 (1996).

[20] Grantham, W. L., E. M. Bracalente, W. L. Jones, and W. J. Johnson, The SEASAT-A Satellite Scatterometer, *IEEE J. Oceanic Engineering*, OE-2, pp. 200-206, (1977).

[21] Hovanessian, S. A., *Introduction to Synthetic Array and Imaging Radars*, Artech House, Dedham, MA, (1980).

[22] Johnson, J. L., L. A. Williams, Jr., E. M. Bracalante, F. B. Beck, and w. L. Grantham, SEASAT-A Satellite Scatterometer Instrument Evaluation, *IEEE J. Oceanic Engineering*, OE-5, pp. 138-144, (1980).

[23] Jones, W. L., L. C. Schroeder, and J. L. Mitchell, Aircraft Measurements of the Microwave Scattering Signature of the Ocean, *IEEE Trans. on Antennas and Prop*., AP-25, pp. 52-61, (1977).

[24] Jones, W. L., L. C. Schroeder, D. H. Boggs, E. M. Bracalante, R. A. Brown, G. J. Dome, W. J. Pierson, and F. J. Wentz, The SEASAT-A Satellite Scatterometer: The Geophysical Evaluation of Remotely Sensed Wind Vectors over the Ocean, *J. Geophys. Res*., 87, pp. 3297-3317 (1982).

[25] Karam, M. A., and A. K. Fung, Propgation and Scattering in Multilayered Random Media with Rough Interfaces, *Electromagnetics*, 2, pp. 239-256 (1982).

[26] Kennet, R. G., and F. K. Li, Seasat Over-land Scatterometer Data, Part 2: selection of Extended Area Land Target Sites for the Calibration of Spaceborne Scatterometers, *IEEE Trans. Geoscience and Remote Sensing, vol. Ge-27, no.6, pp.779-788*

[27] Kerr, D. E., H. Goldstein, Radar Targets and Echoes, Chapter 6 in *Propagation of Short Radio waves*, D. E. Kerr, ed., MIT Radiation Laboratory Series, McGraw-Hill Book Company, New York, (1951)

[28] Long, M. W., *Radar reflectivity of Land and Sea*, Lexington Books, Lexington, MA, (1975).

[29] Long, D. G., P. Hardin, and P. Whiting, resolution Enhancement of Spaceborne Scatterometer Data, *IEEE Trans. Geoscience and Remote Sensing*, Vol. 31, no.3, pp. 700-715 (1993).

[30] Long, D. G., and G. B. Skouson, Calibration of Spaceborne Scatterometers Using Tropical Rain Forests, IEEE Trans on Geoscience and Remote Sensing, Vol. 34, no. 2, pp. 413-424 (1996).

[31] R.K. Moore, W.J. Pierson: Measuring Sea State and Estimating Surface Winds From a Polar Orbiting Satellite, *Proc. International Symp. on Electromagnetic Sensing of the Earth from Satellites*, Miami Beach, FL (1966).

[32] Moore, R. K., and F. T. Ulaby, The Radar Radiometer, *Proc. IEEE*, 57. 587-590, (1969).

[33] Moore, R. K., and A. K. Fung, Radar Determination of Winds at Sea, *Proc. IEEE*, 67, pp 1504-1521, (1979)

[34] Naderi, F., M. H. Freilich, and D. G. Long, Spaceborne Radar Measurement of Wind Velocity over the Ocean - An Overview of the NSCAT System, *Proc IEEE*, vol. 79, no. 6, pp. 850-866, (1991).

[35] Stiles, W. H., and F. T. Ulaby, The Active and Passive Microwave Response to Snow parameters, *J. Geophys. Res.*, pp. 1037-1044 (1980)

[36] Schmugge, T., Remote Sensing of Surface Soil Moisture, *J. Appl. Meteorol.*, 17, pp. 1549-1557, (1978)

[37] Schroeder, L. C., D. H. Boggs, G. J. Dome, I. M. Halberstam, W. L. Jones, W. J. Pierson, and F. J. wentz, The Relationship Between Wind Vector and Normalized radar Cross Section Used to Derive SEASAT-A Satellite Scatterometer Winds, *J. Geophys. Res.*, 87, pp.3318-3336 (1982).

[38] Skolnik, M. I., *Radar Handbook*, McGraw-Hill, New York, (1970)

[39] Skolnik, M. I., *Introduction to Radar Systems*, 2nd edition, McGraw-Hill Book Company, New York, (1980)

[40] Ulaby, F. T., P. P. Batlivala, and M. C. Dobson, Microwave Backscatter Dependence on Surface Roughness, Soil Moisture, and Soil Texture: Part 1- Bare Soil, *IEEE Trans. geoscience Elect*., GE-16, pp. 286-295, (1978)

[41] Ulaby, F. T., W. H. Stiles, D. Brunfeldt, and E. Wilson, 1-35 GHz Microwave Scatterometer, *Proc. 1979 IEEE/MTT-S Intl. Microwave Symp.*, Orlando, FL, (1979)

[42] Ulaby, F.T., Moore, R.K., and Fung, A.K., *Microwave Remote Sensing Active and Passive,* Norwood, MA: Artech House, Inc., 1986.

[43] Wentz, F. J., S. Peterych, L. A. Thomas, A Model Function for Ocean radar Cross Section at 14.6 GHZ, J. Geophys. Res., vol. 89, no. 93 (1984).

[44] Wurtele, M. G., P. M. Woiceshyn, S. Peterych, M. Borowski, and W. S. Appleby, Wind Direction Alias Removal Studies of SEASAT Scatterometer-Derived Wind Fields, *J. Geophys. Res*., 87, pp. 3365-3377 (1982).